

Metastable 1T'-phase group VI transition metal dichalcogenide crystals

Zhuangchai Lai,^{1,2†} Qiyuan He,^{3†} Thu Ha Tran,^{2†} D. V. Maheswar Repaka,^{4†} Dong-Dong Zhou,⁵ Ying Sun,^{6,7} Shibo Xi,⁴ Yongxin Li,⁸ Apoorva Chaturvedi,² Chaoliang Tan,⁹ Bo Chen,¹ Gwang-Hyeon Nam,² Bing Li,¹⁰ Chongyi Ling,¹ Wei Zhai,¹ Zhenyu Shi,^{1,2} Dianyi Hu,² Vinay Sharma,² Zhaoning Hu,² Ye Chen,¹¹ Zhicheng Zhang,^{2,12} Yifu Yu,^{2,13} Xiao Renshaw Wang,^{8,14} Raju V. Ramanujan,² Yanming Ma,^{6,7,15} Kedar Hippalgaonkar,^{2,4*} Hua Zhang^{1,16,17*}

¹Department of Chemistry, City University of Hong Kong, Kowloon, Hong Kong, China.

²Center for Programmable Materials, School of Materials Science and Engineering, Nanyang Technological University, 50 Nanyang Avenue, Singapore 639798, Singapore.

³Department of Materials Science and Engineering, City University of Hong Kong, Kowloon, Hong Kong, China.

⁴Institute of Materials Research and Engineering (IMRE), A*STAR (Agency for Science, Technology and Research), Singapore 138634, Singapore.

⁵MOE Key Laboratory of Bioinorganic and Synthetic Chemistry, School of Chemistry, Sun Yat-Sen University, Guangzhou 510275, China.

⁶State Key Laboratory of Superhard Materials, College of Physics, Jilin University, Changchun 130012, China.

⁷Innovation Center for Computational Physics Methods and Softwares, College of Physics, Jilin University, Changchun 130012, China.

⁸School of Physical and Mathematical Sciences, Nanyang Technological University, 637371 Singapore, Singapore.

⁹Department of Electrical Engineering, City University of Hong Kong, Kowloon, Hong Kong, China.

¹⁰School of Chemistry and Chemical Engineering, Harbin Institute of Technology, Harbin 150001, China.

¹¹Department of Chemistry, The Chinese University of Hong Kong, Shatin, N.T., Hong Kong, China

¹²Tianjin Key Laboratory of Molecular Optoelectronic Sciences, Department of Chemistry, School of Science, Tianjin University & Collaborative Innovation Center of Chemical Science and Engineering, Tianjin 300072, China.

¹³Institute of Molecular Plus, Tianjin University, Tianjin 300354, China.

¹⁴School of Electrical and Electronic Engineering, Nanyang Technological University, 639798 Singapore, Singapore.

¹⁵International Center of Future Science, Jilin University, Changchun 130012, China.

¹⁶Hong Kong Branch of National Precious Metals Material Engineering Research Center (NPMM), City University of Hong Kong, Kowloon, Hong Kong, China.

¹⁷Shenzhen Research Institute, City University of Hong Kong, Shenzhen, 518057, China.

†These authors contributed equally to this work.

*Correspondence author. E-mail: hua.zhang@cityu.edu.hk, kedar@ntu.edu.sg.

Keywords: 1T' phase, metastable phase, transition metal dichalcogenides, WS₂, WSe₂, superconductivity.

Metastable 1T'-phase transition metal dichalcogenides (1T'-TMDs) with semi-metallic nature have attracted increasing interest due to their unique distorted structures and fascinating phase-dependent physicochemical properties. However, the synthesis of high-quality metastable 1T'-TMD crystals, especially for the group VI TMDs, still remains a challenge. Here, we report a general synthetic method for the large-scale preparation of metastable 1T'-phase group VI TMDs, including WS₂, WSe₂, MoS₂, MoSe₂, WS_{2x}Se_{2(1-x)} and MoS_{2x}Se_{2(1-x)}. The crystal structures of 1T'-WS₂, -WSe₂, -MoS₂ and -MoSe₂ have been solved with single-crystal X-ray diffraction. The as-prepared 1T'-WS₂ exhibits thickness-dependent intrinsic superconductivity, showing critical transition temperatures of 8.6 K for the thickness of 90.1 nm and 5.7 K for the single layer, which could be attributed to the high intrinsic carrier concentration and the semi-metallic nature of 1T'-WS₂. This synthesis method will allow a more systematic investigation of the intrinsic properties of metastable TMDs.

Large-size and high-quality crystals are fundamentally important for studying the intrinsic physicochemical properties of ultrathin two-dimensional (2D) layered materials including graphene and transition metal dichalcogenides (TMDs)¹⁻⁴. Different from graphene which can be obtained by exfoliation of the easily accessible graphite crystals or using the well-developed chemical vapor deposition (CVD) method, the preparation of 2D TMDs is more complicated due to their diverse chemical compositions and crystal phases, especially the metastable phases such as octahedral (1T) and distorted octahedral (1T') phases^{5,6}. Compared with the thermodynamically stable trigonal prismatic (2H) phase TMDs which exhibit semiconducting properties, most of the 1T- and 1T'-phase TMDs are (semi-

)metallic, showing superior performances in (opto)electronics, catalysis, energy storage and superconductivity⁵⁻⁹. As known, very few 1T'-TMDs, such as 1T'-MoTe₂ and 1T'-WTe₂, are thermodynamically stable, which are readily prepared¹⁰⁻¹². It still remains a great challenge to prepare pure metastable 1T'-phase group VI TMDs^{5,6,13}. Although a few synthetic strategies have been reported to prepare metastable TMDs, including the chemical/electrochemical alkali metal ions intercalation method¹⁴⁻¹⁸, colloidal synthesis^{19,20}, hydrothermal reaction²¹, chemical vapor deposition²², electron beam irradiation²³, mechanical strain²⁴ and plasmonic hot electron²⁵, all of them can only produce limited types of metastable TMDs. Unfortunately, most of the synthesized metastable 1T- or 1T'-TMDs still contain 2H phase¹⁶⁻²⁰, making it impossible to characterize the intrinsic properties of metastable TMDs. Therefore, it is highly desirable to develop a general method for the synthesis of metastable 1T'-TMDs and consequently investigate their intrinsic properties as well as the phase-dependent applications.

Here, we report a facile and general synthetic method for preparation of metastable 1T'-phase group VI TMD crystals, including WS₂, WSe₂, MoS₂, MoSe₂, WS_{2x}Se_{2(1-x)} and MoS_{2x}Se_{2(1-x)}. The high purity of as-prepared 1T'-TMD crystals was confirmed by the aberration-corrected high-angle annular dark-field (HAADF) scanning transmission electron microscope (STEM), selected area electron diffraction (SAED), X-ray photoelectron spectroscopy (XPS), Auger electron spectroscopy (AES), Raman spectroscopy, X-ray diffraction (XRD), differential scanning calorimetry (DSC), thermogravimetric analysis (TGA), X-ray absorption near edge structure (XANES), extended X-ray absorption fine structure (EXAFS), and single-crystal XRD (SCXRD). Furthermore, 2H-phase group VI TMDs, including WS₂, WSe₂, MoS₂, MoSe₂, WS_{2x}Se_{2(1-x)}

x) and $\text{MoS}_{2x}\text{Se}_{2(1-x)}$, can be easily obtained by thermal annealing of the corresponding 1T'-TMDs, and further confirmed by XRD, XPS, DSC, TGA, Raman spectroscopy, XANES and EXAFS. As a proof-of-concept application, in order to study the superconducting properties of 1T'-WS₂, electrical transport devices based on the mechanically exfoliated 1T'-WS₂ nanosheets were fabricated. It was found that 1T'-WS₂ becomes superconducting when the temperature cools down, showing critical transition temperatures (T_c) of 8.6 K for the thickness of 90.1 nm and 5.7 K for the single layer with thickness of ~1.0 nm. Such high T_c values are ascribed to the high intrinsic carrier concentration and semi-metallic nature of 1T'-WS₂.

The detailed synthetic procedure and the experimental set-up are described in **Methods** and **Supplementary Fig. 1**. As shown in the **Fig. 1a**, the scanning electron microscopy (SEM) image of as-prepared 1T'-WS₂ crystals clearly reveals that their lateral size is up to a few hundred micrometers. The chemical composition of 1T'-WS₂ crystals was confirmed by the energy-dispersive X-ray spectroscopy (EDS), showing strong signals of W and S elements with an atomic ratio of ~1:2 (**Fig. 1b**), which is consistent with the stoichiometry of WS₂. In order to obtain the precise structure of 1T'-WS₂, high-quality crystals of as-prepared 1T'-WS₂ (inset in **Fig. 1a**) were characterized by SCXRD. Detailed crystallographic and structure refinement data of 1T'-WS₂ are summarized in **Supplementary Tables 1-3** and **Supplementary Fig. 2a**. Briefly, 1T'-WS₂ crystallizes in a monoclinic symmetry with the space group of $C2/m$ (space group number 12; $a = 12.848(5)$ Å, $b = 3.2178(12)$ Å, $c = 5.693(2)$ Å, $\beta = 112.847(13)^\circ$ and $V = 216.88(15)$ Å³). The powder XRD pattern of our as-prepared 1T'-WS₂ is well consistent with the simulated pattern of the 1T'-WS₂ crystal (**Supplementary Fig. 3**), confirming the 1T' phase of our

as-prepared WS₂. Moreover, XRD pattern measured in the transmission mode (**Supplementary Fig. 4**) is also consistent with the simulated pattern, further revealing the high-phase purity of the as-prepared 1T'-WS₂ crystals.

Thermal annealing at 400 °C under Ar atmosphere can induce the phase transition of as-prepared 1T'-WS₂ to form 2H-WS₂, which was confirmed by XRD, DSC, TGA, Raman, and XPS measurements (see the detailed information below). The (002) peak located at 14.3° was observed in the powder XRD pattern of the obtained 2H-WS₂ (**Fig. 1c-d**), which is consistent with previously reported 2H-WS₂ (REF.²⁶), indicating the complete phase transition of WS₂ from 1T' to 2H after the thermal annealing. Hereafter, all the 2H-TMDs used in this work are prepared by the thermal annealing of the corresponding as-prepared 1T'-TMDs. Based on the crystal structures of 1T' and 2H phases, (200) and (002) planes are the corresponding 2D planes of 1T'-WS₂ and 2H-WS₂, respectively. As shown in **Fig. 1d**, the (200) plane of 1T'-WS₂ shifts to a higher degree as compared with the (002) plane of 2H-WS₂, which is consistent with the SCXRD data because the interlayer distance of 1T'-WS₂ is smaller than that of 2H-WS₂, further confirming the 1T' crystal phase of our WS₂. Based on the obtained crystal structure, atomic models of 2H- and 1T'-WS₂ are schematically illustrated in **Fig. 1e-f**, revealing the obvious symmetry difference between the trigonal prismatic 2H and distorted octahedral 1T' phases. Compared with the 2H-WS₂ with symmetric hexagonal network throughout the 2D plane, 1T'-WS₂ exhibits a highly asymmetric nature with two adjacent lines of W atoms crowding together to form the unique zigzag chains.

To further confirm the crystal structure of our 1T'-WS₂, SAED patterns on different areas in typical 1T'-WS₂ flakes (**Fig. 2a-d** and **Supplementary Fig. 5a-b**) were obtained,

showing the characteristic 1T' structure diffraction³. From the high-resolution HAADF-STEM images taken on the different 1T'-WS₂ flakes (**Fig. 2e-f** and **Supplementary Fig. 5c-d**), one-dimensional zigzag chains of W atoms are observed and repeatedly appeared in the whole STEM image, which is consistent with the simulated structure model (**Fig. 2g**). Such asymmetric characteristic originates from the distorted 1T' structure, confirming the high purity of our 1T'-WS₂ crystals. In addition, the corresponding Fast Fourier Transform (FFT) pattern of the high-resolution HAADF-STEM image also exhibits the distorted octahedral coordination feature of the 1T' structure (**Fig. 2h**). The elemental mapping and EDS characterizations were carried out under STEM mode, showing strong W and S signals in our 1T'-WS₂ crystals (**Fig. 2i-l** and **Supplementary Fig. 6**).

In order to investigate the thermostability of our 1T'-WS₂ crystals, DSC and TGA measurements were carried out under N₂ in the temperature range from 30 to 300 °C. As shown in **Fig. 3a**, a clear exothermic peak located at 186.5 °C is observed, while the weight of 1T'-WS₂ crystals remained unchanged during the heating process (the blue line in **Fig. 3a**), indicating the phase transition from 1T' to 2H. The starting temperature of phase transition of 1T'-WS₂ is ~117.3 °C, much higher than that of 1T'-MoS₂ (~60 °C)³. Such improved thermostability offers great advantages in various applications, especially in the complex device fabrication process in order to investigate the intrinsic properties of 1T'-WS₂. The TGA-DSC characterization was also conducted on the 2H-WS₂ (**Supplementary Fig. 7**). Obviously, neither exothermic peak nor obvious weight loss was observed during the heating process, which is reasonable as the 2H phase is the thermodynamically stable phase of WS₂. Furthermore, Raman studies were performed on 1T'-WS₂ and 2H-WS₂ (**Fig. 3b**). Two characteristic peaks at 350.7 (E_{2g}¹) and 420.5 (A_{1g})

cm^{-1} are clearly observed in 2H-WS₂ (black curve in **Fig. 3b**)²⁷. The Raman spectrum of the as-prepared 1T'-WS₂ shows nine distinctive peaks located at 110.7, 127.4, 178.7, 239.7, 267.6, 275.4, 295.4, 315.4 and 406.2 cm^{-1} , respectively (red curve in **Fig. 3b**), which are completely different from those of 2H-WS₂. The peaks located at 127.4, 267.6 and 406.2 cm^{-1} are similar to the previously reported result¹⁷, which could be ascribed to the J₁, J₂ and J₃ vibration modes, respectively. However, the E_{2g}¹ (350.7 cm^{-1}) and A_{1g} (420.5 cm^{-1}) peaks belonging to the 2H phase are absent in the Raman spectrum of our as-prepared 1T'-WS₂ due to the high purity of the 1T' phase. Moreover, the Raman spectrum measured from the single-layer 1T'-WS₂ (violet curve in **Fig. 3b**) showed a small shift to higher wavenumbers as compared to the 1T'-WS₂ crystal, which is similar to previously reported layered TMD materials²⁸. To further understand the Raman vibrational modes of 1T'-WS₂, density functional theory (DFT) calculations based on the solved crystal structure are conducted and the results are shown in **Supplementary Fig. 8** and **Table 4**. Furthermore, XPS measurements were carried out on the 1T'- and 2H-WS₂ crystals (**Fig. 3c** and **Supplementary Fig. 9**). As shown in **Fig. 3c**, W 4f peaks of 1T'-WS₂ located at 31.5 and 33.7 eV can be assigned to 4f_{7/2} and 4f_{5/2}, respectively, which exhibited a clear shift of ~0.9 eV to lower binding energy as compared with 2H-WS₂. Similar result was also observed on the S 2p XPS spectra (**Supplementary Fig. 9a**). Importantly, it is worth mentioning that the complete removal of potassium in our as-prepared 1T'-WS₂ crystals was confirmed by the high-resolution K 2p XPS spectrum (**Supplementary Fig. 9b**) and AES measurements (**Supplementary Fig. 10-12**).

Moreover, X-ray absorption fine structure measurements were performed to investigate the structural properties of the as-prepared 1T'-WS₂ crystals. The edge position

of W L₃-edge XANES spectrum for 1T'-WS₂ shifts to lower energy as compared with that of 2H-WS₂ (**Supplementary Fig. 13**), indicating that the valence state of W in 1T'-WS₂ is lower than that of 2H-WS₂. Furthermore, based on the fitted result obtained by using an evolutionary algorithm-based code (EvAX)²⁹, both the Fourier and wavelet transforms of the fitted EXAFS spectra perfectly match those of the experimental EXAFS (**Fig. 3d** and **Supplementary Fig. 14**), proving the high purity of our as-prepared 1T'-WS₂, given that EXAFS is highly sensitive to the local structure change of materials. Specifically, as shown in **Supplementary Table 5**, the nearest W-S distance for 1T'-WS₂ obtained from EXAFS is ~2.42 Å, which is consistent with the average value of W-S bond lengths obtained from SCXRD (average: 2.435(5) Å). Additionally, compared to the nearest distance of W-W for 2H-WS₂ (3.18 Å), the distribution of adjacent W-W distances in 1T'-WS₂ was split to three different values (2.81, 3.23 and 3.78 Å), perfectly matching the results obtained from SCXRD (2.779(2), 3.218(1) and 3.792(2) Å). The local structures of 1T'-WS₂ and 2H-WS₂ were further confirmed by the radial distribution functions (**Supplementary Fig. 15**), showing the broadening of W-S distribution and splitting of W-W distribution for 1T'-WS₂, which are consistent with the analysis data shown in **Supplementary Table 5**. The EXAFS spectrum and analysis results of 2H-WS₂ also perfectly match those derived from standard XRD data (**Fig. 3d, Supplementary Fig. 16** and **Supplementary Table 5**), further confirming the purity of our materials. Furthermore, the possible reaction mechanism for the synthesis of 1T'-WS₂ has been studied and described in detail in **Supplementary Fig. 17-19**. Besides 1T'-WS₂, five more 1T'-TMD crystals, including 1T'-WSe₂, 1T'-WS₂_xSe_{2(1-x)}, 1T'-MoS₂, 1T'-MoSe₂ and 1T'-MoS₂_xSe_{2(1-x)} were also successfully synthesized and fully

characterized (see detailed information in **Supplementary Figs. 2, 20-49, Supplementary Tables 1-3, 6** and **Supplementary Notes 1-5**).

The successful preparation of high-quality 1T'-TMD crystals makes it possible to explore their intrinsic charge transport properties. In a typical experiment, two-terminal device was fabricated on mechanically exfoliated single-layer 1T'-WS₂ nanosheet on SiO₂ (285 nm)/Si substrate (**Supplementary Fig. 50a**). The single-layer 1T'-WS₂ with thickness of ~1.0 nm was confirmed by atomic force microscopy (AFM) (**Supplementary Fig. 50b**). Notably, the electrical transport measurements (**Supplementary Fig. 50c-d**) confirmed the metallic nature of the 1T'-WS₂. Similarly, the 1T'-WSe₂ nanosheet also shows metallic charge transport behaviour (**Supplementary Fig. 51**).

Recently, the exotic superconductivity of ultrathin TMDs with electrostatic carrier accumulation or under high pressure has attracted increasing research interest³⁰⁻³⁴. The electronic properties of TMDs can be tuned from band insulator, superconductor to reentrant insulator using gate voltage³⁵. In particular, a superconducting state can be induced in ultrathin 2H-MoS₂ by heavy electrostatic doping in ionic liquid, yielding the highest critical temperature ($T_c = \sim 12$ K) in TMD-based superconductors³⁶. Extremely high doping concentration exceeding 10^{14} cm⁻² (n_{2D}) through electrical double-layer (EDL) capacitors is often required to reach the superconducting state in thermodynamically stable phase TMDs which have low intrinsic carrier concentrations, including 2H-MoS₂ (REF.^{30,36-38}), 2H-WS₂ (REF.^{35,39,40}) and 1T-SnSe₂ (REF.⁴¹). On the other hand, the metallic TMDs can be obtained from high doping with metal intercalation on 2H-TMDs. For example, the potassium-doped MoS₂ has achieved a T_c of 4.6 K⁴². After additional electrostatic doping in ionic liquid⁴³, superconductivity was also reported in the potassium-

intercalated WS₂ nanotubes at 5.3 K. Moreover, the pressure driven dome-like superconductivity in WTe₂ up to a maximum T_c of 7 K at 16.8 GPa was also observed⁴⁴. Since the group VI 1T'-TMDs are semi-metallic with relatively high carrier concentration, it is promising to study their intrinsic superconducting properties without any carrier modulation and ultrahigh pressure. For example, few-layer 1T-MoS₂ (REF.⁴⁵) and 1T'-MoS₂ (REF.⁸) nanosheets have been reported to exhibit T_c of 0.92 and 4.6 K, respectively.

As a proof-of-concept study, we conducted temperature-dependent electrical transport measurements on 1T'-WS₂, 1T'-WSe₂, and 1T'-WS_{2x}Se_{2(1-x)} ($x = 0.796$ and 0.472) to investigate their intrinsic superconducting properties. **Fig. 4a** shows the temperature-dependent resistivity (ρ - T plots) of 1T'-WS₂ with thickness of 90.1 nm (**Supplementary Fig. 52**), 1T'-WSe₂ with thickness of 71.2 nm (**Supplementary Fig. 53**), 1T'-WS_{2x}Se_{2(1-x)} ($x = 0.796$) with thickness of 14.9 nm (**Supplementary Fig. 54**) and 1T'-WS_{2x}Se_{2(1-x)} ($x = 0.472$) with thickness of 50.2 nm (**Supplementary Fig. 55**) measured by four-probe configuration under zero magnetic field from room temperature to ~ 3.0 K. The positive slopes ($dR/dT > 0$) of the curves (**Fig. 4a**) confirm the metallic charge-transport behavior, which is consistent with the back-gated measurement (**Supplementary Fig. 50d**) and previous reports on semi-metallic TMDs^{3,22}. Like most metals, these ρ - T plots show temperature-independent behavior at low temperature. The residual resistance ratios (RRR which is the ratio of room-temperature resistivity (ρ_{300K}) to the resistivity at lowest temperature in which the resistivity is temperature independent) are 27.42 (at 8.7 K), 48.29 (at 4.0 K), 1.63 (at 4.0 K) and 3.32 (at 4.0 K) for 1T'-WS₂, 1T'-WSe₂, 1T'-WS_{2x}Se_{2(1-x)} ($x = 0.796$) and 1T'-WS_{2x}Se_{2(1-x)} ($x = 0.472$), respectively. The resistivity of 1T'-WS₂ drops sharply from 4.58×10^{-8} at 8.7 K to 1.18×10^{-12} $\Omega \cdot m$ below 8.6 K as shown in the high-

resolution ρ - T plot below 10.0 K in the bottom inset of **Fig. 4a**. This superconducting transition is sharp without any intermediate plateau under zero magnetic field. The superconducting critical temperature, $T_c = 8.6$ K (90% of resistance drop), is among the highest T_c for TMDs reported until now (see **Supplementary Table 7**). It is noteworthy that our 1T'-WSe₂ and 1T'-WS₂xSe_{2(1-x)} ($x = 0.796$ and 0.472) do not undergo a superconducting transition in the measured temperature range down to 3.0 K (**Fig. 4a**).

Furthermore, upon increasing out-of-plane magnetic fields (B_{\perp}), the T_c values of 1T'-WS₂ shift to lower temperatures due to the Meissner effect (**Fig. 4b**). The complete suppression of superconducting behavior occurs in a magnetic field of 2.0 T at 4.0 K. **Fig. 4c** shows the out-of-plane magnetic field-dependent resistivity (ρ - B_{\perp} isotherms) around the transition temperature. Below T_c , the ρ - B_{\perp} isotherms show a broad transition from superconducting state to normal state, and their corresponding critical fields increase with the lowering of temperature. **Fig. 4d** shows the critical fields, B_{c1} and B_{c2} , as a function of T/T_c , in which B_{c1} is the field at which the resistivity deviates from superconducting state (entering of quantized flux), and B_{c2} is the field at which 90% of normal state resistivity is attained. Broadening of these transitions indicates Type-II superconducting behavior. The coherence length, $\xi(0)$ of 10.5 nm is obtained by fitting the critical fields using $B_{c2}(T) = \frac{\phi_0}{2\pi\xi_{GL}(0)^2} \left(1 - \frac{T}{T_c}\right)$ for the out-of-plane magnetic fields, where ϕ_0 is the flux quantum (2.0678×10^{-15} Wb), and $\xi_{GL}(0)$ is the Ginzburg-Landau (GL) in-plane coherence length which quantifies the size of cooper pairs in Bardeen-Cooper-Schrieffer (BCS) theory. The mean free path (l) of the carrier can be written as $l = v_F \tau = \frac{\hbar}{e} (3\pi^2 n)^{1/3} \mu$, where v_F is Fermi velocity of the carrier, τ is the relaxation time, and h is Plank's constant. The l value of 125.37 nm was obtained at a temperature of 10.0 K, just above the T_c , on this 90.1 nm

1T'-WS₂ device with the Hall carrier concentration ($n = 3.18 \times 10^{21} \text{ cm}^{-3}$) and mobility ($\mu = 418 \text{ cm}^2 \text{ V}^{-1} \text{ s}^{-1}$). As expected from the BCS theory for out-of-plane magnetic field, the mean free path is much larger than the coherence length ($l \gg 1.35\xi_{GL}(0)$), indicating the high-quality crystallinity of our as-prepared 1T'-WS₂ crystal and its clean superconductivity³⁴.

Thickness-dependent superconductivity was performed to further reveal the nature of superconductivity of our as-prepared 1T'-WS₂. **Fig. 4e** shows the temperature-dependent normalized electrical resistance (below 10.0 K) of four-probe devices made of 1T'-WS₂ with different thicknesses (152.2, 90.1, 27.2, 6.9, and ~1.0 nm (single layer)). The inset in **Fig. 4e** shows the decrease of T_c from 8.7 K to 5.7 K with thickness reduced from 152.2 nm to single layer. The four-probe 1T'-WS₂ devices all show superconducting transitions and their electrical resistivity reach zero below T_c except the devices made of 1T'-WS₂ with thicknesses of 6.9 and 1.0 nm. **Supplementary Fig. 56** shows the temperature-dependent normalized electrical resistance (below 10.0 K) of additional two-probe devices made of 1T'-WS₂ with thicknesses of 2.5, 3.7 and 6.0 nm. A broad superconducting transition and non-zero resistance of the four-probe device made of single-layer 1T'-WS₂ in the superconducting state was observed (**Fig. 4e** and **Supplementary Fig. 57a**), which could be due to the thermal fluctuations through the formation of vortex-antivortex phases and the high sheet resistance⁴⁶⁻⁴⁸. Such intermediate superconducting transition with non-zero resistivity would occur along with the superconducting-to-insulating transition, when the sheet resistance, $R_{\square} = \rho/t = R^w/l$, is close to or above the quantum sheet resistance, $R_Q = h/(2e)^2 = \sim 6.45 \text{ k}\Omega/\square$, for cooper pairs^{49,50}. **Supplementary Fig. 57c** shows the temperature-dependent sheet resistances (R_{\square}) of these four-probe devices, indicating that

the R_{\square} of 1T'-WS₂ increases as its thickness decreases. At 10.0 K, which is the temperature above the superconducting state, the R_{\square} values of the devices made of 1T'-WS₂ with thicknesses of 27.2, 90.1, and 152.2 nm are 8.9, 0.52, and 0.24 Ω/\square , respectively, which are far below R_Q (~ 6.45 k Ω/\square), and all of these devices show zero resistivity in the superconducting state. When the thickness is further reduced to ~ 1.0 and 6.9 nm, the R_{\square} values at 10.0 K are 1.3 and 0.3 k Ω/\square , respectively, approaching R_Q (~ 6.45 k Ω/\square), thus showing superconducting transition with non-zero resistivity in the superconducting state.

The superconducting-to-insulating transition and non-zero resistance in the superconducting states have also been reported through tuning the sample thickness⁵¹, as well as applying external modulation such as ionic gating⁵² and magnetic fields⁵³. The field-induced superconducting-to-insulating transition (the crossover behavior in the ρ - B_{\perp} plots) has also been observed on the single-layer 1T'-WS₂ (inset of **Supplementary Fig. 57b**). Such magnetic field-induced superconducting-to-insulating transition through a quantum Griffiths state has also been observed in other highly crystalline 2D superconductors, such as ZrNCl and 2H-MoS₂ (REF.⁵⁴).

Supplementary Fig. 57 a-b, 58 a-b, 59 a-d and 60 a, c show the ρ - T plots and ρ - B_{\perp} plots measured under different out-of-plane magnetic fields for devices made of 1T'-WS₂ with different thicknesses. The superconductivity in all devices disappears under the out-of-plane magnetic fields > 3.0 T at 4.0 K due to the Meissner effect. Using GL equation and the out-of-plane upper critical fields, the in-plane coherence lengths, $\xi(0)$, of 10.02, 10.40, 9.62 and 8.85 nm were obtained for the devices made of 1T'-WS₂ with thicknesses of 2.5, 6.0, 6.9 and 152.2 nm, respectively. On the other hand, the superconductivity persists under the in-plane magnetic field of 9.0 T at 4.0 K (**Supplementary Fig. 60 b, d**)

for the 152.2 nm 1T'-WS₂. The anisotropic critical fields (large difference between $B_{c2\parallel}$ and $B_{c2\perp}$) (**Supplementary Fig. 61**), the broader transitions from superconducting-to-normal states in the ρ - B isotherms under in-plane magnetic fields (**Supplementary Fig. 60d**) compared to that under out-of-plane magnetic fields (**Supplementary Fig. 60c**), and the larger coherence length (10.02, 10.40 and 9.62 nm) compared to the respective thickness (2.5, 6.0 and 6.9 nm) of 1T'-WS₂ further confirm the intrinsic 2D features of the superconductivity.

The linear I - V curves (**Supplementary Fig. 62a**) confirm the ohmic nature of the 1T'-WS₂ device in the inset in **Fig. 4a**. The linear curves of Hall voltage (V_H) versus magnetic fields (V_H - B) with negative slopes (**Supplementary Fig. 62b**) show that the dominant carriers in 1T'-WS₂ are holes. **Fig. 4f** illustrates the temperature-dependent carrier concentration (n) and Hall mobility (μ_H) of the 1T'-WS₂ device. Significantly, the carrier concentration in 1T'-WS₂ approaches $\sim 10^{22}$ cm⁻³ at 300.0 K. However, its carrier concentration reaches 3.18×10^{21} cm⁻³ at 10 K, equivalent to 2.87×10^{16} cm⁻² divided by its thickness (90.1 nm), which is much higher than the typical carrier concentration ($\sim 10^{14}$ cm⁻²) in 2D superconductors with gate tuning³⁸. The carrier mobility (**Fig. 4f**) increases with lowering the temperature, and shows a linear trend with $T^{-3/2}$ down to ~ 75.0 K, indicating that acoustic phonon scattering dominates at high temperatures (inset of **Fig. 4f**). The T_c shows a peak with carrier concentration that defines the superconducting dome in gate-tuned TMDs³⁰. It is worth mentioning that although the superconductivity with T_c of 8.6 K was observed in the electrochemically doped K_x WS₂ (REF.⁴⁰) in the carrier concentration range from 0.8×10^{21} cm⁻³ to 4.0×10^{21} cm⁻³, our as-synthesized 1T'-WS₂ is completely potassium-free and hence the superconductivity is intrinsic to the phase-pure

1T'-WS₂. On the other hand, 1T'-WSe₂ and 1T'-WS_{2x}Se_{2(1-x)} do not undergo a superconducting transition in our measurement temperature down to 3.0 K. **Supplementary Fig. 63** shows the transport properties of 1T'-WSe₂, exhibiting hole transport nature and lower carrier concentration compared to 1T'-WS₂. Hence, in our 1T'-WS₂, the metallic character and higher carrier concentration can aid the pairing of Cooper pairs and therefore contribute to the high superconducting T_c of 8.6 K in 1T'-WS₂ with thickness of 90.1 nm. DFT calculations confirm the aforementioned superconductivity arises from the high intrinsic carrier concentration and semi-metallic nature of 1T'-WS₂ (**Supplementary Fig. 64**).

In summary, a facile and general method has been developed to synthesize a series of metastable 1T' phase group VI TMD crystals, including WS₂, WSe₂, WS_{2x}Se_{2(1-x)}, MoS₂, MoSe₂ and MoS_{2x}Se_{2(1-x)}. The precise crystal structures of 1T'-WS₂, 1T'-WSe₂, 1T'-MoS₂ and 1T'-MoSe₂ were solved based on the high-quality crystals. It is worth mentioning that 1T'-WS₂ and 1T'-WSe₂ crystals are thermally stable up to ~117.3 and ~160.1 °C, respectively, which are preferable for the complex device fabrication for a variety of applications. The superconducting transition is found to be 8.6 K and 5.7 K on 1T'-WS₂ with thickness of 90.1 nm and ~1.0 nm (single layer), respectively, placing our as-prepared 1T'-WS₂ among the best reported TMD-based superconductors without any external carrier concentration tuning or high pressure. Based on the experimental results and DFT calculations, such intrinsic superconductivity could be attributed to the high intrinsic carrier concentration and semi-metallic nature of 1T'-WS₂. Our strategy paves the way of phase-engineering of nanomaterials (PEN)⁵⁵ to the preparation of other metastable TMDs

at a large scale and high purity, providing a platform for exploring their phase-dependent physicochemical properties and applications.

References

- 1 Cao, Y. *et al.* Correlated insulator behaviour at half-filling in magic-angle graphene superlattices. *Nature* **556**, 80-84 (2018).
- 2 Cao, Y. *et al.* Unconventional superconductivity in magic-angle graphene superlattices. *Nature* **556**, 43-50 (2018).
- 3 Yu, Y. *et al.* High phase-purity 1T'-MoS₂- and 1T'-MoSe₂-layered crystals. *Nat. Chem.* **10**, 638-643 (2018).
- 4 Chaturvedi, A. *et al.* A universal method for rapid and large-scale growth of layered crystals. *SmartMat* **1**, e1011 (2020).
- 5 Voiry, D., Mohite, A. & Chhowalla, M. Phase engineering of transition metal dichalcogenides. *Chem. Soc. Rev.* **44**, 2702-2712 (2015).
- 6 Tan, C. *et al.* Recent Advances in Ultrathin Two-Dimensional Nanomaterials. *Chem. Rev.* **117**, 6225-6331 (2017).
- 7 Zhang, X., Lai, Z., Ma, Q. & Zhang, H. Novel structured transition metal dichalcogenide nanosheets. *Chem. Soc. Rev.* **47**, 3301-3338 (2018).
- 8 Guo, C. *et al.* Observation of superconductivity in 1T'-MoS₂ nanosheets. *J. Mater. Chem. C* **5**, 10855-10860 (2017).
- 9 Lin, H. *et al.* Growth of environmentally stable transition metal selenide films. *Nat. Mater.*, **18**, 602-607 (2019).
- 10 Zhou, J. *et al.* Large-Area and High-Quality 2D Transition Metal Telluride. *Adv. Mater.* **29**, 1603471 (2017).
- 11 Sung, J. H. *et al.* Coplanar semiconductor–metal circuitry defined on few-layer MoTe₂ via

- polymorphic heteroepitaxy. *Nat. Nanotechnol.* **12**, 1064-1070 (2017).
- 12 Zhou, J. *et al.* A library of atomically thin metal chalcogenides. *Nature* **556**, 355-359 (2018).
- 13 Zhang, H. Ultrathin Two-Dimensional Nanomaterials. *ACS Nano* **9**, 9451-9469 (2015).
- 14 Tan, C. *et al.* Preparation of High-Percentage 1T-Phase Transition Metal Dichalcogenide Nanodots for Electrochemical Hydrogen Evolution. *Adv. Mater.* **30**, 1705509 (2018).
- 15 Wypych, F. & Schollhorn, R. 1T-MoS₂, a new metallic modification of molybdenum disulfide. *J. Chem. Soc., Chem. Commun.*, 1386-1388 (1992).
- 16 Kappera, R. *et al.* Phase-engineered low-resistance contacts for ultrathin MoS₂ transistors. *Nat. Mater.* **13**, 1128-1134 (2014).
- 17 Voiry, D. *et al.* Enhanced catalytic activity in strained chemically exfoliated WS₂ nanosheets for hydrogen evolution. *Nat. Mater.* **12**, 850-855 (2013).
- 18 Zeng, Z. *et al.* Single-Layer Semiconducting Nanosheets: High-Yield Preparation and Device Fabrication. *Angew. Chem. Int. Ed.* **50**, 11093-11097 (2011).
- 19 Mahler, B., Hoepfner, V., Liao, K. & Ozin, G. A. Colloidal Synthesis of 1T-WS₂ and 2H-WS₂ Nanosheets: Applications for Photocatalytic Hydrogen Evolution. *J. Am. Chem. Soc.* **136**, 14121-14127 (2014).
- 20 Sokolikova, M. S., Sherrell, P. C., Palczynski, P., Bemmer, V. L. & Mattevi, C. Direct solution-phase synthesis of 1T' WSe₂ nanosheets. *Nat. Commun.* **10**, 712 (2019).
- 21 Geng, X. *et al.* Pure and stable metallic phase molybdenum disulfide nanosheets for hydrogen evolution reaction. *Nat. Commun.* **7**, 10672 (2016).
- 22 Liu, L. *et al.* Phase-selective synthesis of 1T' MoS₂ monolayers and heterophase bilayers. *Nat. Mater.* **17**, 1108-1114 (2018).
- 23 Lin, Y.-C., Dumcenco, D. O., Huang, Y.-S. & Suenaga, K. Atomic mechanism of the semiconducting-to-metallic phase transition in single-layered MoS₂. *Nat. Nanotechnol.* **9**, 391-396 (2014).

- 24 Duerloo, K.-A. N., Li, Y. & Reed, E. J. Structural phase transitions in two-dimensional Mo- and W-dichalcogenide monolayers. *Nat. Commun.* **5**, 4214 (2014).
- 25 Kang, Y. *et al.* Plasmonic Hot Electron Induced Structural Phase Transition in a MoS₂ Monolayer. *Adv. Mater.* **26**, 6467-6471 (2014).
- 26 Zink, N. *et al.* Selective Synthesis of Hollow and Filled Fullerene-like (IF) WS₂ Nanoparticles via Metal–Organic Chemical Vapor Deposition. *Chem. Mater.* **19**, 6391-6400 (2007).
- 27 Gong, Y. *et al.* Vertical and in-plane heterostructures from WS₂/MoS₂ monolayers. *Nat. Mater.* **13**, 1135-1142 (2014).
- 28 Li, H. *et al.* From Bulk to Monolayer MoS₂: Evolution of Raman Scattering. *Adv. Funct. Mater.* **22**, 1385-1390 (2012).
- 29 Timoshenko, J., Kuzmin, A. & Purans, J. EXAFS study of hydrogen intercalation into ReO₃ using the evolutionary algorithm. *J. Phys.: Condens. Matter* **26**, 055401 (2014).
- 30 Ye, J. T. *et al.* Superconducting Dome in a Gate-Tuned Band Insulator. *Science* **338**, 1193-1196 (2012).
- 31 Fatemi, V. *et al.* Electrically tunable low-density superconductivity in a monolayer topological insulator. *Science* **362**, 926-929 (2018).
- 32 Sajadi, E. *et al.* Gate-induced superconductivity in a monolayer topological insulator. *Science* **362**, 922-925 (2018).
- 33 Chi, Z. *et al.* Superconductivity in Pristine 2H_a-MoS₂ at Ultrahigh Pressure. *Phys. Rev. Lett.* **120**, 037002 (2018).
- 34 Saito, Y., Nojima, T. & Iwasa, Y. Highly crystalline 2D superconductors. *Nat. Rev. Mater.* **2**, 16094 (2016).
- 35 Lu, J. *et al.* Full superconducting dome of strong Ising protection in gated monolayer WS₂. *Proc. Natl. Acad. Sci.* **115**, 3551-3556 (2018).
- 36 Costanzo, D., Jo, S., Berger, H. & Morpurgo, A. F. Gate-induced superconductivity in

- atomically thin MoS₂ crystals. *Nat. Nanotechnol.* **11**, 339 (2016).
- 37 Lu, J. M. *et al.* Evidence for two-dimensional Ising superconductivity in gated MoS₂. *Science* **350**, 1353-1357 (2015).
- 38 Taniguchi, K., Matsumoto, A., Shimotani, H. & Takagi, H. Electric-field-induced superconductivity at 9.4 K in a layered transition metal disulphide MoS₂. *Appl. Phys. Lett.* **101**, 042603 (2012).
- 39 Jo, S., Costanzo, D., Berger, H. & Morpurgo, A. F. Electrostatically Induced Superconductivity at the Surface of WS₂. *Nano Lett.* **15**, 1197-1202 (2015).
- 40 Shi, W. *et al.* Superconductivity Series in Transition Metal Dichalcogenides by Ionic Gating. *Sci. Rep.* **5**, 12534 (2015).
- 41 Zeng, J. *et al.* Gate-Induced Interfacial Superconductivity in 1T-SnSe₂. *Nano Lett.* **18**, 1410-1415 (2018).
- 42 Zhang, R. *et al.* Superconductivity in Potassium-Doped Metallic Polymorphs of MoS₂. *Nano Lett.* **16**, 629-636 (2016).
- 43 Qin, F. *et al.* Diameter-Dependent Superconductivity in Individual WS₂ Nanotubes. *Nano Lett.* **18**, 6789-6794 (2018).
- 44 Pan, X.-C. *et al.* Pressure-driven dome-shaped superconductivity and electronic structural evolution in tungsten ditelluride. *Nat. Commun.* **6**, 7805 (2015).
- 45 Sharma, C. H., Surendran, A. P., Varma, S. S. & Thalakulam, M. 2D superconductivity and vortex dynamics in 1T-MoS₂. *Commun. Phys.* **1**, 90 (2018).
- 46 Cui, J. *et al.* Transport evidence of asymmetric spin-orbit coupling in few-layer superconducting 1T_d-MoTe₂. *Nat. Commun.* **10**, 2044 (2019).
- 47 Beasley, M. R., Mooij, J. E. & Orlando, T. P. Possibility of Vortex-Antivortex Pair Dissociation in Two-Dimensional Superconductors. *Phys. Rev. Lett.* **42**, 1165-1168 (1979).
- 48 Skocpol, W. J. & Tinkham, M. Fluctuations near superconducting phase transitions. *Rep. Prog. Phys.* **38**, 1049-1097 (1975).

- 49 Fan, Y. J. *et al.* Quantum superconductor-insulator transition in titanium monoxide thin films with a wide range of oxygen contents. *Phys. Rev. B* **98**, 064501 (2018).
- 50 Jaeger, H. M., Haviland, D. B., Orr, B. G. & Goldman, A. M. Onset of superconductivity in ultrathin granular metal films. *Phys. Rev. B* **40**, 182-196 (1989).
- 51 Yan, R. *et al.* Thickness dependence of superconductivity in ultrathin NbS₂. *Appl. Phys. Express* **12**, 023008 (2019).
- 52 Saito, Y., Kasahara, Y., Ye, J., Iwasa, Y. & Nojima, T. Metallic ground state in an ion-gated two-dimensional superconductor. *Science* **350**, 409-413 (2015).
- 53 Hebard, A. F. & Paalanen, M. A. Magnetic-field-tuned superconductor-insulator transition in two-dimensional films. *Phys. Rev. Lett.* **65**, 927-930 (1990).
- 54 Saito, Y., Nojima, T. & Iwasa, Y. Quantum phase transitions in highly crystalline two-dimensional superconductors. *Nat. Commun.* **9**, 778 (2018).
- 55 Chen, Y. *et al.* Phase engineering of nanomaterials. *Nat. Rev. Chem.* **4**, 243-256 (2020).

Methods

Chemicals. Potassium tungsten oxide (K₂WO₄, 99.5%) was purchased from Alfa Aesar (USA). Potassium molybdate (K₂MoO₄, 98%), sulfur powder (S, 99.98%), selenium powder (Se, 100 mesh, ≥99.5%) and acetonitrile (anhydrous, 99.8%) were purchased from Sigma-Aldrich (Germany). Iodine (I₂, 98.0%) was purchased from Tokyo Chemical Industry Company Limited (Japan). Hydrogen/argon gas mixture (20% H₂ / 80% Ar) and purified argon (Ar, 99.9%) were purchased from Leeden National Oxygen Limited (Singapore). The Milli-Q water obtained from the Milli-Q purification system (Millipore Corporation of Billerica, Massachusetts, USA) was used in all experiments.

Synthesis of 1T'-WS₂ crystals. In a typical procedure, K₂WO₄ and S powders with molar

ratio of 1:4 and a total weight of 1.0 g were mixed and then ground for 10 min using a mortar. The obtained homogeneous mixture was subsequently transferred to a quartz ampoule, which was sealed under the internal pressure of about 10^{-6} - 10^{-5} Torr. In a box furnace, the temperature of sealed quartz ampoule was increased from room temperature to 500 °C in about 6 h, which was then maintained for 96 h, and cooled down gradually. After that, the precursor for preparation of 1T'-WS₂ crystals was obtained. Next, 500 mg of the prepared precursor was loaded into an alumina crucible in the middle of the quartz tube with a diameter of 6 cm. The tube was vacuumed and refilled with Ar for 3 times. After that, the tube was purged with H₂/Ar mixed gas (20% H₂ / 80% Ar) with a flow rate of 200 s.c.c.m (standard cubic centimeter per minute) for 15 min. Then, it was placed into the preheated furnace at 750 °C. The reaction was maintained for 10 h before the furnace power was turned off and the temperature was quickly ramped down to room temperature. The resulting product was washed with Milli-Q water thoroughly until the pH value of the suspension reached 7-8. After the product was stored in Milli-Q water for 24 h, it was transferred into an I₂ acetonitrile solution (4 mmol, 15 ml) for another 24 h to completely remove the K residues, followed by washing with Milli-Q water twice. Finally, the 1T'-WS₂ crystals were obtained by drying in a vacuum oven at room temperature.

Synthesis of 1T'-WSe₂ crystals. The synthesis of 1T'-WSe₂ crystals is different from that of 1T'-WS₂ due to the low reactivity of Se with K₂WO₄. Typically, Se powder was used to replace S powder in the synthetic process. In addition, the heating temperature used for the reaction of precursor was 700 °C, instead of 500 °C used in the preparation of 1T'-WS₂ crystals. Importantly, additional 500 mg of Se powder was mixed with 500 mg of prepared precursor to form a homogeneous mixture. The mixture was then heated at 450 °C for 90

min before the temperature was rapidly increased to 850 °C in about 15 min and then maintained for 10 h. After reaction, the shiny products grown on the surface of alumina crucible were collected and processed with the similar post-treatment used for the preparation of 1T'-WS₂ crystals. Finally, the 1T'-WSe₂ crystals were obtained after drying in vacuum oven for 24 h.

Synthesis of 1T'-WS_{2x}Se_{2(1-x)} ternary crystals. 1T'-WS_{2x}Se_{2(1-x)} crystals were prepared using the similar method for the preparation of 1T'-WSe₂ crystals. Here, mixtures of K₂WO₄ with various ratios of S and Se powder were used as the starting materials to prepare the precursor. The temperature used for the reaction to prepare precursor was 650 °C. The prepared precursors were then mixed with the same amount of extra Se powder to synthesize the ternary 1T'-WS_{2x}Se_{2(1-x)} crystals using the similar reaction condition that was used for the synthesis of 1T'-WSe₂ crystals.

Synthesis of 1T'-MoS₂ and 1T'-MoSe₂ crystals. The synthetic procedures for 1T'-MoS₂ and 1T'-MoSe₂ were similar to that used for the synthesis of 1T'-WS₂ and 1T'-WSe₂, respectively, except that K₂WO₄ was replaced with K₂MoO₄.

Synthesis of 1T'-MoS_{2x}Se_{2(1-x)} ternary crystals. 1T'-MoS_{2x}Se_{2(1-x)} crystals were prepared by using the similar method for preparation of 1T'-MoS₂ crystals. Mixtures of K₂MoO₄ with various ratios of S and Se powder were used as the starting materials to prepare the precursors. The prepared precursors were then used to synthesize ternary 1T'-MoS_{2x}Se_{2(1-x)} crystals via the similar reaction condition that was used for the synthesis of 1T'-MoS₂ crystals.

Preparation of 2H-WS₂, -WSe₂, -WS_{2x}Se_{2(1-x)}, -MoS₂, -MoSe₂ and -MoS_{2x}Se_{2(1-x)} crystals. All the 2H-TMD crystals were obtained by annealing the corresponding as-

prepared 1T'-TMD crystals at temperature of 400 °C under Ar for 4 h.

Fabrication of 1T'-WS₂, 1T'-WSe₂ and 1T'-WS_{2-x}Se_{2(1-x)} (x = 0.796 and 0.472) devices.

Two-terminal devices: 1T'-WS₂ or 1T'-WSe₂ nanosheets were mechanically exfoliated and placed on a freshly cleaned SiO₂ (285 nm)/Si substrate, which was then spin-coated with poly(methyl methacrylate) (PMMA 495, A8, Microchem) at 3500 rpm followed by baking on a hotplate at 80 °C for 5 min. Finally, e-beam lithography (Raith PIONEER TWO) was used to define two electrodes at a dosage of 250 μC/cm², followed by the thermal evaporation of Cr (5 nm)/Au (70 nm) (PVD 75, Kurt. J. Lesker) as metal contacts.

Multi-terminal devices: Large rectangular 1T'-WS₂ nanosheets (> 200 μm²) were obtained by the previously reported dry-transfer method⁵⁶. Briefly, a poly(L-lactic acid) (PLLA) film was spin-coated on the mechanically exfoliated 1T'-WS₂ nanosheets on a freshly cleaned SiO₂ (285 nm)/Si substrate followed by baking on a hotplate at 50 °C. Then a Polydimethylsiloxane (PDMS) film was brought into conformal contact with the polymer film and a small water droplet (~30 μL) was introduced at one exposed hydrophilic edge of the SiO₂/Si substrate to separate the PDMS/PLLA/1T'-WS₂ film from the hydrophilic SiO₂/Si substrate. The obtained PDMS/PLLA/1T'-WS₂ film was covered on the target SiO₂ (285 nm)/Si chip followed by peeling off the PDMS at 50 °C and dissolving PLLA in dichloromethane to leave 1T'-WS₂ nanosheets on the target chip, which was then spin-coated with poly(methyl methacrylate) (PMMA 495, A8, Microchem) at 3500 rpm followed by baking on a hotplate at 80°C for 5 min. E-beam lithography (Raith PIONEER TWO) was used to define the multiple electrodes at a dosage of 250 μC/cm², followed by thermal evaporation of Cr (5 nm)/Au (50 nm) (PVD 75, Kurt. J. Lesker) as metal contacts. Atomic force microscope (Dimension 5000, Bruker) was used to characterize the

thicknesses of 1T'-WS₂ nanosheets after all the superconducting measurements were completed. It is worth mentioning that the aforementioned procedures can also be used to prepare other multi-terminal devices made of 1T'-WSe₂ or 1T'-WS₂_xSe_{2(1-x)} ($x = 0.796$ or 0.472).

Electrical transport measurements. The temperature-dependent electrical resistivity (ρ - T) and field-dependent electrical resistivity (ρ - B) down to 4.0 K were measured using the Physical Property Measurement System (PPMS, Quantum Design, USA). The home-built multifunctional probes were used for electrical resistivity measurements under out-of-plane and in-plane magnetic fields using SRS 830 Lock in amplifiers along with PPMS. The isotherms of current versus voltage (I - V) plots and the Hall voltage versus B_{\perp} were used to calculate the carrier concentration and mobility.

Characterizations. Transmission electron microscope (TEM) images and energy-dispersive X-ray spectroscopy (EDS) spectra were obtained with JEOL JEM-2100F (JEOL, Tokyo, Japan) transmission electron microscope. High-angle annular dark-field (HAADF) scanning transmission electron microscope (STEM) images were captured with JEOL ARM200F (JEOL, Tokyo, Japan) transmission electron microscope equipped with a cold field emission gun and double hexapole C_s correctors (CEOS GmbH, Heidelberg, Germany). All the TEM instruments were operated at the accelerating voltage of 200 kV. Scanning electron microscope (SEM) images were taken with a field-emission scanning electron microscope (FESEM, JSM 7600F) equipped with an EDS detector. Powder X-ray diffraction (XRD) patterns in reflection mode were collected with Bruker D8 ADVANCE X-ray powder diffractometer and XRD patterns in transmission mode were collected with Bruker D8 DISCOVERY X-ray powder diffractometer, both using Cu $K\alpha$ radiation

(operated at 40 kV and 40 mA). Single-crystal X-ray diffraction (SCXRD) data were collected at 100 K with a Bruker-APEX II X-ray diffractometer equipped with a large area CCD detector using graphite monochromated Mo K α radiation ($\lambda = 0.71073 \text{ \AA}$). Absorption corrections were applied by using the multi-scan program. These structures were solved and refined using a SHELXTL Software Package. Anisotropic thermal parameters were applied to all atoms. Atomic force microscope (AFM) images were captured with Bruker Dimension 5000 AFM under tapping mode. Differential scanning calorimeter (DSC) measurements were carried out using Discovery DSC (TA Instruments) under N₂ at heating rate of 5 °C min⁻¹. Thermogravimetric analysis (TGA) was performed using Q500 TGA (TA Instruments) under N₂ at heating rate of 5 °C min⁻¹. X-ray photoelectron spectroscopy (XPS) data was obtained with VG ESCALAB 220i-XL system (base pressure 5×10^{-10} mbar) equipped with monochromatic Al K α (1486.7 eV) X-ray source. All XPS spectra were calibrated according to the C1s peak located at 284.5 eV. Raman spectra were recorded using WITec system (Germany) with excitation wavelength of 532 nm and power of 0.1 mW. Auger electron spectroscopy (AES) measurements were conducted on a JEOL JAMP-7830F machine equipped with a field-emission electron gun and a hemispherical analyzer. The specimens for AES depth profiling were prepared by drop-casting the ethanolic solution of the as-prepared 1T'-WS₂ crystals on a Si substrate. The secondary electron imaging and AES scanning were performed at an acceleration voltage of 10 keV and a probe current of 10×10^{-9} A. The sample was tilted at 30° during the measurement. Prior to depth profiling, the survey AES spectra were obtained on the 1T'-WS₂ over a range of 0-2000 eV with a step size of 1 eV and a dwell time of 100 ms. Floating micro-ion etching device (FMIED) delivering an ion beam of 500 eV Ar⁺ was

used to sputter the sample surface over an area of $1.5 \times 1.5 \text{ mm}^2$ for depth profiling. Each cycle in the depth profiling started with a 60 s sputtering step, followed by the acquisition of narrow AES spectra of all elements of interest (1 eV step size and 100 ms dwell time). This procedure was terminated only after the stable Si signal was detected, indicating 1T'-WS₂ was etched out. Superconductivity was measured using Physical Property Measurement System (PPMS, Quantum Design USA) in four-probe device configuration. The X-ray absorption near edge structure (XANES) and the extended X-ray absorption fine structure (EXAFS) measurements of W L₃-edge were performed at the XAFCA beamline of Singapore Synchrotron Light Source (SSLS)⁵⁷. The storage ring of SSLS operated at E = 700 MeV and I_{max} = 200 mA. The X-ray radiation was monochromatized by the Si (111) double-crystal monochromator. W metal powder was used as a reference for energy calibration, and all samples were measured in the transmission mode at room temperature. Data processing was carried out using the Demeter software package⁵⁸ and data fitting was based on the evolutionary algorithm using EvAX code developed by Janis Timoshenko²⁹.

Density functional theory calculations.

Calculations of Raman active modes: Density functional theory (DFT) calculations were performed using the projector augmented wave (PAW) method⁵⁹ as implemented in the Vienna ab initio simulation package (VASP)^{60,61}. The generalized gradient approximation in the Perdew-Burke-Ernzerhof (PBE) form^{62,63} and a cut-off energy of 400 eV for plane-wave basis set were adopted. The Brillouin zones were sampled by a Monkhorst-Pack k-point mesh of $16 \times 8 \times 4$. The convergence thresholds were 10^{-8} eV and 10^{-5} eV/Å for energy and force, respectively. To simulate the Raman activities of 1T'-WS₂ and 1T'-WSe₂, their dielectric susceptibility tensor and phonons at the Γ -point were computed following

the approach proposed by Porezag and Pederson⁶⁴, as implemented in the `vasp_raman.py` code (`vasp_raman.py`. <https://github.com/raman-sc/VASP/>: 2013).

Calculations of superconducting transitions: Crystal structure models of bulk transition metal dichalcogenides (2H-WS₂ and 1T'-WS₂) and single-layer 1T'-WS₂ were fully optimized by using DFT calculations. Electronic band structure and projected density of states (PDOS) calculations were performed using the Vienna Ab initio Simulation Package (VASP)⁶⁰. The electron-ion interaction was described by Projector-Augmented-Wave potentials with the $6s^25d^4$ and $3s^23p^4$ configurations treated as valence electrons for W and S, respectively⁵⁹. The Perdew-Burke-Ernzerhof generalized gradient approximation was chosen for the exchange-correlation functional, and kinetic cutoff energy of 800 eV and Monkhorst-Pack k meshes with grid spacing of $2\pi \times 0.03 \text{ \AA}^{-1}$ were adopted to ensure the energy converges to be better than 1 meV/atom^{65,66}. Lattice-dynamical properties and the Eliashberg spectral function were calculated using density functional perturbation theory (DFPT)⁶⁷, performed with the Quantum-ESPRESSO code⁶⁸. Norm-conserving pseudopotentials were used with a kinetic energy cutoff of 80 Ry, and the charge density was integrated on a Γ -centered $10 \times 6 \times 4$ k -point mesh⁶⁹. A Methfessel-Paxton first-order smearing of 0.02 Ry was applied. The first-order potential perturbation and dynamical matrices were calculated using DFPT on an irreducible $5 \times 3 \times 2$ Γ -centered q -point mesh. Electron-phonon couplings (EPC) constant λ and superconducting transition temperature T_c were obtained by direct solution of the Eliashberg equation⁷⁰.

Acknowledgements

H.Z. thanks the support from ITC via the Hong Kong Branch of National Precious Metals

Material Engineering Research Center (NPMM), the Start-Up Grant (Project No.9380100) and the grants (Project Nos. 9610478 and 1886921) from the City University of Hong Kong, and the Science Technology and Innovation Committee of Shenzhen Municipality (grant no. JCYJ20200109143412311). Q.H. acknowledges the funding support from the Start-Up Grant (Project No.9610482) from the City University of Hong Kong. Y.S. and Y.M. acknowledge the funding support from the National Natural Science Foundation of China (under Grants No.11534003) and Program for JLU Science and Technology Innovative Research Team and Science Challenge Project (No.TZ2016001). K.H. and D.V.M.R. acknowledge funding from the Accelerated Materials Development for Manufacturing Program at A*STAR via the AME Programmatic Fund by the Agency for Science, Technology and Research under Grant No. A1898b0043. R.V.R. and V.S. acknowledge the support by grants from the National Research Foundation, Prime Minister's Office, Singapore under its Campus for Research Excellence and Technological Enterprise (CREATE) program. We also would like to thank Prof. Wypych Fernando for his generousness to provide us his PhD thesis for our reference and Dr. Samuel Morris for the helpful discussion. We would like to acknowledge the Facility for Analysis, Characterization, Testing and Simulation, Nanyang Technological University, Singapore, for use of their electron microscopy (and/or X-ray) facilities.

Author contributions

H.Z. proposed the research direction and guided the project. Z.L. designed and performed the synthesis and characterizations of all the materials. Q.H., W.Z. and Z.S. fabricated and tested the devices. T.H.T. and D.H. helped to synthesize the materials and performed some

characterizations. D.V.M.R., Q.H., A.C., V.S., R.V.R. and K.H. performed the superconductivity measurements on the devices and analyzed the results. Y.S. and Y.M. performed the DFT calculations on the electronic structures and superconducting gap of the materials. S.X. carried out the X-ray absorption fine structure (XAFS) measurements and analyzed the data. Y.L. performed the single crystal X-ray diffraction (SCXRD) measurements and D.-D.Z. refined the data to solve the crystal structures. B.C. carried out the aberration-corrected high-angle annular dark field scanning transmission electron microscopy (HAADF-STEM) imaging of the samples. G.N. performed the Raman measurements of materials. C.L. performed the calculations on the Raman active modes and analyzed the Raman data. D.-D.Z. and Z.H. helped to perform X-ray diffraction (XRD) test on materials. B.L. and Y.C. performed the X-ray photoelectron spectroscopy (XPS) tests. C.T., Z.Z., Y.Y. and X.R.W. helped to analyze the structure information of the materials. Z.L., Q.H., D.V.M.R., K.H. and H.Z. drafted the manuscript. All authors analyzed and discussed the experimental results, and checked the manuscript.

Competing interests

The authors declare no competing interests.

Data availability

The X-ray crystallographic coordinates for the structure reported in this study have been deposited at the Cambridge Crystallographic Data Centre under deposition numbers CCDC 2062455, 2062456, 2062457 and 2062458. These data can be obtained free of charge from <https://www.ccdc.cam.ac.uk/structures/>. Other data that support the findings of this study

are available from the corresponding author upon reasonable request.

References

- 56 Li, H. *et al.* A Universal, Rapid Method for Clean Transfer of Nanostructures onto Various Substrates. *ACS Nano* **8**, 6563-6570 (2014).
- 57 Du, Y. *et al.* XAFCA: a new XAFS beamline for catalysis research. *J. Synchrotron Rad.* **22**, 839-843 (2015).
- 58 Ravel, B. & Newville, M. ATHENA, ARTEMIS, HEPHAESTUS: data analysis for X-ray absorption spectroscopy using IFEFFIT. *J. Synchrotron Rad.* **12**, 537-541 (2005).
- 59 Blöchl, P. E. Projector augmented-wave method. *Phys. Rev. B* **50**, 17953-17979 (1994).
- 60 Kresse, G. & Furthmüller, J. Efficient iterative schemes for ab initio total-energy calculations using a plane-wave basis set. *Phys. Rev. B* **54**, 11169-11186 (1996).
- 61 Kresse, G. & Joubert, D. From ultrasoft pseudopotentials to the projector augmented-wave method. *Phys. Rev. B* **59**, 1758-1775 (1999).
- 62 Perdew, J. P. & Wang, Y. Accurate and simple analytic representation of the electron-gas correlation energy. *Phys. Rev. B* **45**, 13244-13249 (1992).
- 63 Perdew, J. P. *et al.* Atoms, molecules, solids, and surfaces: Applications of the generalized gradient approximation for exchange and correlation. *Phys. Rev. B* **46**, 6671-6687 (1992).
- 64 Porezag, D. & Pederson, M. R. Infrared intensities and Raman-scattering activities within density-functional theory. *Phys. Rev. B* **54**, 7830-7836 (1996).
- 65 Perdew, J. P. & Wang, Y. Pair-distribution function and its coupling-constant average for the spin-polarized electron gas. *Phys. Rev. B* **46**, 12947-12954 (1992).
- 66 Perdew, J. P., Burke, K. & Ernzerhof, M. Generalized Gradient Approximation Made Simple. *Phys. Rev. Lett.* **77**, 3865-3868 (1996).
- 67 Baroni, S., de Gironcoli, S., Dal Corso, A. & Giannozzi, P. Phonons and related crystal

- properties from density-functional perturbation theory. *Rev. Mod. Phys.* **73**, 515-562 (2001).
- 68 Paolo, G. *et al.* QUANTUM ESPRESSO: a modular and open-source software project for quantum simulations of materials. *J. Phys.: Condens. Matter* **21**, 395502 (2009).
- 69 Hamann, D. R., Schlüter, M. & Chiang, C. Norm-Conserving Pseudopotentials. *Phys. Rev. Lett.* **43**, 1494-1497 (1979).
- 70 Allen, P. B. & Mitrović, B. in *Solid State Physics* Vol. 37 (eds Henry Ehrenreich, Frederick Seitz, & David Turnbull) 1-92 (Academic Press, 1983).

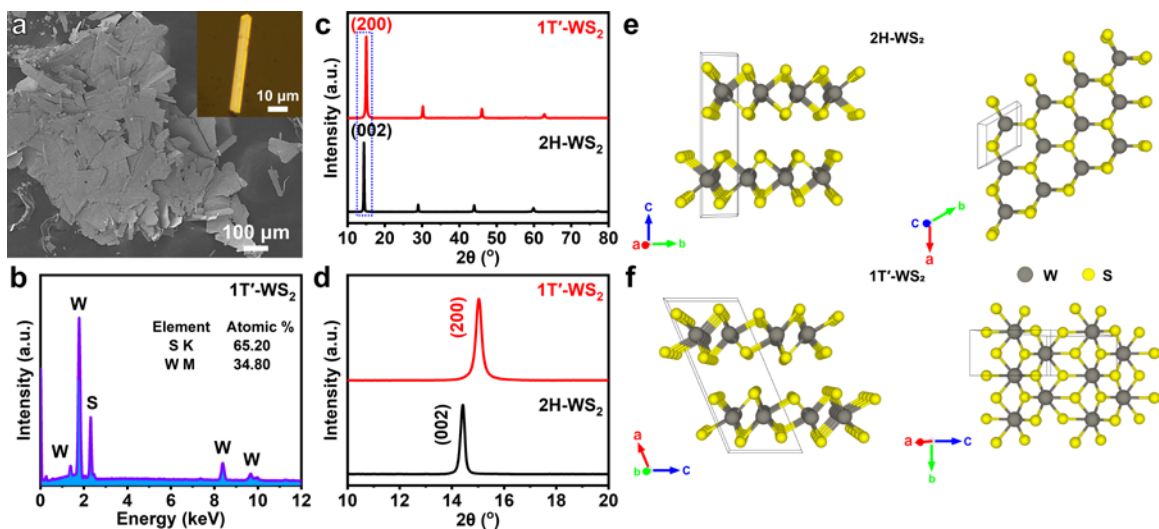


Fig. 1 | Crystal structure and characterization of WS₂. **a**, SEM image of the as-prepared 1T'-WS₂ crystals. Inset: optical image of a 1T'-WS₂ crystal. **b**, EDS spectrum of the as-prepared 1T'-WS₂ crystals obtained under SEM mode. **c**, XRD patterns of 1T'-WS₂ crystals, and 2H-WS₂ crystals obtained by annealing 1T'-WS₂ crystals. **d**, Magnified XRD patterns of the (200) peak of 1T'-WS₂ and (002) peak of 2H-WS₂ crystals from the blue dashed area in (c). **e, f**, Schematic illustration of structures of (e) 2H-WS₂ and (f) 1T'-WS₂. Left panel: side view of the structure; right panel: top view of a typical single-layer. The areas marked by black lines represent the unit cells of WS₂.

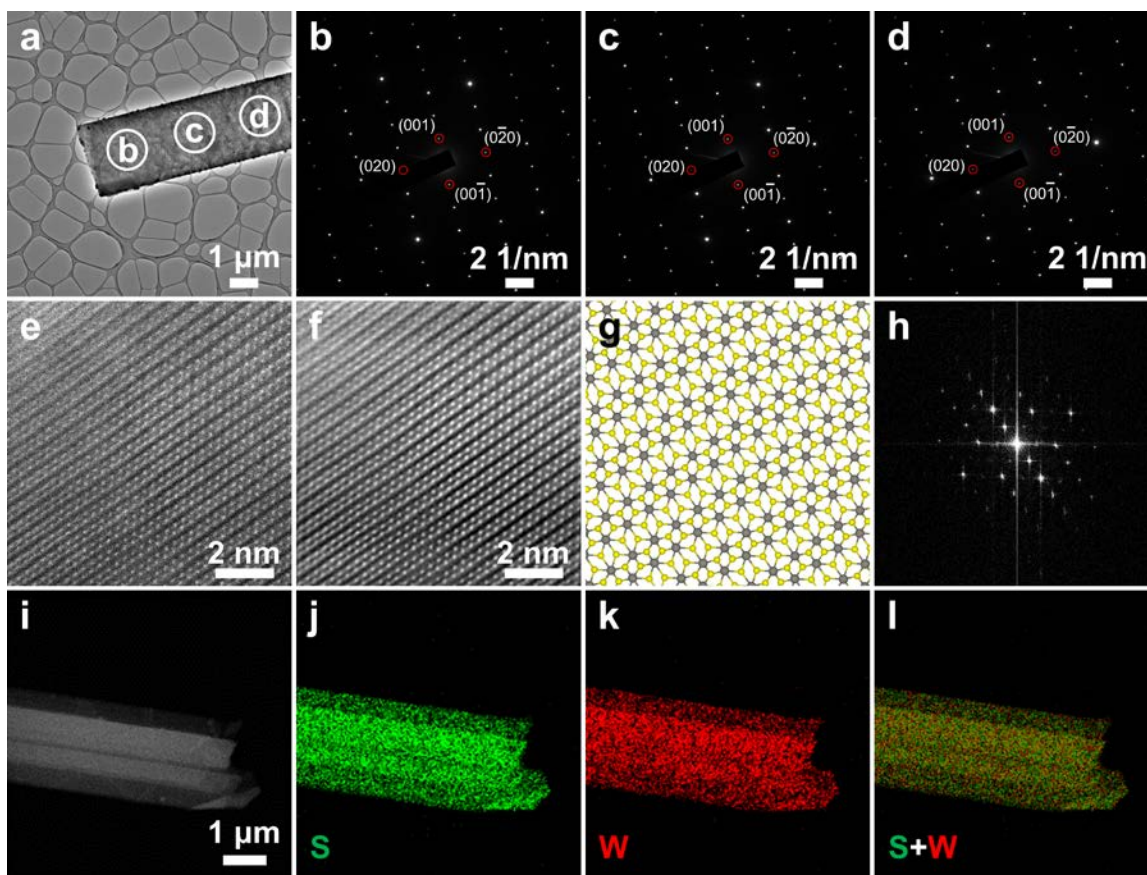


Fig. 2 | Structure characterization of 1T'-WS₂. **a**, TEM image of a single 1T'-WS₂ flake. **b-d**, SAED patterns obtained from the corresponding areas in **(a)**. **e**, HAADF-STEM image obtained from a 1T'-WS₂ flake. **f**, Fast Fourier transform (FFT) filtered image of **(e)**. **g**, Simulated 1T'-WS₂ structure showing the same crystal orientation as that in **(f)**. The grey balls represent W atoms, and the yellow balls represent S atoms. **h**, Corresponding FFT pattern obtained from the HAADF-STEM image in **(e)**. **i-l**, **(i)** Dark-field STEM image and **(j-l)** elemental mapping images of the as-prepared 1T'-WS₂ flake: **(j)** S K signals, **(k)** W L signals, and **(l)** overlap of S K and W L signals.

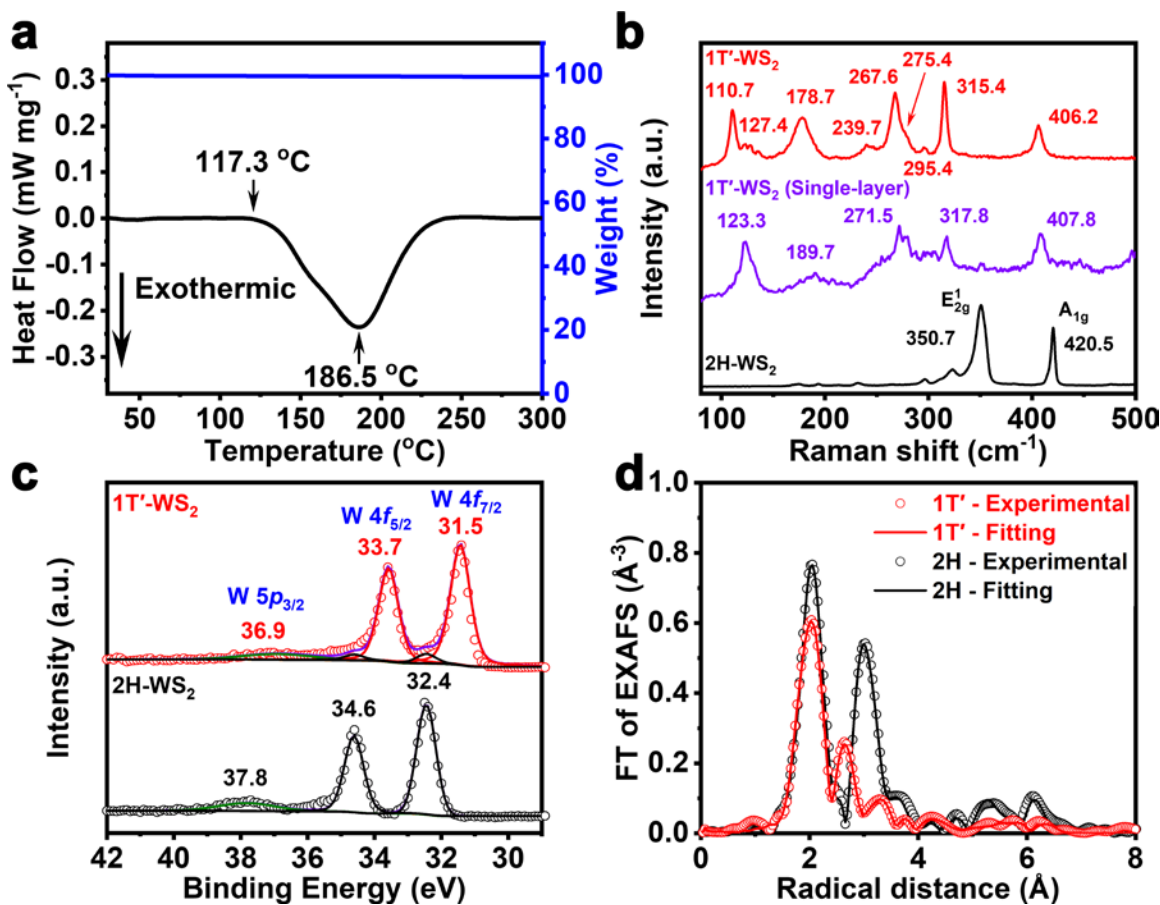


Fig. 3 | Characterization of 1T'- and 2H-WS₂. **a**, TGA-DSC curves of the as-prepared 1T'-WS₂ crystals. **b**, Raman spectra of the as-prepared 1T'-WS₂ crystals, mechanically exfoliated single-layer 1T'-WS₂, and 2H-WS₂ crystals obtained by annealing 1T'-WS₂ crystals. **c**, Experimental (dots) and fitting (curves) high-resolution XPS W 4f spectra of 1T'-WS₂ and 2H-WS₂ obtained by annealing 1T'-WS₂ crystals. The red and black deconvoluted peaks of W 4f belong to the 1T' and 2H phases, respectively. **d**, Experimental (dots) and fitting (curves) Fourier transforms of W L₃-edge EXAFS spectra of the as-prepared 1T'-WS₂ and 2H-WS₂ crystals based on evolutionary algorithm.

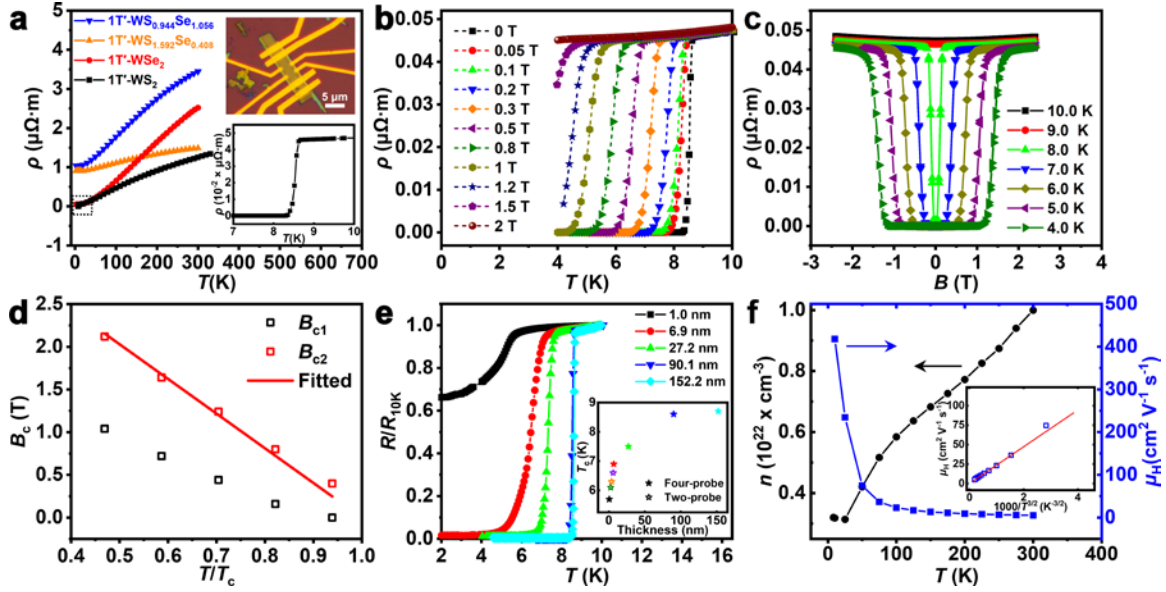


Fig. 4 | Device configuration and electrical transport properties of devices made of 1T'-WS₂ (90.1 nm), 1T'-WSe₂ (71.2 nm), 1T'-WS_{2x}Se_{2(1-x)} ($x = 0.796$) (14.9 nm), and 1T'-WS_{2x}Se_{2(1-x)} ($x = 0.472$) (50.2 nm). **a**, Temperature-dependent electrical resistivity (ρ - T) of the mechanically exfoliated 1T'-WS₂, 1T'-WSe₂ and 1T'-WS_{2x}Se_{2(1-x)} ($x = 0.796$ and 0.472) without magnetic field. Insets: (Top) optical image of the 1T'-WS₂ device with four-probe configuration and Hall bars; (Bottom) high-resolution ρ - T plot of 1T'-WS₂ around T_c shown in the black dotted area. **b**, ρ - T plots of the 1T'-WS₂ device in (a) under different out-of-plane magnetic fields (B_{\perp}). **c**, ρ - B_{\perp} isotherms under out-of-plane magnetic fields measured at $T = 10.0$ and 9.0 K for $T > T_c$, and $T = 8.0, 7.0, 6.0, 5.0$ and 4.0 K for $T < T_c$. **d**, Critical magnetic fields, B_{c1} and B_{c2} , as a function of T/T_c . **e**, R/R_{10K} plots of four-probe devices made of 1T'-WS₂ nanosheets with different thicknesses. Inset: superconducting transition temperature of two- and four-probe devices of 1T'-WS₂ nanosheets with different thicknesses. **f**, Plots of temperature-dependent carrier concentration (n) and carrier Hall mobility (μ_H) obtained from the 1T'-WS₂ device in (a). Inset: plot of the carrier Hall mobility as a function of $T^{3/2}$.

Metastable 1T'-phase group VI transition metal dichalcogenide crystals

Zhuangchai Lai,^{1,2†} Qiyuan He,^{3†} Thu Ha Tran,^{2†} D. V. Maheswar Repaka,^{4†} Dong-Dong Zhou,⁵ Ying Sun,^{6,7} Shibo Xi,⁴ Yongxin Li,⁸ Apoorva Chaturvedi,² Chaoliang Tan,⁹ Bo Chen,¹ Gwang-Hyeon Nam,² Bing Li,¹⁰ Chongyi Ling,¹ Wei Zhai,¹ Zhenyu Shi,^{1,2} Diany Hu,² Vinay Sharma,² Zhaoning Hu,² Ye Chen,¹¹ Zhicheng Zhang,^{2,12} Yifu Yu,^{2,13} Xiao Renshaw Wang,^{8,14} Raju V. Ramanujan,² Yanming Ma,^{6,7,15} Kedar Hippalgaonkar,^{2,4*} Hua Zhang^{1,16,17*}

¹Department of Chemistry, City University of Hong Kong, Kowloon, Hong Kong, China.

²Center for Programmable Materials, School of Materials Science and Engineering, Nanyang Technological University, 50 Nanyang Avenue, Singapore 639798, Singapore.

³Department of Materials Science and Engineering, City University of Hong Kong, Kowloon, Hong Kong, China.

⁴Institute of Materials Research and Engineering (IMRE), A*STAR (Agency for Science, Technology and Research), Singapore 138634, Singapore.

⁵MOE Key Laboratory of Bioinorganic and Synthetic Chemistry, School of Chemistry, Sun Yat-Sen University, Guangzhou 510275, China.

⁶State Key Laboratory of Superhard Materials, College of Physics, Jilin University, Changchun 130012, China.

⁷Innovation Center for Computational Physics Methods and Softwares, College of Physics, Jilin University, Changchun 130012, China.

⁸School of Physical and Mathematical Sciences, Nanyang Technological University, 637371 Singapore, Singapore.

⁹Department of Electrical Engineering, City University of Hong Kong, Kowloon, Hong Kong, China.

¹⁰School of Chemistry and Chemical Engineering, Harbin Institute of Technology, Harbin 150001, China.

¹¹Department of Chemistry, The Chinese University of Hong Kong, Shatin, N.T., Hong Kong, China

¹²Tianjin Key Laboratory of Molecular Optoelectronic Sciences, Department of Chemistry, School of Science, Tianjin University & Collaborative Innovation Center of Chemical Science and Engineering, Tianjin 300072, China.

¹³Institute of Molecular Plus, Tianjin University, Tianjin 300354, China.

¹⁴School of Electrical and Electronic Engineering, Nanyang Technological University, 639798 Singapore, Singapore.

¹⁵International Center of Future Science, Jilin University, Changchun 130012, China.

¹⁶Hong Kong Branch of National Precious Metals Material Engineering Research Center (NPMM), City University of Hong Kong, Kowloon, Hong Kong, China.

¹⁷Shenzhen Research Institute, City University of Hong Kong, Shenzhen, 518057, China.

†These authors contributed equally to this work.

*Correspondence author. E-mail: hua.zhang@cityu.edu.hk, kedar@ntu.edu.sg.

This PDF file includes:

Supplementary Figs. 1 to 64

Supplementary Tables 1 to 7

Supplementary Notes 1 to 5

Other Supplementary Materials for this manuscript includes the following:

Supplementary Data 1: The CIF document of 1T'-WS₂ crystal

Supplementary Data 2: The CIF document of 1T'-WSe₂ crystal

Supplementary Data 3: The CIF document of 1T'-MoS₂ crystal

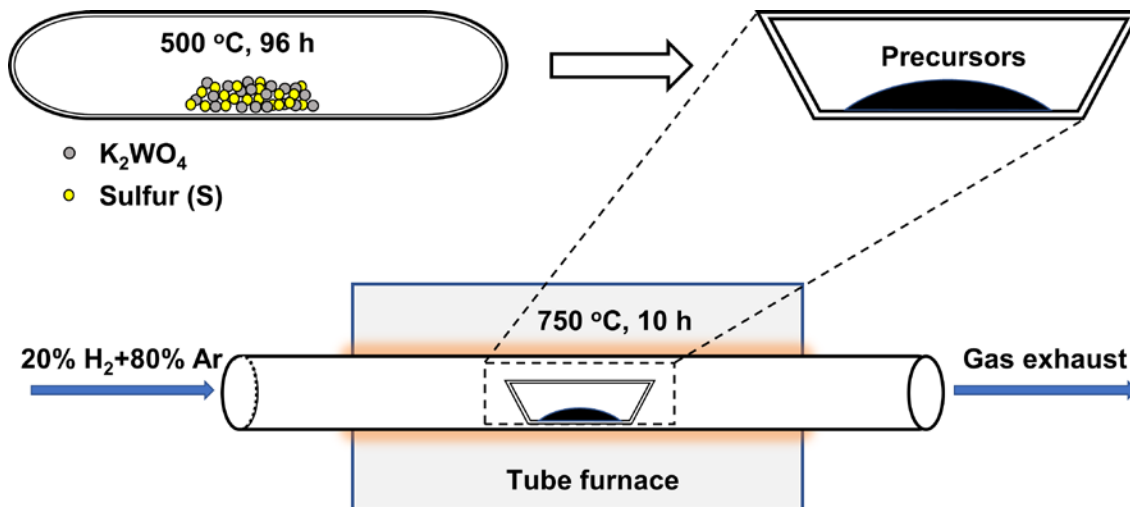
Supplementary Data 4: The CIF document of 1T'-MoSe₂ crystal

Table of Contents

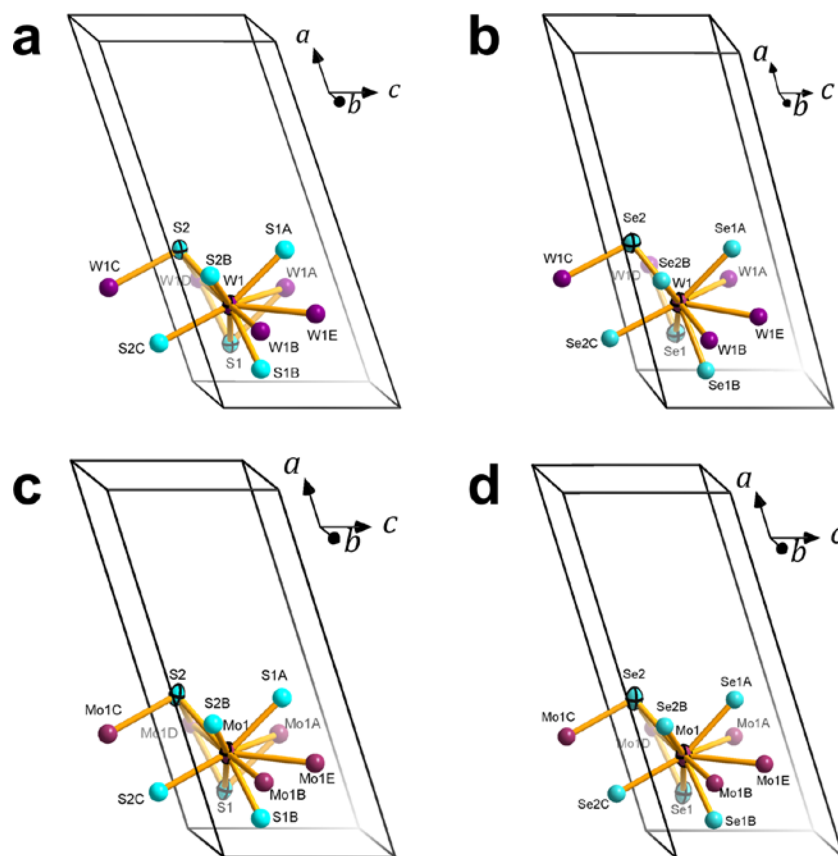
1. Supplementary figures and notes	S5
1.1. 1T'-WS ₂ , 1T'-WSe ₂ , and 1T'-WS _{2x} Se _{2(1-x)}	S5
1.2. 1T'-MoS ₂ , 1T'-MoSe ₂ , and 1T'-MoS _{2x} Se _{2(1-x)}	S41
1.3. Electrical transport and superconducting measurements	S61
1.4. Discussion on the calculation results of 2H-WS ₂ and 1T'-WS ₂	S75
2. Supplementary tables	S77
Supplementary Note 1	S25
Supplementary Note 2	S37
Supplementary Note 3	S41
Supplementary Note 4	S50
Supplementary Note 5	S57
Supplementary References	S85

1. Supplementary figures and notes

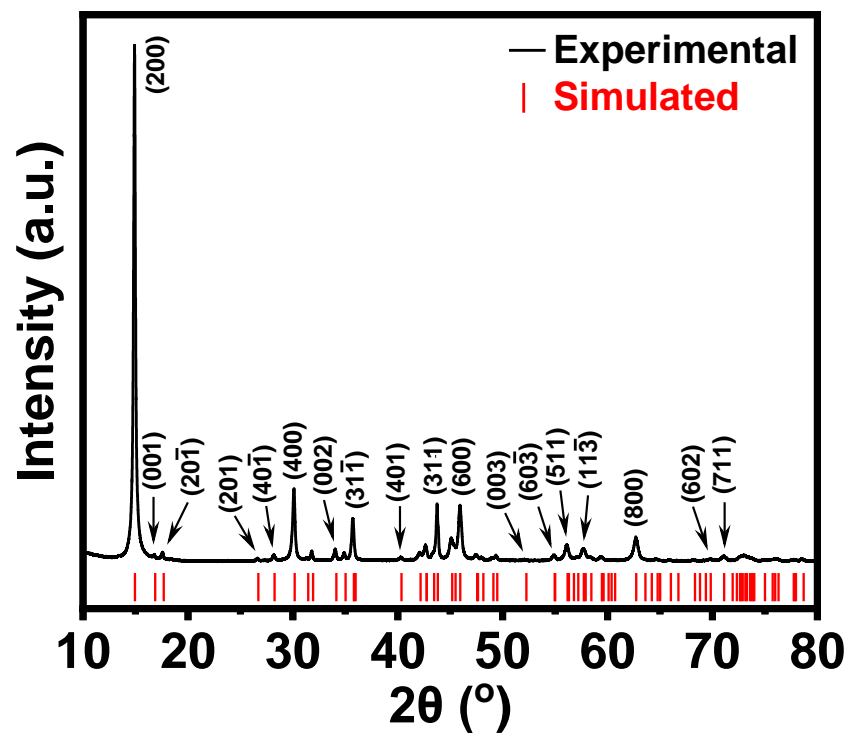
1.1. 1T'-WS₂, 1T'-WSe₂, and 1T'-WS_{2x}Se_{2(1-x)}



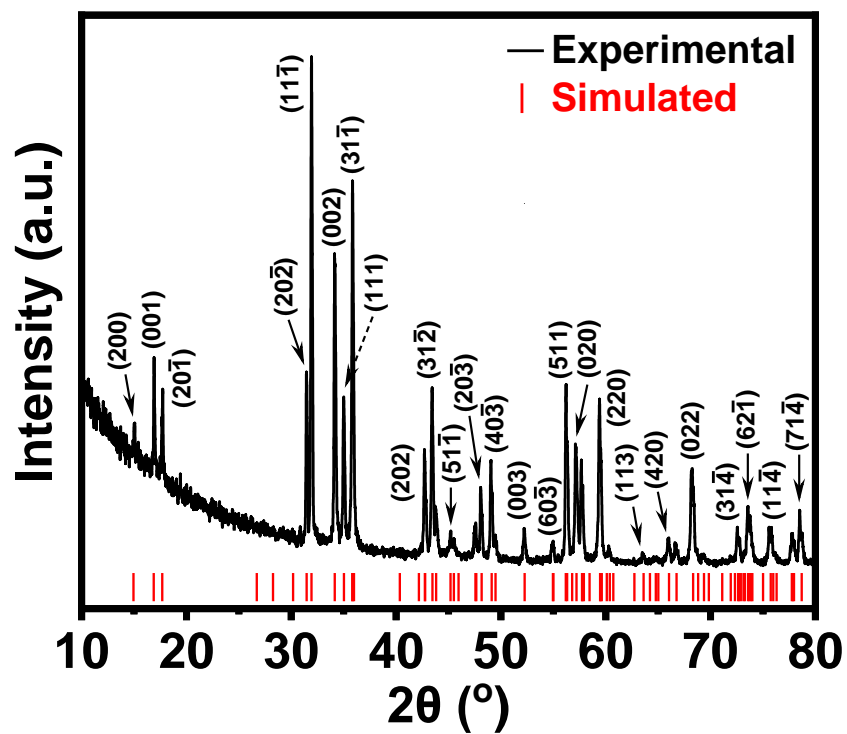
Supplementary Fig. 1 | Schematic illustration for the synthesis of 1T'-WS₂ crystals.



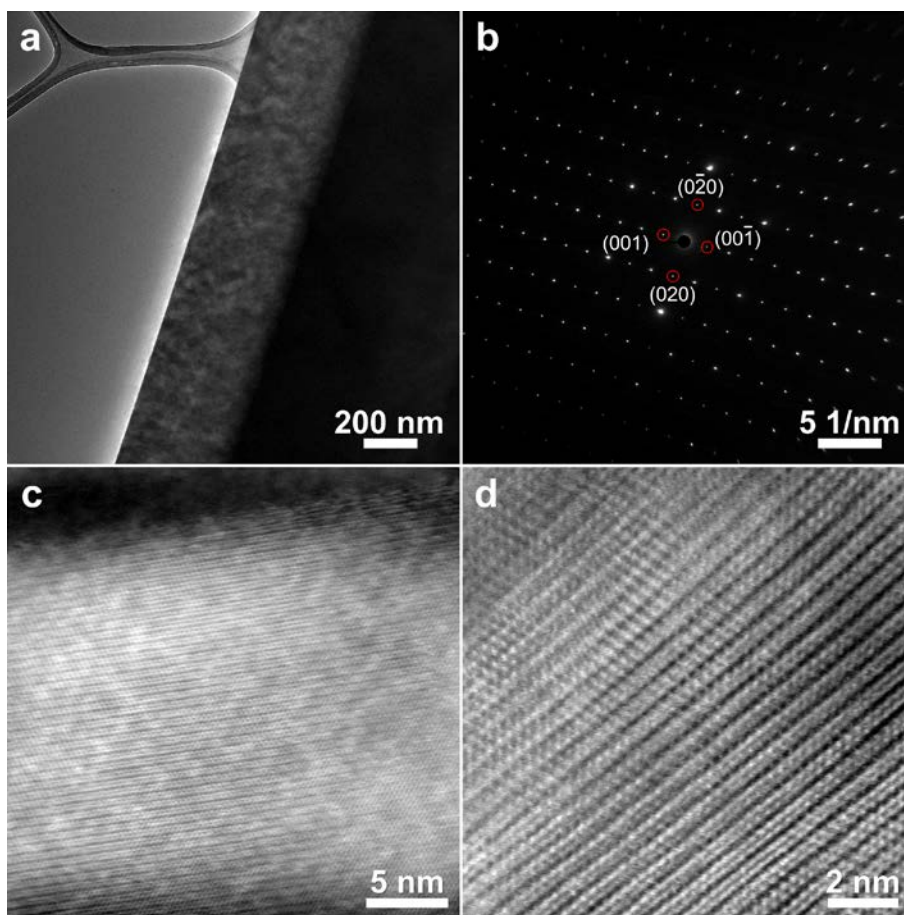
Supplementary Fig. 2 | The coordination environment of (a) 1T'-WS₂, (b) 1T'-WSe₂, (c) 1T'-MoS₂ and (d) 1T'-MoSe₂ (probability ellipsoids drawn at 50% for independent unit). Symmetry code: A = 1/2-x, 1/2-y, 1-z; B = x, 1+y, z; C = 1/2-x, 1/2-y, -z; D = x, -1+y, z; E = 1/2-x, 3/2-y, 1-z. The visual pictures of atoms in unit cells indicate four compounds are isostructural (W and Mo atoms possess the same position, and S and Se atoms also have the same position).



Supplementary Fig. 3 | Comparison of experimental and simulated XRD patterns of the as-prepared 1T'-WS₂ crystals.

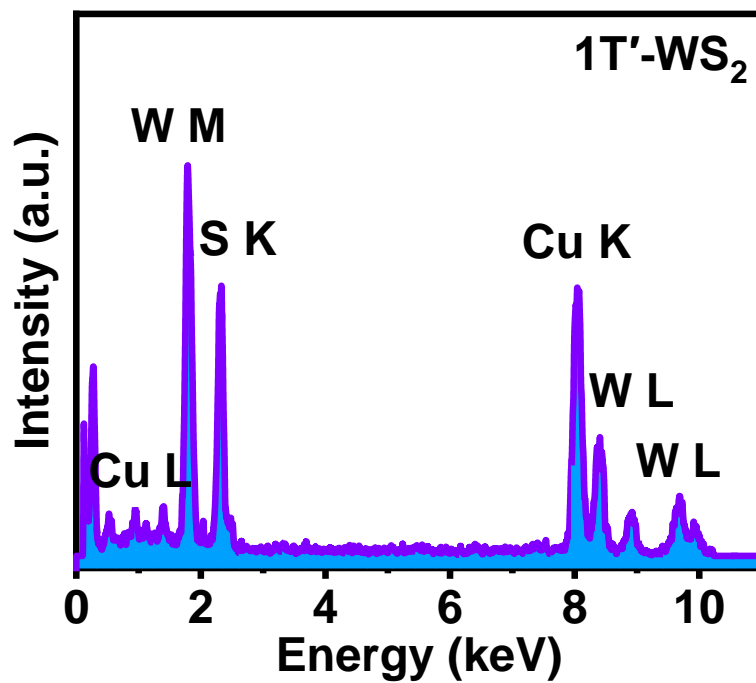


Supplementary Fig. 4 | Comparison of experimental XRD pattern obtained in the transmission mode and simulated XRD pattern of the as-prepared 1T'-WS₂ crystals.



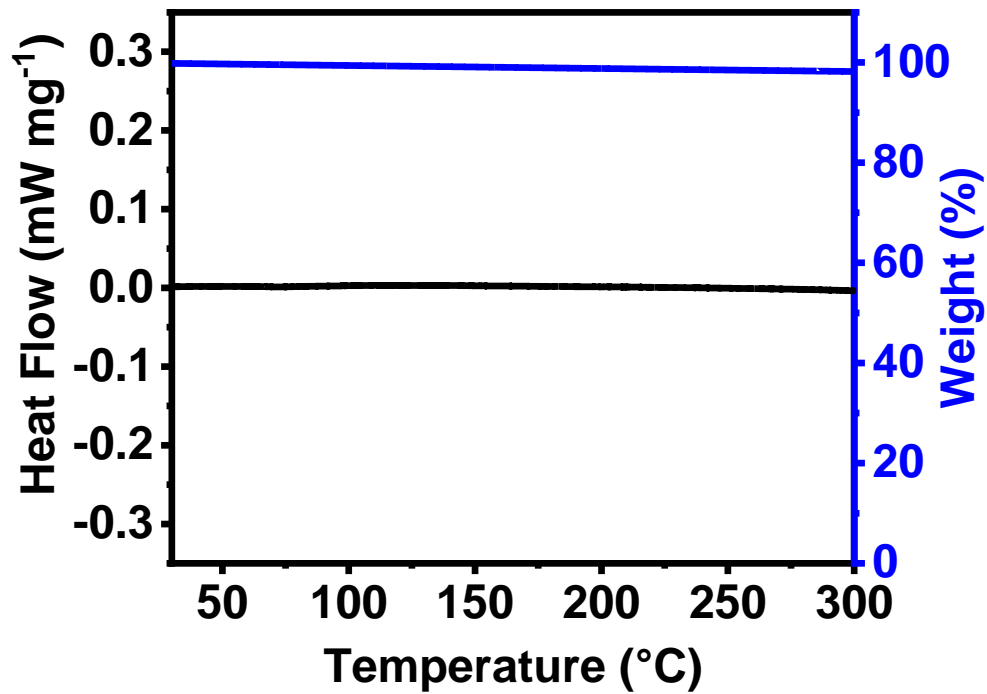
Supplementary Fig. 5 | Structure characterization of 1T'-WS₂. **a**, Low-magnification TEM image obtained from the edge of a 1T'-WS₂ flake. **b**, SAED pattern taken from the 1T'-WS₂ flake in **(a)**. **c,d**, High-resolution HAADF-STEM images taken from the 1T'-WS₂ flake in **(a)**.

To further confirm the 1T' structure of the as-prepared 1T'-WS₂, SAED pattern (**Supplementary Fig. 5b**) and HAADF-STEM images (**Supplementary Fig. 5 c-d**) were taken from the edge of another 1T'-WS₂ flake (**Supplementary Fig. 5a**). Obviously, the SAED pattern shows the same characteristic 1T' structure diffraction as that shown in **Fig. 2a-d**. One-dimensional zigzag chains of W atoms are also observed and repeatedly appeared in both two STEM images, which are consistent with the simulated structure model (**Fig. 2g**), further confirming the high purity of the as-prepared 1T'-WS₂ crystals.

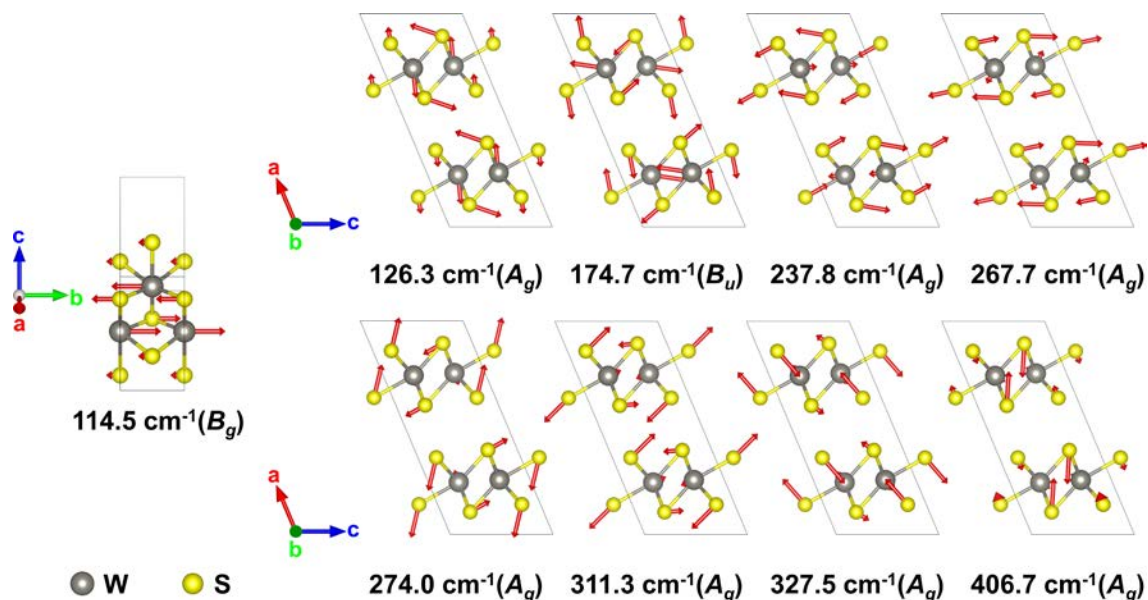


Supplementary Fig. 6 | The EDS spectrum obtained from a 1T'-WS₂ flake under STEM mode.

Note that the Cu signals in the EDS spectrum are from the Cu TEM grid.

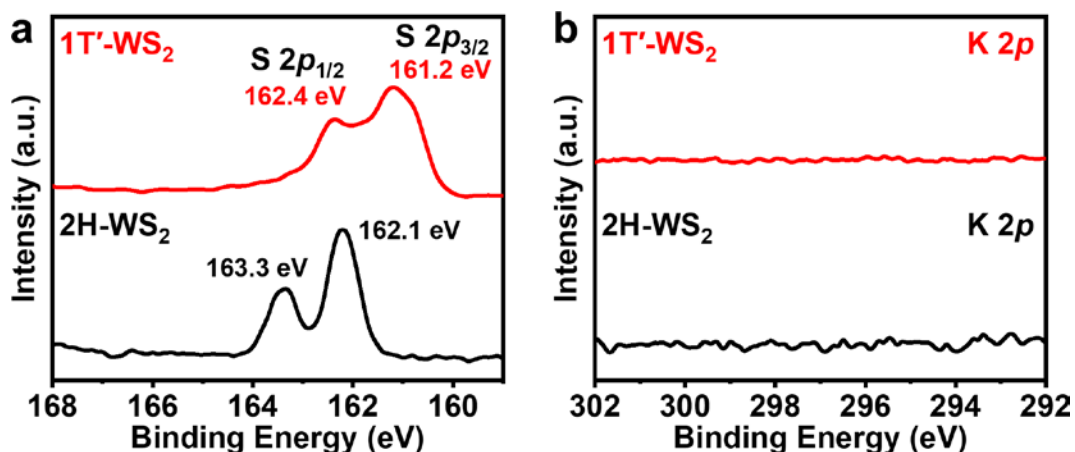


Supplementary Fig. 7 | TGA-DSC curves of 2H-WS₂ obtained by annealing 1T'-WS₂ crystals.



Supplementary Fig. 8 | The vibrational vectors of Raman-active modes of 1T'-WS₂. B_g mode is viewed in the bc-plane, while A_g and B_u modes are viewed in the ac-plane.

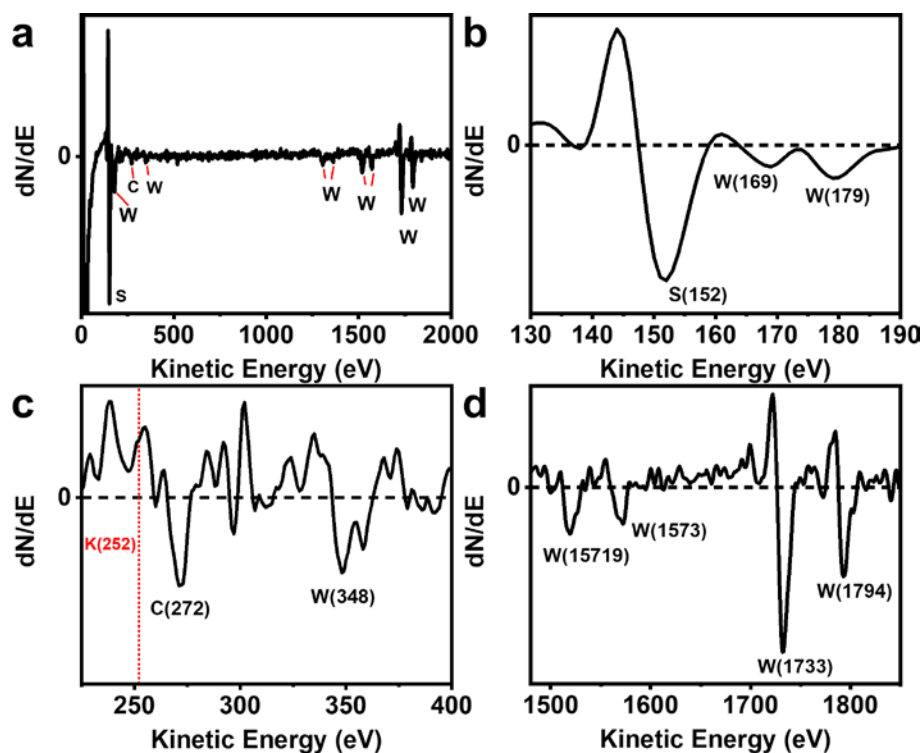
The calculated Raman active modes and their corresponding intensities of 1T'-WS₂ are shown in **Supplementary Fig. 8** and **Table 4**. Compared to 2H-WS₂ which only has two first-order Raman-active modes due to its trigonal prismatic crystal structure, 1T'-WS₂ exhibits more vibrational modes theoretically (**Supplementary Table 4**). The emergence of low-frequency vibrational modes is attributed to the reduction of symmetry of 1T' crystal structure. The most intense Raman signals from the DFT calculations are ascribed to B_g, A_g and B_u modes (**Supplementary Fig. 8**). Nine typical Raman-active vibrational modes (1 B_g + 6 A_g + 2 B_u) are also in good agreement with the experiment (**Fig. 3b**).



Supplementary Fig. 9 | High-resolution XPS spectra of 1T'- and 2H-WS₂ crystals. a, High-resolution XPS S 2p spectra. **b,** High-resolution XPS K 2p spectra.

In the high-resolution K 2p XPS spectra (**Supplementary Fig. 9b**), there is no observable K signal, indicating the absence of potassium in the as-prepared 1T'-WS₂.

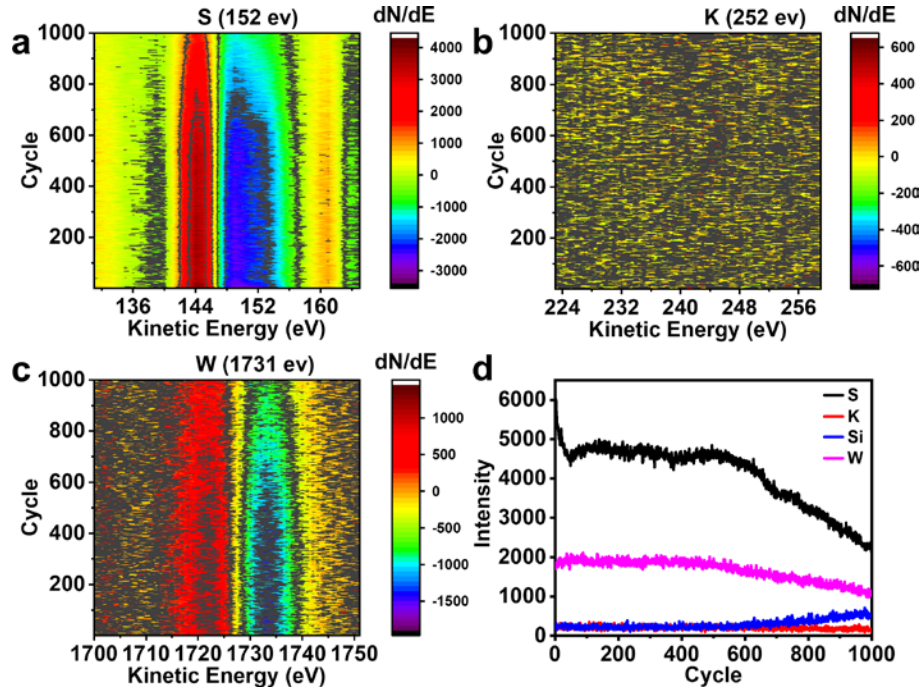
To further confirm the absence of potassium in the as-prepared 1T'-WS₂, the surface-sensitive Auger Electron Spectroscopy (AES) technique was carried out during the pulse-wise ion sputtering on the surface of 1T'-WS₂ crystals. Compared to EDS, AES with lower detection limit can be used to detect any trace-amount elements at uppermost atomic layers exposed after each sputtering cycle¹. Therefore, the depth profile of measured elements can be obtained across the whole sample. As shown in **Supplementary Fig. 10**, the K signal (the negative peak at around 252 eV) cannot be observed in the as-prepared 1T'-WS₂ before the ion sputtering, indicating the absence of K in 1T'-WS₂.



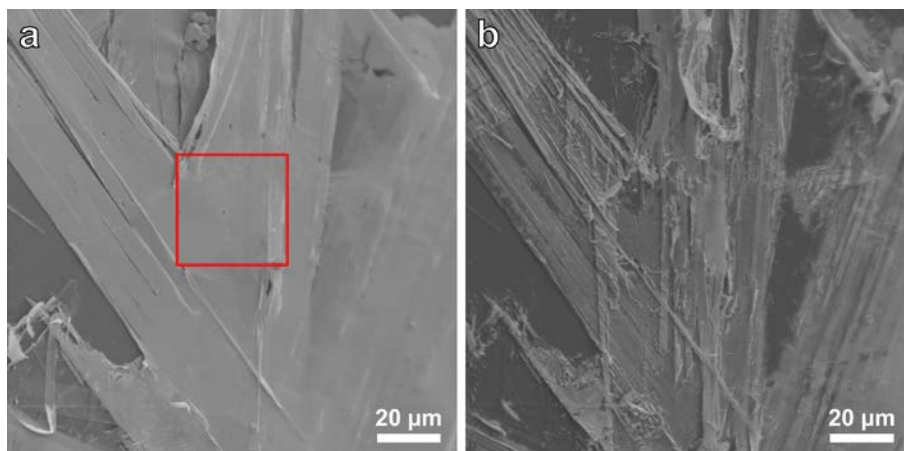
Supplementary Fig. 10 | AES analysis of the as-prepared 1T'-WS₂ crystals. a, Survey AES spectrum in derivative form obtained from the as-prepared 1T'-WS₂ crystals. **b-d**, Magnified AES analyses in (a) showing the negative peak positions of different elements: (b) S, (c) K and (d) W.

Furthermore, we carried out 1,000 cycles of ion sputtering on the 1T'-WS₂ crystal to investigate the compositions in the whole crystal (**Supplementary Fig. 11**). Obviously, as shown in **Supplementary Fig. 11a-c**, during the etching process, no K signals can be detected. The Si signals start to appear in the AES spectrum after ~600 cycles (**Supplementary Fig. 11d**), indicating the exposure of Si substrate after 1T'-WS₂ started to be etched out. This is also confirmed by the SEM image of the sample after 1,000 sputtering cycle (**Supplementary Fig. 12**). In order to further confirm the absence of K in our as-prepared 1T'-WS₂ crystals, AES depth profiling was also performed on three more 1T'-WS₂ crystals. Same as the result obtained in the first 1T'-WS₂ crystal, no K signals

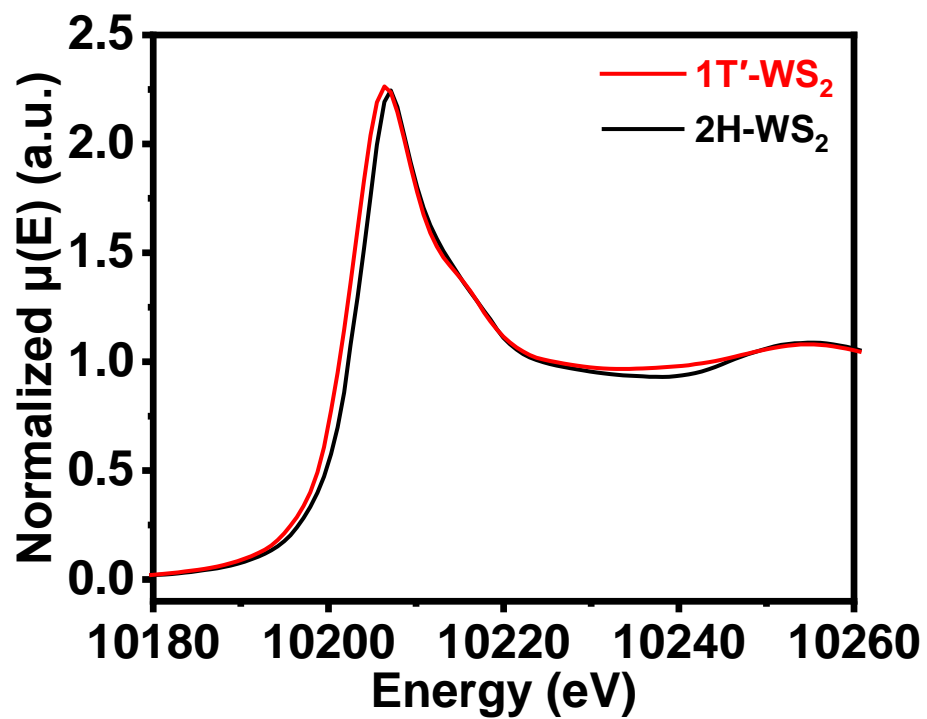
were detected during the whole etching process on the other three 1T'-WS₂ crystals. All the aforementioned results confirm the absence of potassium in our as-prepared 1T'-WS₂ crystals.



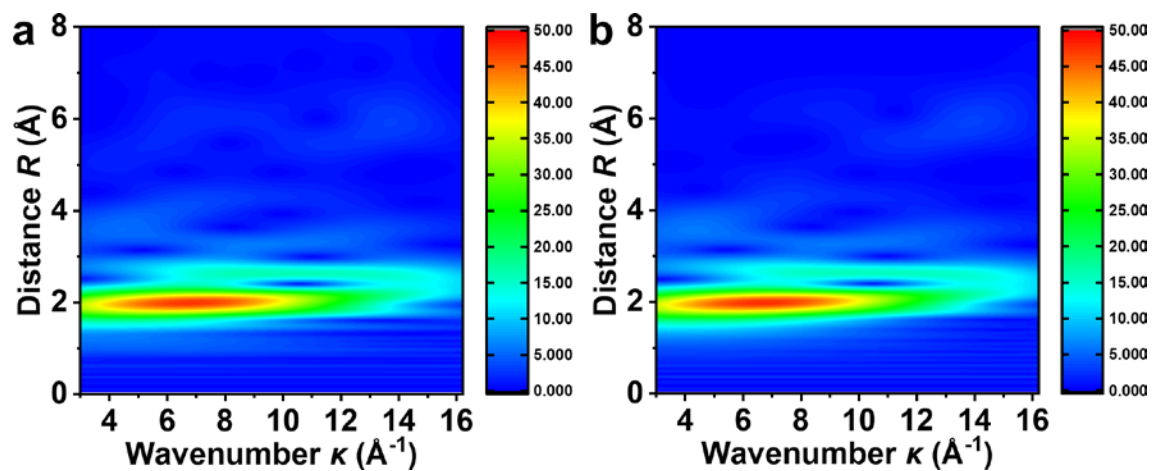
Supplementary Fig. 11 | Depth-profiling AES analysis of the as-prepared 1T'-WS₂ crystals in 1,000 sputtering cycles. a-c, High-resolution AES spectra in narrow scan ranges of (a) S, (b) K and (c) W signals, respectively, over 1000 sputtering cycles. **d,** Peak-to-peak signals of different elements measured in dN/dE curves versus the sputtering cycle.



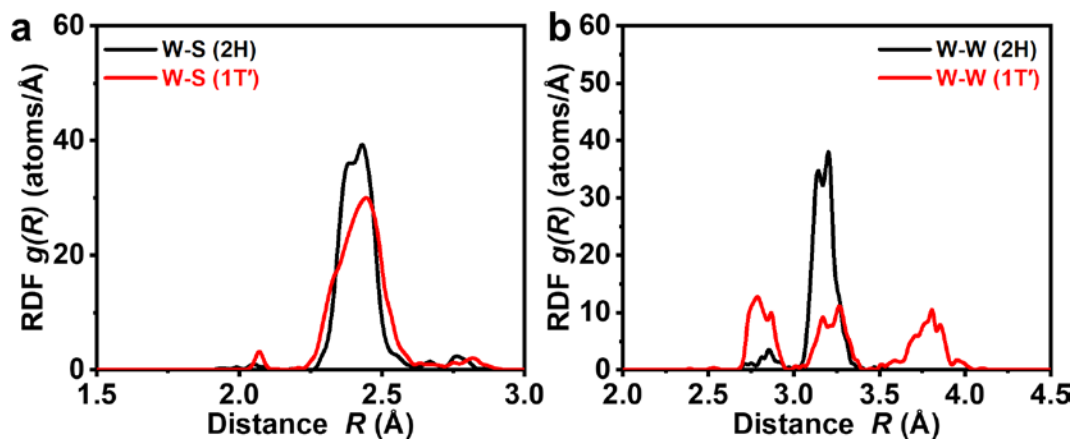
Supplementary Fig. 12 | SEM images of the as-prepared 1T'-WS₂ sample **(a)** before and **(b)** after 1,000 sputtering cycles. The AES scanned area is marked by the red square.



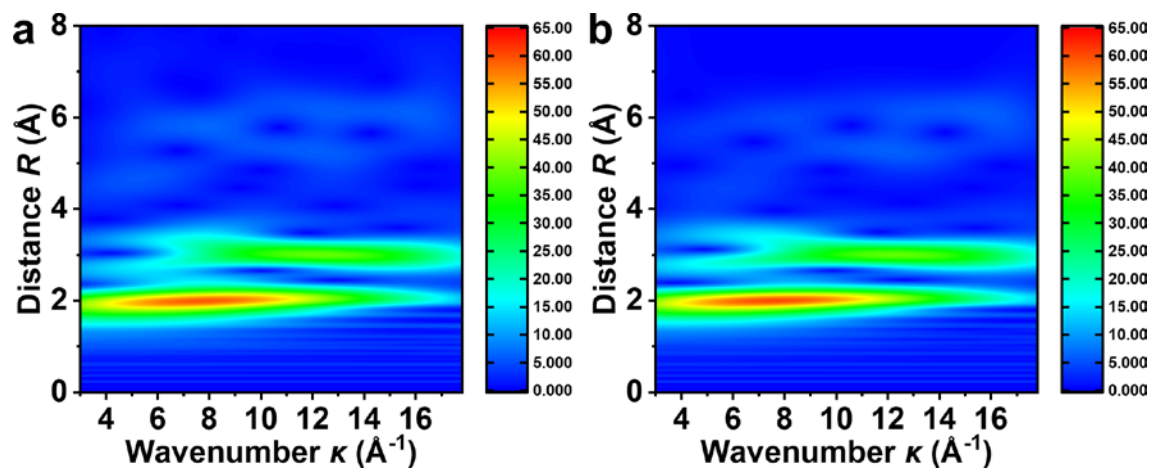
Supplementary Fig. 13 | Normalized W L₃-edge XANES spectra of the as-prepared 1T'-WS₂ and 2H-WS₂.



Supplementary Fig. 14 | (a) Experimental and (b) fitted wavelet transforms of W L₃-edge EXAFS spectra of the as-prepared 1T'-WS₂ based on evolutionary algorithm.



Supplementary Fig. 15 | Radial distribution functions (RDFs) of the adjacent (a) W-S and (b) W-W coordinations of the as-prepared 1T'-WS₂ and 2H-WS₂.

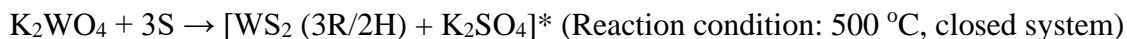


Supplementary Fig. 16 | (a) Experimental and (b) fitted wavelet transforms of W L_3 -edge EXAFS spectra of 2H-WS₂ based on evolutionary algorithm.

Possible reaction mechanism for the synthesis of 1T'-WS₂ (Supplementary Fig. 17-18)

To investigate the possible formation mechanism of 1T'-WS₂ using our current closed-system (*cs*) gas-solid method, EDS and XRD were carried out to characterize the precursor, referred to as *cs*-WS₂-precursor, obtained during the synthesis of 1T'-WS₂. As shown in **Supplementary Fig. 17a**, the XRD pattern of the precursor obtained during the preparation of 1T'-WS₂ can be indexed to 2H/3R-WS₂ (see the peaks indicated by arrows in **Supplementary Fig. 17a**), which is similar to the result reported by Toh et al.², and K₂SO₄. The EDS results (taken on more than 10 areas) showed the signals of W, K, S and O with the atomic ratio close to 1:2:3:5 (**Supplementary Fig. 17b**). Note that additional O signal may arise from the conductive carbon tape and the SEM characterization system. Therefore, we can speculate that the precursor is possibly [2H/3R-WS₂+K₂SO₄]*.

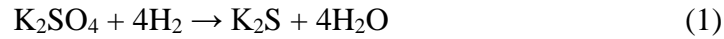
Therefore, the reaction in the sealed quartz ampoule using our current closed-system gas-solid method could be proposed below.



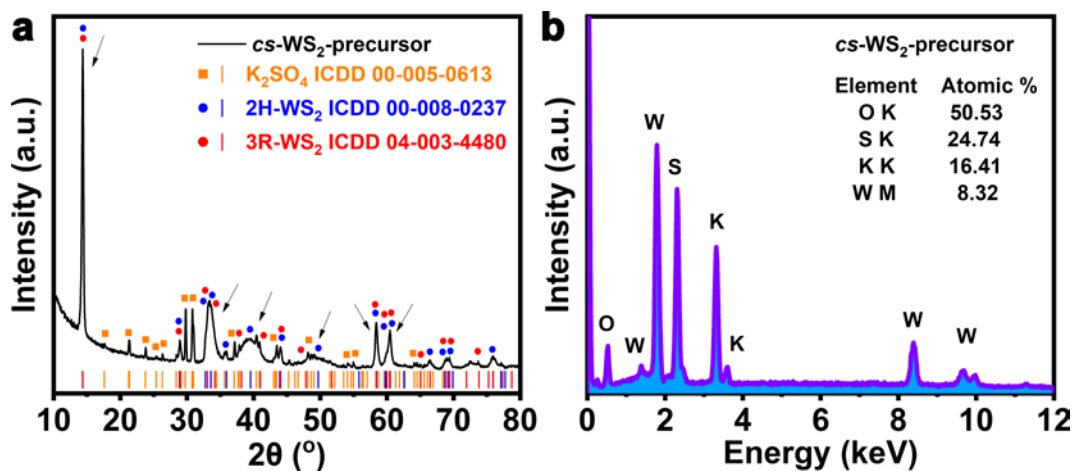
The possible mechanism for the formation of 1T'-WS₂ crystal is proposed and described as follows.

First, K₂SO₄ could quickly undergo the reduction reaction to form K₂S and H₂O at 750 °C in the H₂ gas environment (Reaction 1), as reported by C. W. So and D. Barham³. Second, WS₂ in the precursor could react with H₂ and H₂O produced in Reaction 1 to form tungsten oxides or tungsten hydroxides²⁰. One possible reaction in the oxidation of WS₂ is shown in Reaction 2, which follows the proposed mechanism reported by Sahoo et al.⁴. One of the products, H₂S, was successfully detected in the exhaust gas during the synthesis

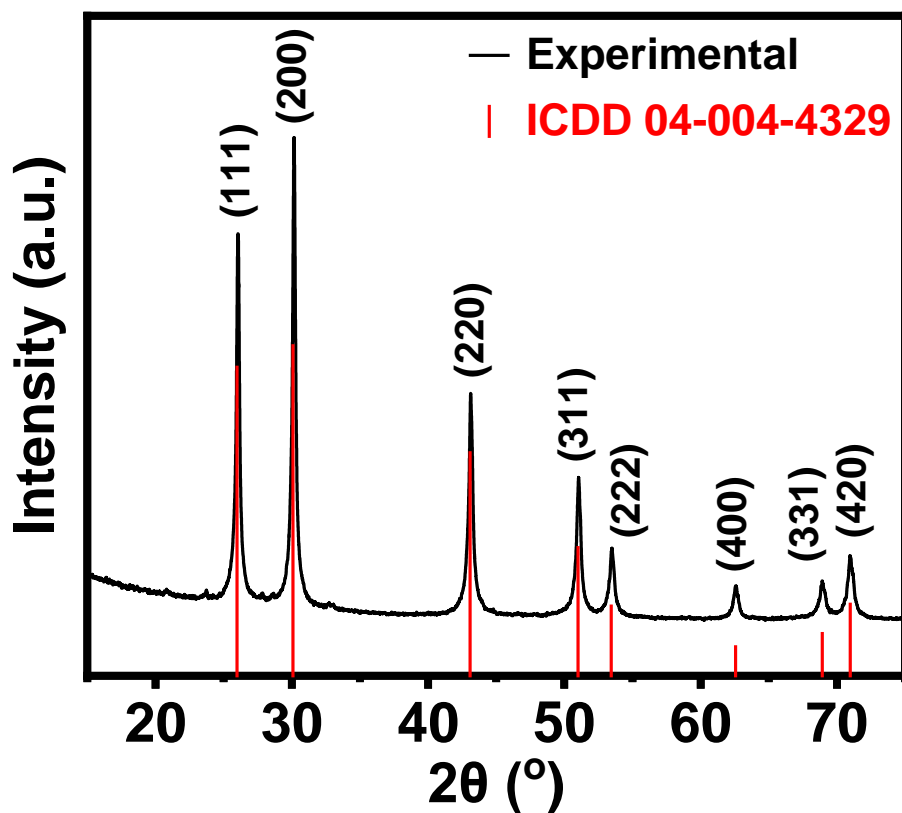
after reaction with the $\text{Pb}(\text{CH}_3\text{COO})_2$ solution (see **Supplementary Fig. 18**). The formation of PbS black precipitates confirms the presence of H_2S , and this result recognizes the possibility of oxidation of WS_2 in the H_2O steam. Finally, the tungsten oxides could react with K_2S (obtained in Reaction 1) and H_2S gas (obtained in Reaction 2) to form K_yWS_2 (Reaction 3). The reaction of H_2S with tungsten oxides has been reported by Sahoo et al.⁴. However, instead of formation of pure 2H- WS_2 in the previous work⁴, K_yWS_2 was obtained in our different synthesis due to the presence of K_2S . After K_yWS_2 was washed with Milli-Q water and I_2 acetonitrile solution to completely remove potassium, the final product of 1T'- WS_2 , was obtained. This result is similar to the preparation of 1T'- MoS_2 by removal of potassium from K_xMoS_2 synthesized by the chemical vapor deposition method in reductive gas (a mixture of H_2 and Ar)⁵.



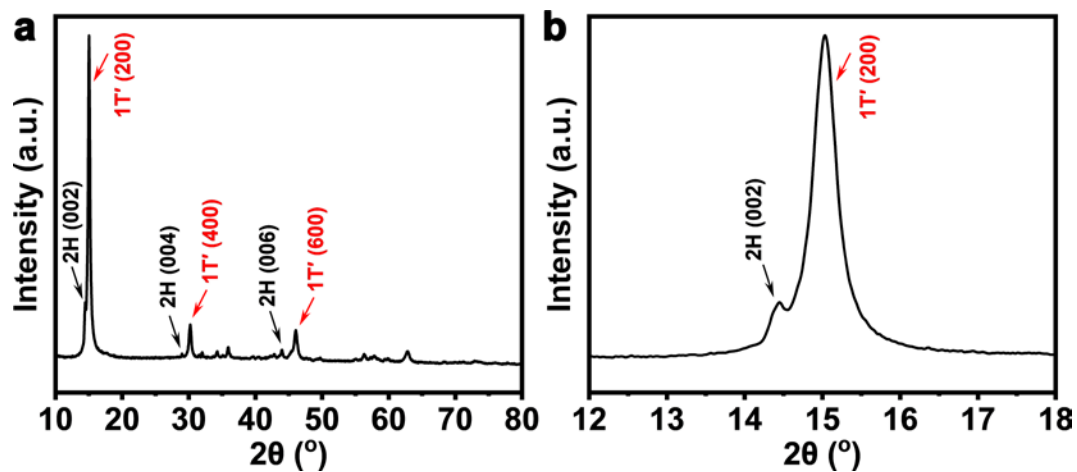
To further confirm the proposed possible mechanism, a control experiment was conducted by using the mixed powders of commercial 2H- WS_2 and K_2SO_4 with the molar ratio of 1:1 to replace the precursor obtained by the reaction of K_2WO_4 with S in sealed ampoule. As shown in **Supplementary Fig. 19**, the XRD pattern confirms the obtained WS_2 with mixed 1T' and 2H phases (see the peaks indicated by arrows in **Supplementary Fig. 19**). Although the result could partially support our proposed mechanism, more studies will be carried out in the future to fully understand the mechanism on the formation of 1T'- WS_2 by using our method.



Supplementary Fig. 17 | (a) XRD pattern and (b) EDS spectrum of *cs*-WS₂-precursor obtained by our closed-system gas-solid method.



Supplementary Fig. 18 | XRD pattern of the PbS obtained by flowing the exhaust gas during the synthesis of 1T'-WS₂ crystals into the Pb(CH₃COO)₂ solution, indicating the presence of H₂S in the exhaust gas.

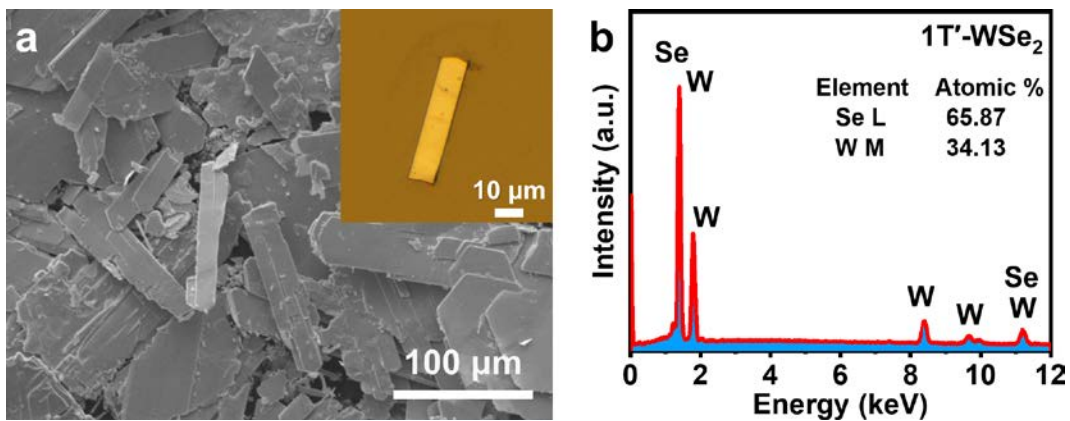


Supplementary Fig. 19 | XRD characterization of WS₂ obtained by using the mixture of commercial 2H-WS₂ and K₂SO₄. **a**, XRD patterns of WS₂ obtained using the mixture of commercial 2H-WS₂ and K₂SO₄, showing the mixed 1T' and 2H phases. **b**, Magnified XRD patterns of the (200) and (002) peaks of 1T' and 2H phases, respectively, in (a).

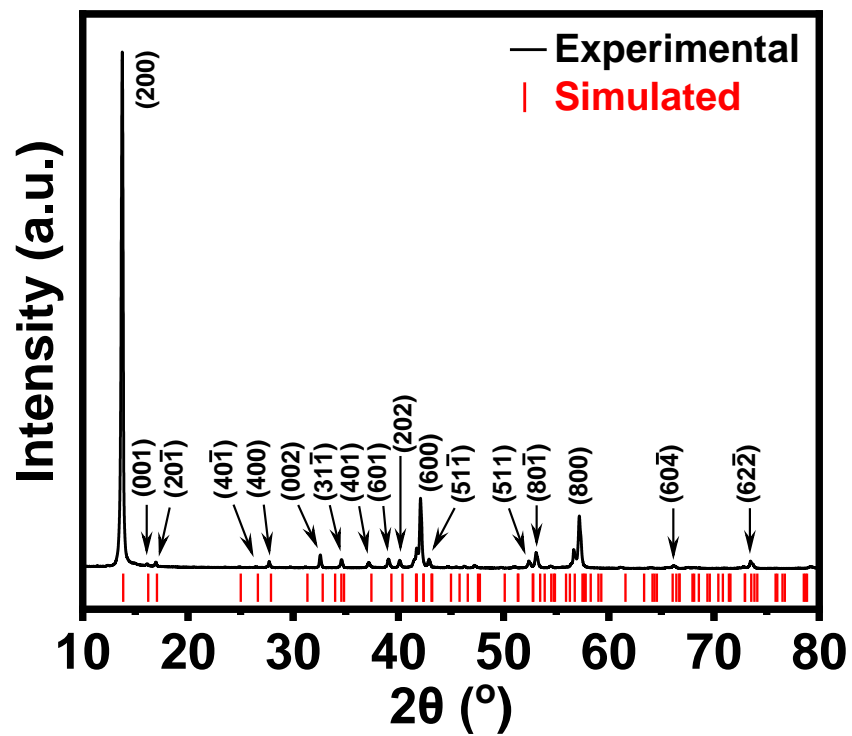
Supplementary Note 1

Besides 1T'-WS₂, 1T'-WSe₂ was also successfully synthesized and fully characterized. As shown in **Supplementary Fig. 20a**, the as-prepared 1T'-WSe₂ crystals exhibit similar morphology to 1T'-WS₂ (**Fig. 1a**). The EDS spectrum exhibits strong signals of W and Se with the atomic ratio of ~1:2 (**Supplementary Fig. 20b**), which is consistent with the stoichiometry of WSe₂. As shown in **Supplementary Tables 1-3** and **Supplementary Fig. 2b**, our as-prepared 1T'-WSe₂ crystallizes in a monoclinic symmetry with the space group of *C2/m* (space group number 12; $a = 13.739(4)$ Å, $b = 3.2651(8)$ Å, $c = 5.865(1)$ Å, $\beta = 111.505(7)^\circ$ and $V = 244.77(11)$ Å³). The powder XRD pattern of our as-prepared 1T'-WSe₂ also matches the simulated XRD pattern well based on the crystal data (**Supplementary Fig. 21**), confirming the pure phase of our as-prepared 1T'-WSe₂. Furthermore, powder XRD characterization was performed on 2H-WSe₂ crystals obtained by thermal annealing (**Supplementary Fig. 22**). Notably, a shift of the (200) peak to higher degree on our as-prepared 1T'-WSe₂ was also observed as compared to the (002) peak of 2H-WSe₂. To further confirm the crystal structure of as-prepared 1T'-WSe₂, SAED, high-resolution TEM (HRTEM) and HAADF-STEM characterizations were carried out. As shown in **Supplementary Fig. 23a-b**, the SAED pattern of a typical 1T'-WSe₂ flake exhibits similar distorted octahedral coordinated structure as that of 1T'-WS₂. The clear zigzag chain structure was also observed in the HRTEM (**Supplementary Fig. 23c**) and HAADF-STEM (**Supplementary Fig. 23e**) images, which are consistent with the corresponding FFT patterns in **Supplementary Fig. 23d** and **f**, respectively. Furthermore, the elemental maps (**Supplementary Fig. 24**) and EDS spectrum (**Supplementary Fig. 25**) of 1T'-WSe₂ crystals were obtained under STEM mode, showing strong W and Se

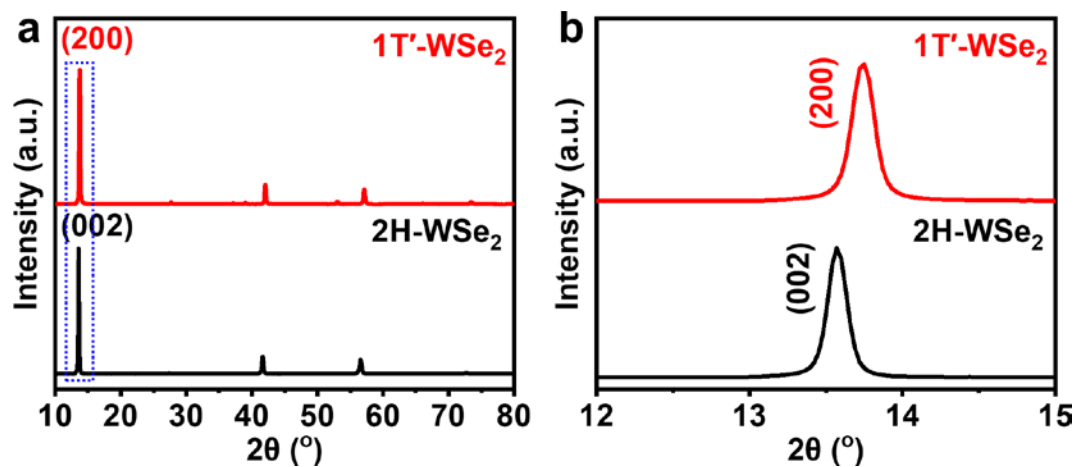
signals. Moreover, as shown in **Supplementary Fig. 26**, Raman spectrum of 1T'-WSe₂ crystals shows distinctive characteristic peaks (105.9, 145.6, 152.7, 177.1, 182.7, 217.9, 236.6 and 259.2 cm⁻¹), which are completely different from those of 2H-WSe₂ (248.3 and 257.6 cm⁻¹)⁶. The peaks located at 105.9, 152.7, 177.1, 217.9, 236.6 and 259.2 cm⁻¹ are similar with the reported results of 1T'-WSe₂ nanoflowers⁷. In addition, DFT calculations based on the solved crystal structure are performed to investigate the Raman vibrational modes of 1T'-WSe₂ (**Supplementary Fig. 27** and **Table 6**). The high-resolution XPS W 4f spectrum of 1T'-WSe₂ also shows ~0.9 eV shift to lower binding energy as compared with the 2H-WSe₂ (**Supplementary Fig. 28**), which is similar to 1T'-WS₂ (**Fig. 3c**). In addition, the thermostability of 1T'- and 2H-WSe₂ crystals was revealed by the TGA and DSC characterizations. As shown in **Supplementary Fig. 29a**, the exothermic heat flow starts at ~160.1 °C, in which the phase transition of 1T'-WSe₂ initiates, and reaches the peak at ~256.2 °C. After thermal annealing of our 1T'-WSe₂, in the TGA-DSC curves of the obtained 2H-WSe₂, neither exothermic peak nor obvious weight loss was observed, indicating the thermodynamically stable nature of 2H-WSe₂ (**Supplementary Fig. 29b**).



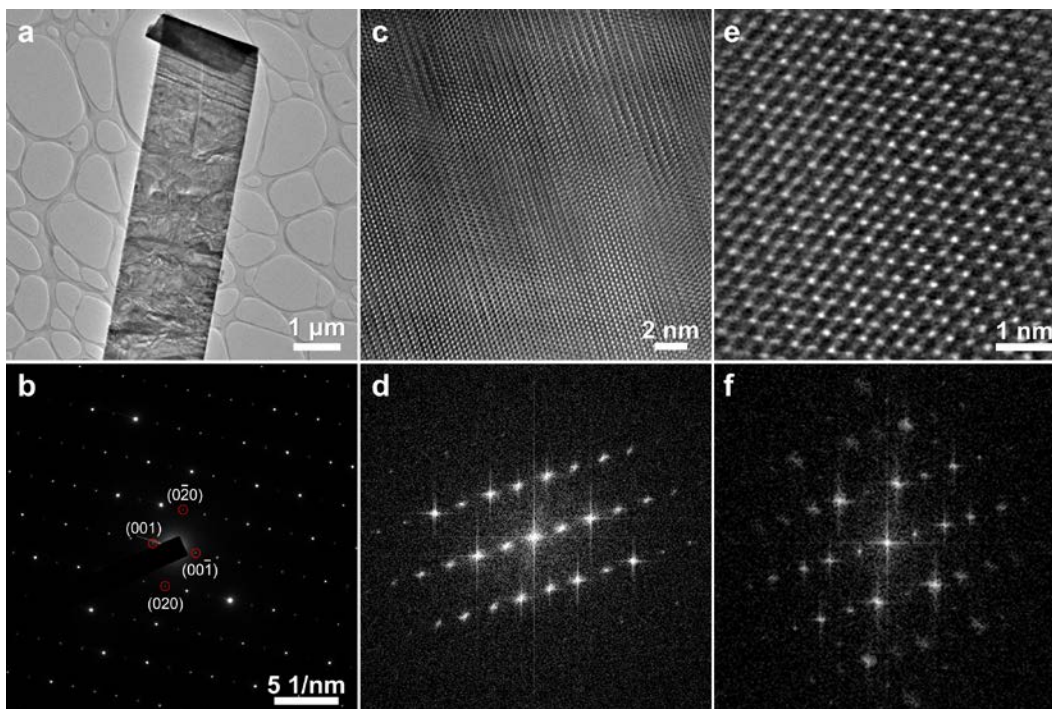
Supplementary Fig. 20 | Morphology and composition analysis of 1T'-WSe₂ crystals. a, SEM image of the as-prepared 1T'-WSe₂ crystals. Inset: optical image of a 1T'-WSe₂ crystal. **b**, EDS spectrum of the as-prepared 1T'-WSe₂ crystals.



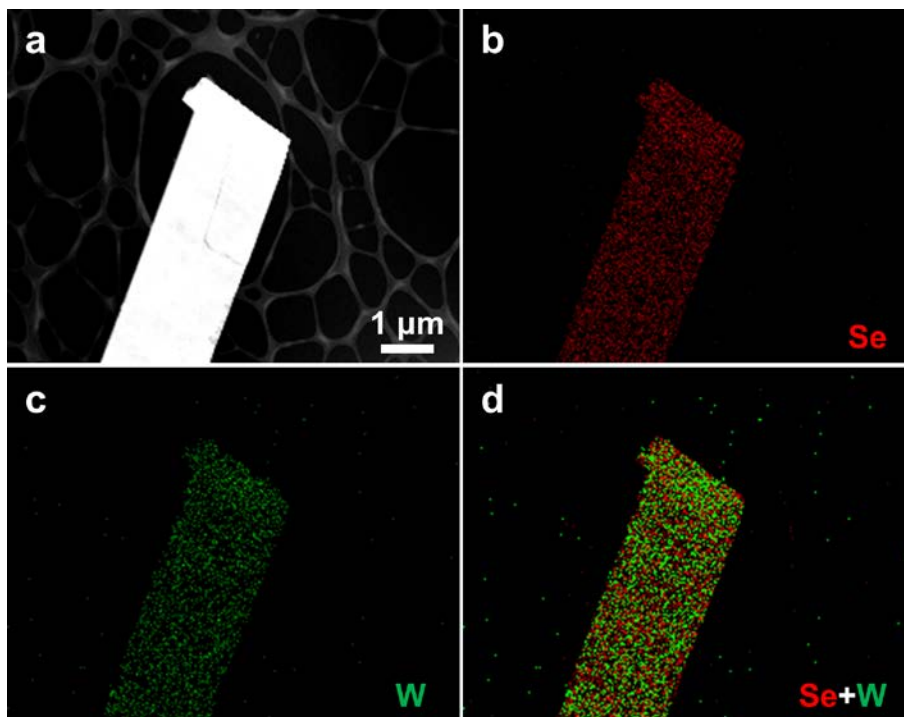
Supplementary Fig. 21 | Comparison of experimental and simulated XRD patterns of the as-prepared 1T'-WSe₂.



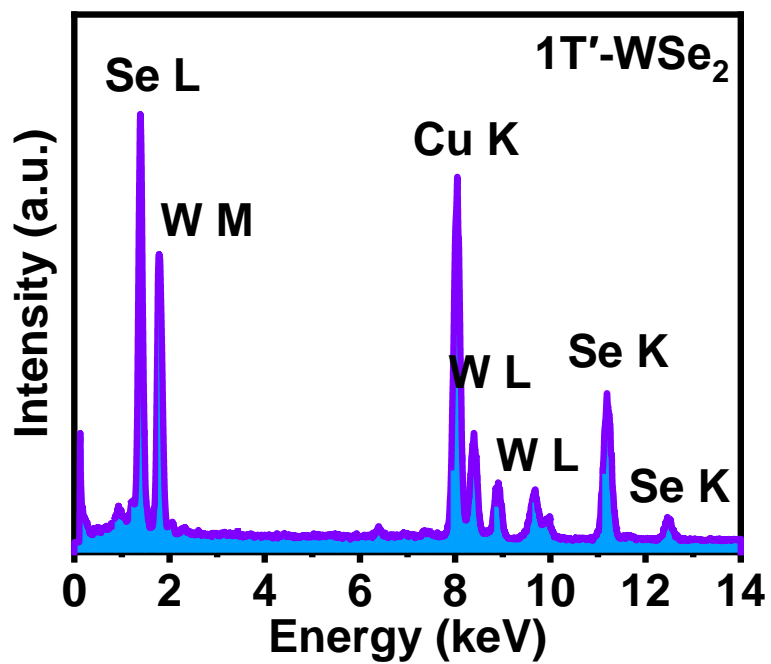
Supplementary Fig. 22 | Structure characterization of 1T'- and 2H-WSe₂. **a**, XRD patterns of 1T'- and 2H-WSe₂ crystals. **b**, Magnified XRD patterns of the (200) peak of 1T'-WSe₂ and (002) peak of 2H-WSe₂ crystals, obtained from the blue dotted area in (a).



Supplementary Fig. 23 | Structure characterization of 1T'-WSe₂ crystals. **a**, Low-magnification TEM image of a 1T'-WSe₂ flake. **b**, SAED pattern taken from the 1T'-WSe₂ flake in **(a)**. **c**, HRTEM image taken on a thin edge of the 1T'-WSe₂ flake in **(a)**. **d**, Corresponding FFT pattern obtained from the HRTEM image in **(c)**. **e**, HAADF-STEM image taken on the thin edge of the 1T'-WSe₂ flake in **(a)**. **f**, Corresponding FFT pattern obtained from the STEM image in **(e)**.

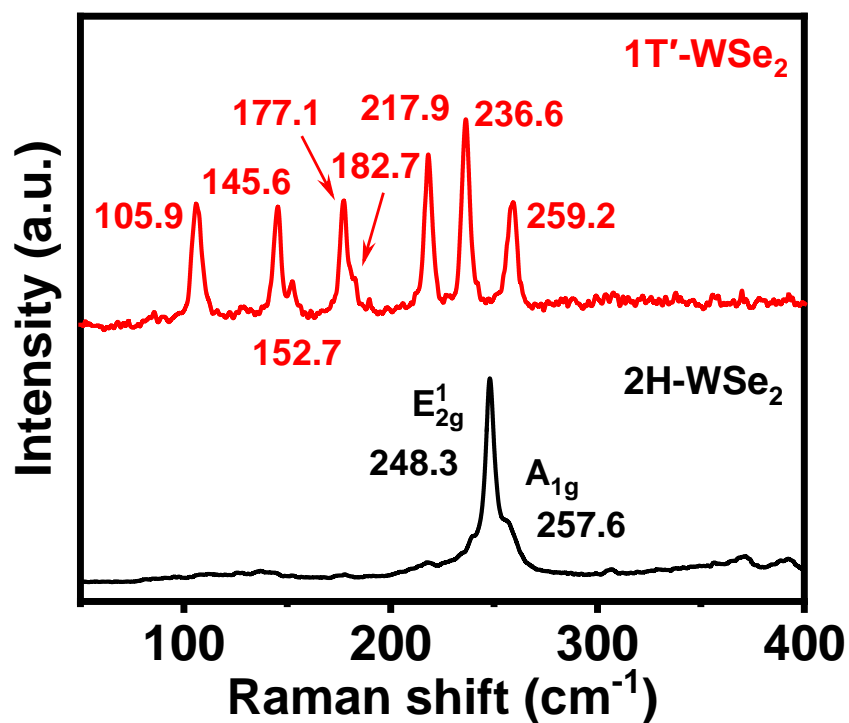


Supplementary Fig. 24 | Elemental mapping of a 1T'-WSe₂ flake. **a**, Dark-field STEM image of a 1T'-WSe₂ flake. **c-d**, Elemental mapping images of the 1T'-WSe₂ flake in **(a)**: **(b)** Se K signals, **(c)** W L signals, and **(d)** the overlap of Se K and W L signals.



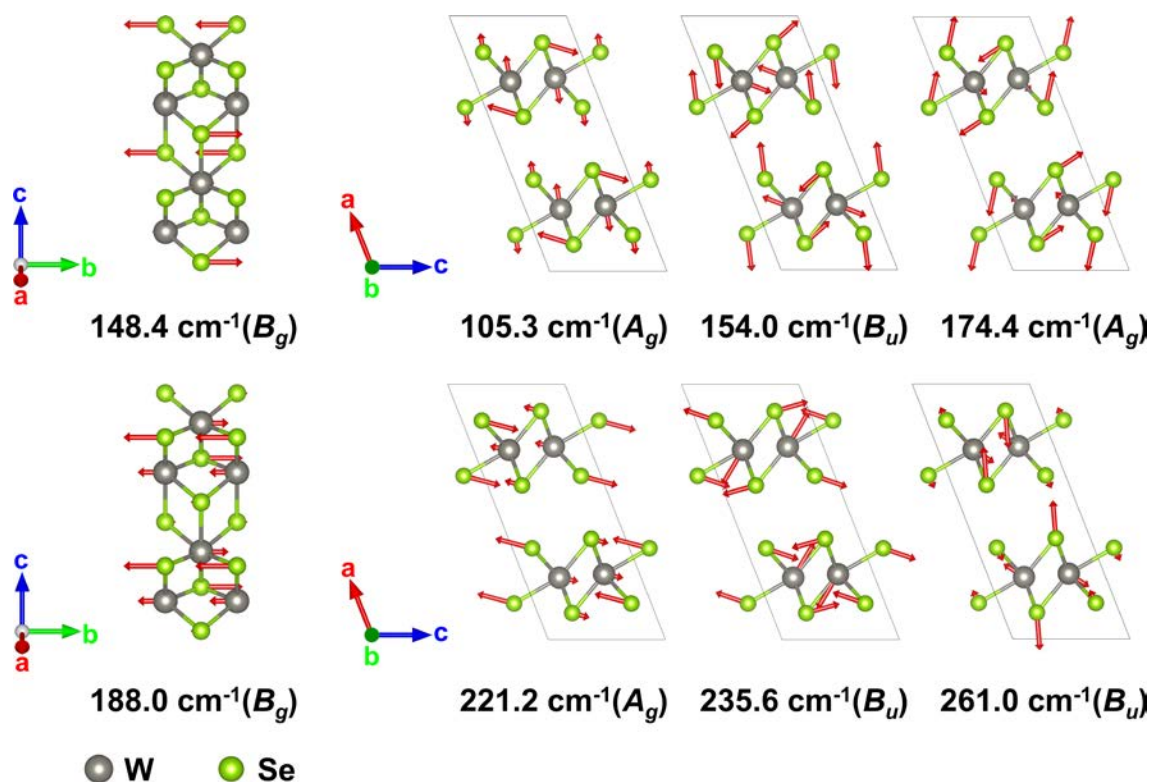
Supplementary Fig. 25 | EDS spectrum obtained from a 1T'-WSe₂ flake under STEM mode.

Note that the Cu signals in the EDS spectrum are from the Cu TEM grid.



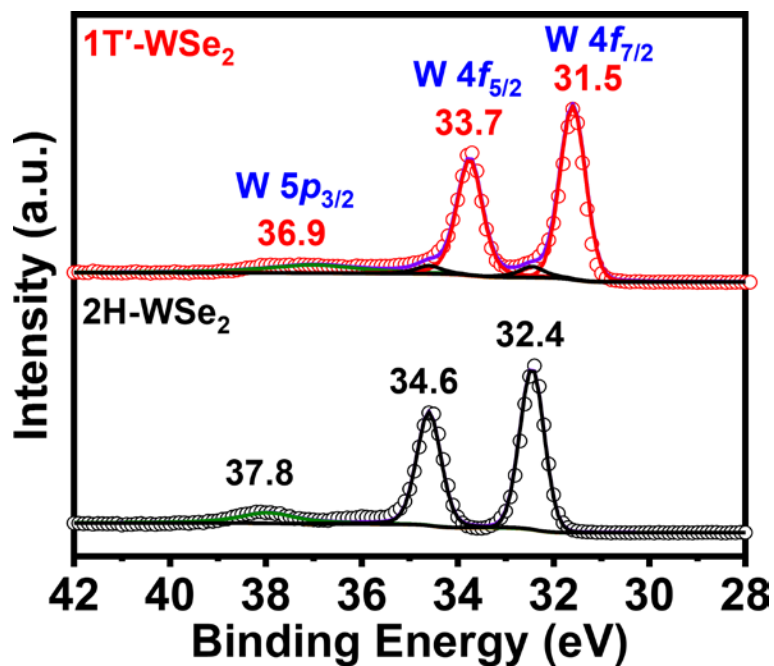
Supplementary Fig. 26 | Raman spectra of 1T'- and 2H-WSe₂ crystals.

As shown in **Supplementary Fig. 26**, the Raman spectrum of the as-prepared 1T'-WSe₂ exhibits eight peaks located at 105.9, 145.6, 152.7, 177.1, 182.7, 217.9, 236.6 and 259.2 cm⁻¹, respectively. Among them, the peaks located at 105.9, 152.7, 177.1, 217.9, 236.6 and 259.2 cm⁻¹ are similar with the previously reported result⁷. However, the E_{2g}¹ (248.3 cm⁻¹) and A_{1g} (257.6 cm⁻¹) peaks belonging to the 2H phase are absent in the Raman spectrum of our as-prepared 1T'-WSe₂ due to the high purity of the 1T' phase. In addition, there are more Raman peaks of 1T'-WSe₂ compared to that of 2H-WSe₂, which could be ascribed to the lower symmetry of the monoclinic 1T' phase compared to the hexagonal 2H phase.

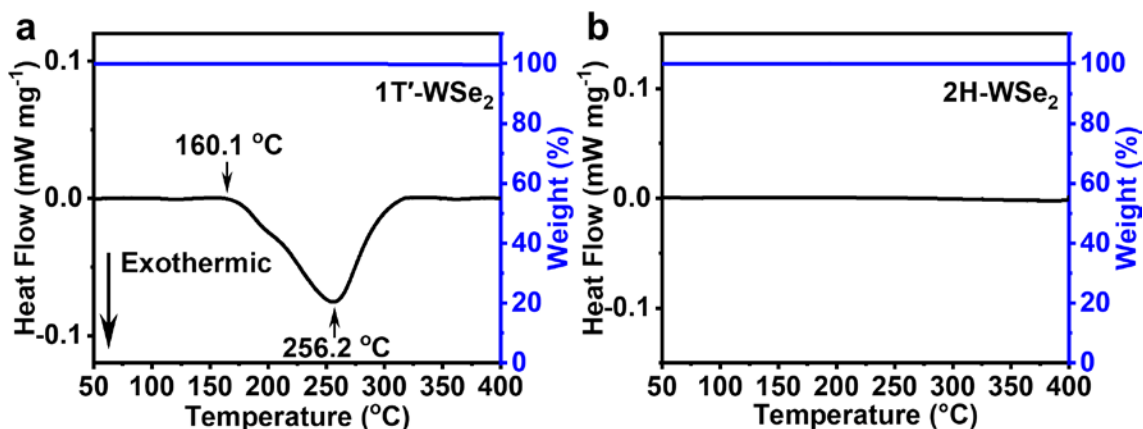


Supplementary Fig. 27 | The vibrational vectors of Raman-active modes of 1T'-WSe₂. B_g mode is viewed in the bc -plane, while A_g and B_u modes are viewed in the ac -plane.

The calculated Raman active modes and their corresponding intensities of 1T'-WSe₂ are shown in **Supplementary Fig. 27** and **Table 6**. Similar to 1T'-WS₂ (**Supplementary Fig. 8** and **Table 4**), 1T'-WSe₂ also exhibits more vibrational modes theoretically compared to 2H-WSe₂. Eight most intense Raman modes ($2 B_g + 3 A_g + 3 B_u$) for 1T'-WSe₂ and their corresponding vibrational vectors are demonstrated in **Supplementary Fig. 27** and **Table 6**, which are consistent with the Raman peaks observed in the experiment (**Supplementary Fig. 26**).



Supplementary Fig. 28 | Experimental (dots) and fitting (curves) high-resolution W 4f XPS spectra of 1T'- and 2H-WSe₂ crystals. The red and black deconvoluted peaks of W 4f belong to the 1T' and 2H phases, respectively.

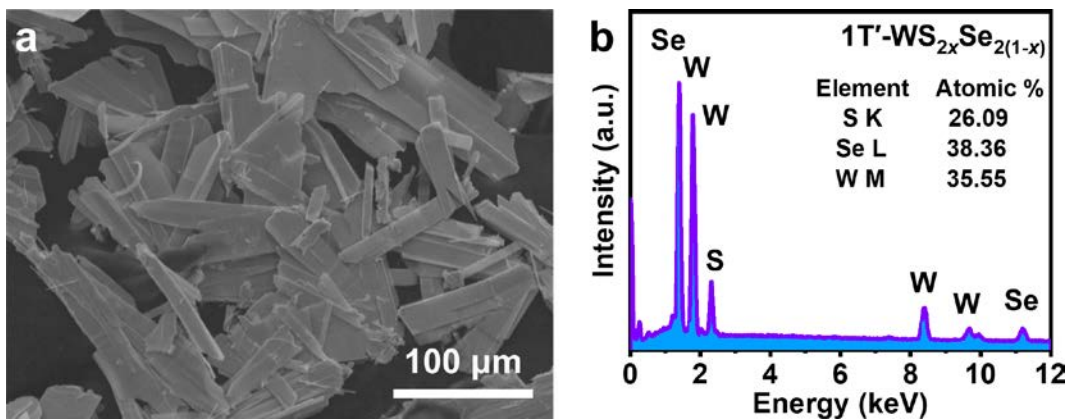


Supplementary Fig. 29 | Thermostability measurement of 1T'- and 2H-WSe₂ crystals. a, TGA-DSC curves of 1T'-WSe₂ crystals. **b,** TGA-DSC curves of 2H-WSe₂ crystals obtained by annealing 1T'-WSe₂ crystals.

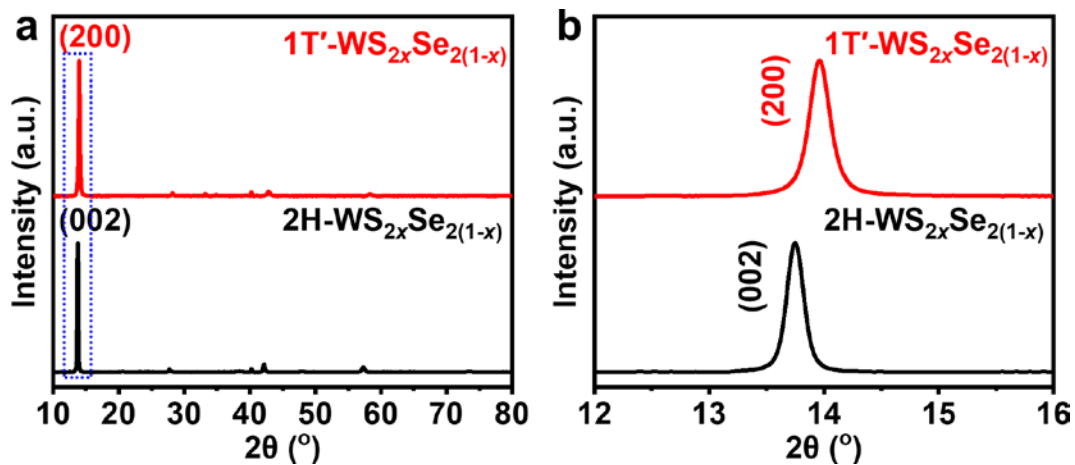
TGA and DSC were also used to investigate the phase transition temperature of the as-prepared 1T'-WSe₂ crystals (**Supplementary Fig. 29**). Compared to 1T'-WS₂ (**Fig. 3a**), the phase transition begins at a higher temperature of 160.1 °C followed by an exothermic peak at 256.2 °C, indicating a greater thermal stability of 1T'-WSe₂. The TGA result shows no weight loss over the transition range, indicating its phase transition.

Supplementary Note 2

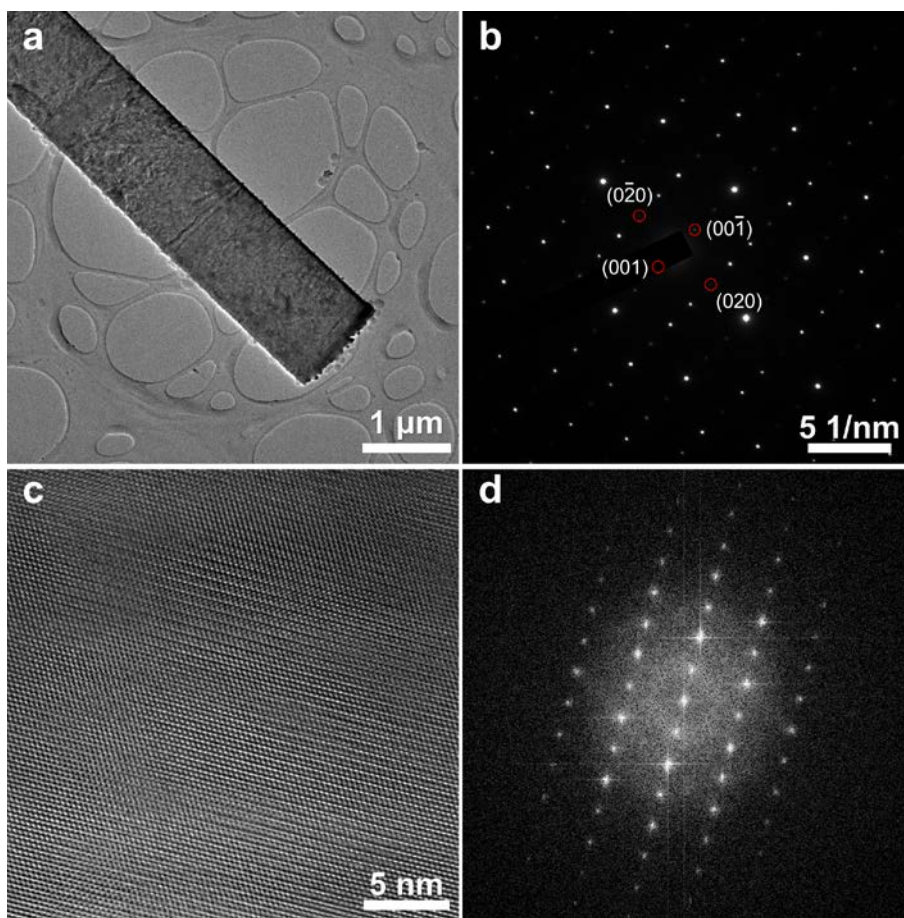
By changing the precursors and reaction conditions (see detailed information in **Supplementary Information**), ternary $1T'$ - $WS_{2x}Se_{2(1-x)}$ crystals with similar morphologies were prepared (**Supplementary Fig. 30a**). The chemical composition of as-prepared $1T'$ - $WS_{2x}Se_{2(1-x)}$ crystals was revealed by EDS, showing strong signals of W, S and Se elements (**Supplementary Fig. 30b**). The crystal structure of $1T'$ - $WS_{2x}Se_{2(1-x)}$ was further characterized and revealed by XRD (**Supplementary Fig. 31**), HRTEM and SAED (**Supplementary Fig. 32**), showing clear distorted $1T'$ structure. Moreover, the elemental mapping of the $1T'$ - $WS_{2x}Se_{2(1-x)}$ flake shows signals of W, S and Se elements uniformly distributed in the whole flake (**Supplementary Fig. 33**).



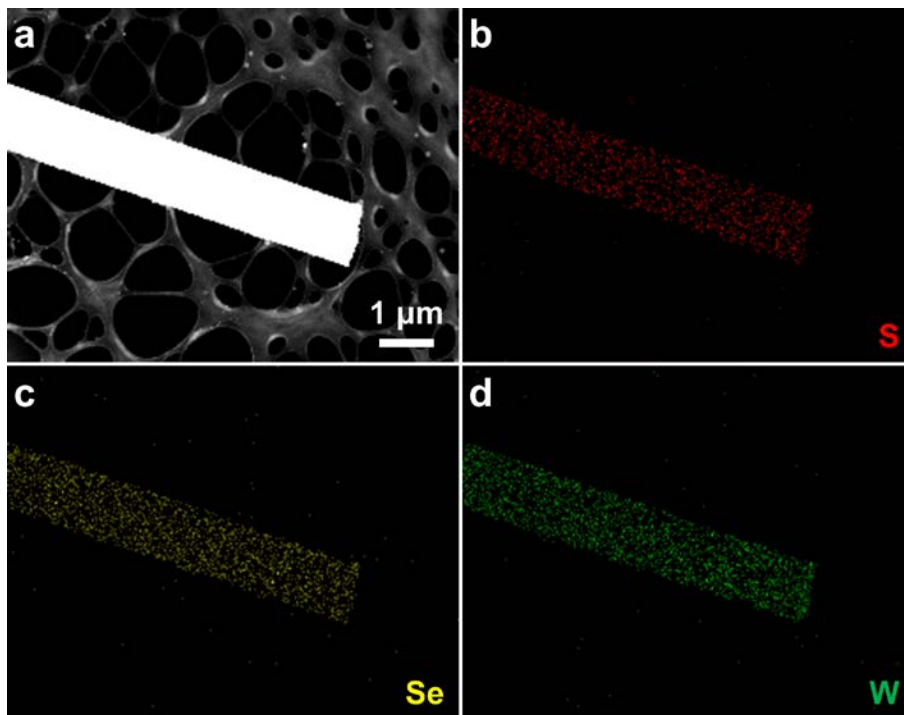
Supplementary Fig. 30 | Morphology and composition analysis of $1T'$ - $WS_{2x}Se_{2(1-x)}$ crystals. a, SEM image of the as-prepared $1T'$ - $WS_{2x}Se_{2(1-x)}$ crystals. **b,** EDS spectrum of the prepared $1T'$ - $WS_{2x}Se_{2(1-x)}$ crystals.



Supplementary Fig. 31 | Structure characterization of 1T'- and 2H- $\text{WS}_{2x}\text{Se}_{2(1-x)}$ crystals. **a**, XRD patterns of 1T'- and 2H- $\text{WS}_{2x}\text{Se}_{2(1-x)}$ crystals. **b**, Magnified XRD pattern of the (200) peak of 1T'- $\text{WS}_{2x}\text{Se}_{2(1-x)}$ and (002) peak of 2H- $\text{WS}_{2x}\text{Se}_{2(1-x)}$ crystals, obtained from the blue dotted area in (a).



Supplementary Fig. 32 | Structure characterization of 1T'-WS_{2x}Se_{2(1-x)} crystals. **a**, Low-magnification TEM image of a 1T'-WS_{2x}Se_{2(1-x)} flake. **b**, SAED pattern taken from the 1T'-WS_{2x}Se_{2(1-x)} flake in **(a)**. **c**, HRTEM image taken on a thin edge of the 1T'-WS_{2x}Se_{2(1-x)} flake in **(a)**. **d**, Corresponding FFT pattern obtained from the HRTEM image in **(c)**.



Supplementary Fig. 33 | Elemental mapping of a $1T'$ - $WS_{2x}Se_{2(1-x)}$ flake. **a**, Dark-field STEM image of a $1T'$ - $WS_{2x}Se_{2(1-x)}$ flake. **b-d**, Elemental mapping images of the $1T'$ - $WS_{2x}Se_{2(1-x)}$ flake in **(a)**: **(b)** S K signals, **(c)** Se K signals, and **(d)** W L signals.

1.2. 1T'-MoS₂, 1T'-MoSe₂, and 1T'-MoS_{2-x}Se_{2(1-x)}

Supplementary Note 3

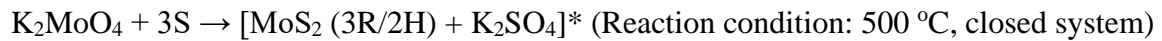
Besides the 1T'-WS₂, 1T'-WSe₂ and 1T'-WS_{2-x}Se_{2(1-x)}, three more 1T'-TMD crystals, including 1T'-MoS₂, 1T'-MoSe₂ and 1T'-MoS_{2-x}Se_{2(1-x)}, have also been synthesized by using the similar method (see the detailed information in **Methods** section in main text). For example, the morphology and crystal size of as-prepared 1T'-MoS₂ (**Supplementary Fig. 34a**) are similar with the reported result⁸ with an atomic ratio of ~1:2 for Mo and S elements (**Supplementary Fig. 34b**). As shown in **Supplementary Tables 1-3** and **Supplementary Fig. 2c**, our as-prepared 1T'-MoS₂ crystallizes in a monoclinic symmetry with the space group of *C2/m* (space group number 12; $a = 12.835(6)$ Å, $b = 3.1838(14)$ Å, $c = 5.662(2)$ Å, $\beta = 113.695(11)^\circ$ and $V = 211.86(16)$ Å³). The powder XRD pattern of our as-prepared 1T'-MoS₂ also well matches the simulated XRD pattern of the 1T'-MoS₂ crystal (**Supplementary Fig. 35**), confirming the pure phase of our as-prepared 1T'-MoS₂. Furthermore, the XRD pattern shows that the (200) peak of 1T'-MoS₂ also shifts to a higher degree as compared with the (002) peak of 2H-MoS₂ (**Supplementary Fig. 36**), which is similar to the 1T'-WS₂ (**Fig. 1d**). The SAED pattern obtained from a 1T'-MoS₂ flake clearly shows the 1T' structure diffraction feature (**Supplementary Fig. 37a-b**), which is consistent with a previous reported result⁸. The crystal structure of 1T'-MoS₂ was further confirmed by HRTEM (**Supplementary Fig. 37c-d**), showing the distorted 1T' phase structure characteristic.

In addition, as shown in **Supplementary Fig. 38**, the thermostability of 1T'-MoS₂ crystals was also studied by DSC and TGA. Obviously, a clear exothermic peak located at 106.3 °C was observed (black line in **Supplementary Fig. 38**), while the weight of the

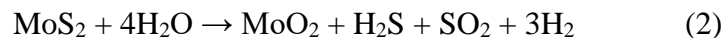
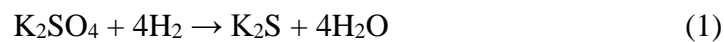
1T'-MoS₂ crystals remained unchanged during the heating process (blue line in **Supplementary Fig. 38**), indicating the successful phase transition from 1T' to 2H. The starting temperature of phase transition of 1T'-MoS₂ is ~60.1 °C, which is similar to the previously reported result⁸.

Moreover, to investigate the possible formation mechanism of 1T'-MoS₂ using our current closed-system (*cs*) gas-solid method, EDS and XRD were carried out to characterize the precursor, referred to as *cs*-MoS₂-precursor, obtained during the synthesis of 1T'-MoS₂. As shown in **Supplementary Fig. 39a**, similar to the *cs*-WS₂-precursor (**Supplementary Fig. 17a**), the XRD pattern of the precursor obtained during the preparation of 1T'-MoS₂ can be indexed to 2H/3R-MoS₂ (see the peaks indicated by arrows in **Supplementary Fig. 39a**), which is similar to the result reported by Toh et al.², and K₂SO₄. The EDS results (taken on more than 10 areas) showed the signals of Mo, K, S and O with the atomic ratio close to 1:2:3:8 (**Supplementary Fig. 39b**). Note that additional O signal may arise from the conductive carbon tape and the SEM characterization system. Therefore, we can speculate that the precursor is possibly [2H/3R-MoS₂+K₂SO₄]*.

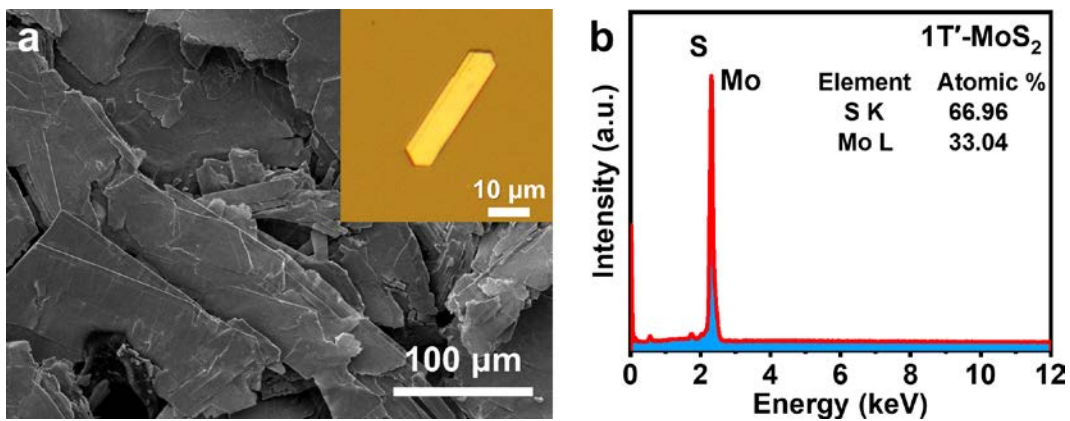
The reaction happened in the sealed quartz ampoule using our current closed-system gas-solid method could be proposed below.



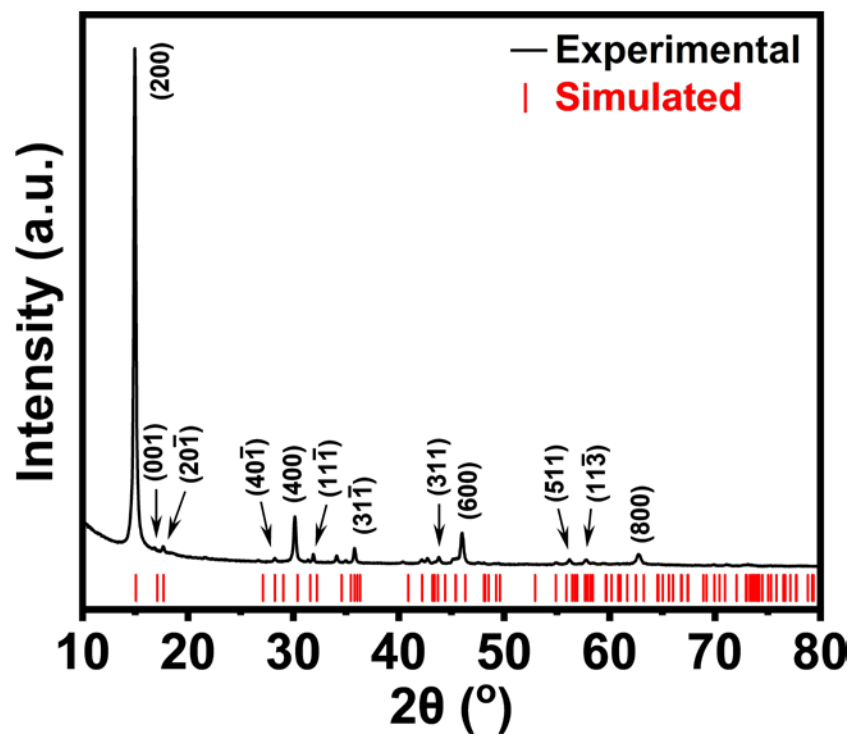
The possible mechanism for the formation of 1T'-MoS₂ crystal could be proposed and described as follows, which is similar to that of our as-prepared 1T'-WS₂.



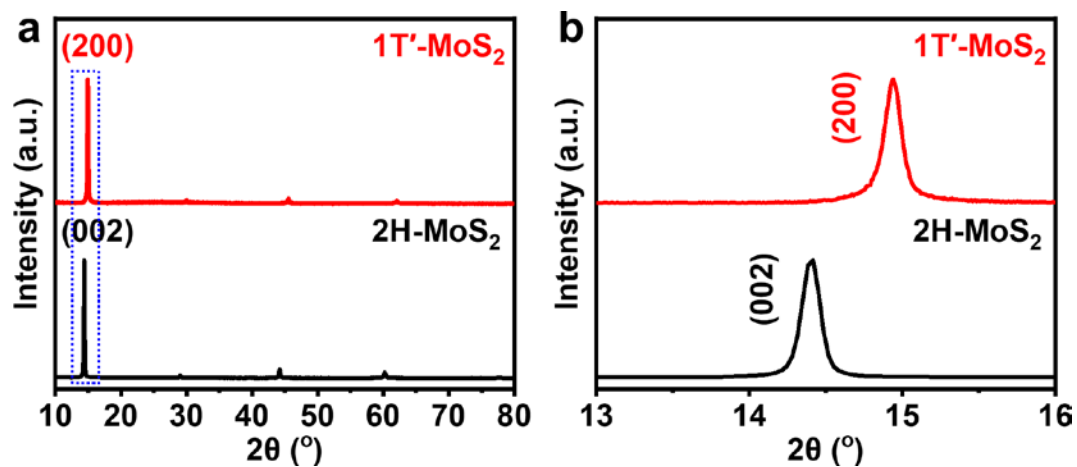
To further confirm the proposed possible mechanism, a control experiment was conducted by using the mixed powders of commercial 2H-MoS₂ and K₂SO₄ with the molar ratio of 1:1 to replace the precursor obtained by the reaction of K₂MoO₄ with S in sealed ampoule. As shown in **Supplementary Fig. 40**, the XRD pattern confirms the obtained MoS₂ with mixed 1T' and 2H phases (see the peaks indicated by arrows in **Supplementary Fig. 40**). Although the result could partially support our proposed mechanism, more studies should be carried out in the future to fully understand the mechanism on the formation of 1T'-MoS₂ by using our method.



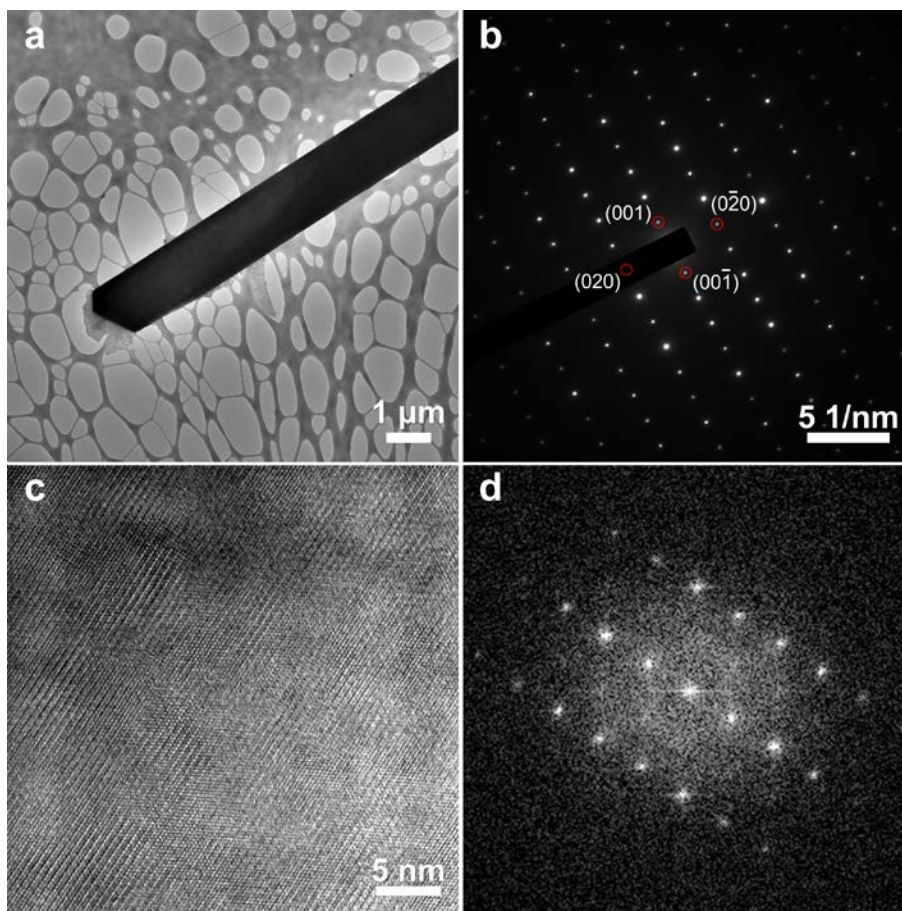
Supplementary Fig. 34 | Morphology and composition analysis of 1T'-MoS₂ crystals. a, SEM image of the as-prepared 1T'-MoS₂ crystals. Inset: optical image of a 1T'-MoS₂ crystal. **b**, EDS spectrum of the as-prepared 1T'-MoS₂ crystals.



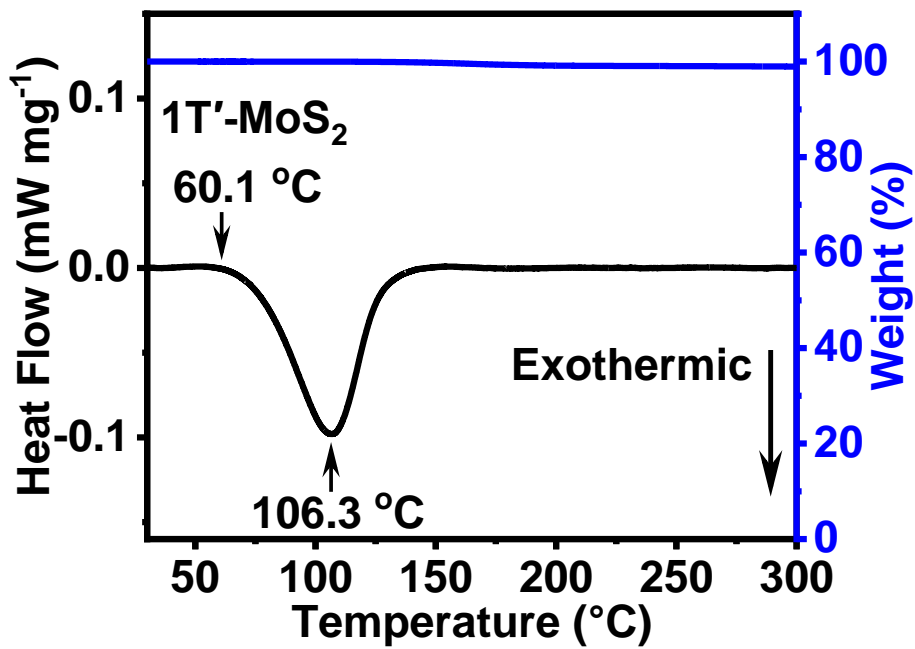
Supplementary Fig. 35 | Comparison of experimental and simulated XRD patterns of the as-prepared 1T'-MoS₂.



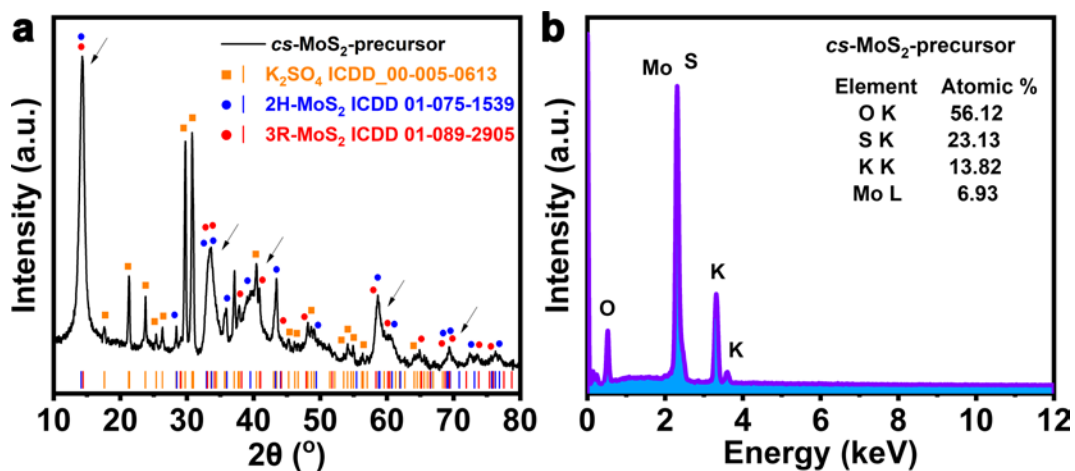
Supplementary Fig. 36 | Structure characterization of 1T'- and 2H-MoS₂ crystals. **a**, XRD patterns of 1T'- and 2H-MoS₂ crystals. **b**, Magnified XRD patterns of the (200) peak of 1T'-MoS₂ and (002) peak of 2H-MoS₂ crystals, obtained from the blue dotted area in (a).



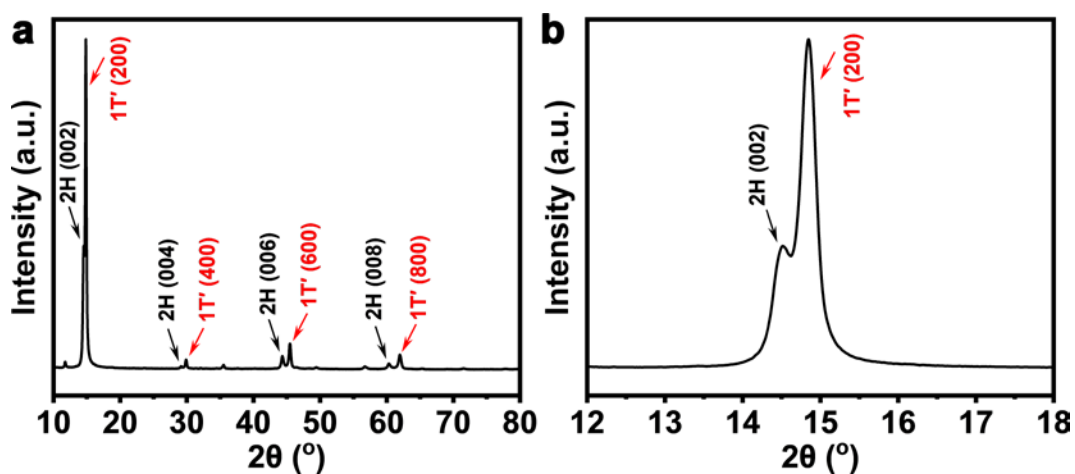
Supplementary Fig. 37 | Structure characterization of 1T'-MoS₂ crystals. **a**, Low-magnification TEM image of a 1T'-MoS₂ flake. **b**, SAED pattern taken from the 1T'-MoS₂ flake in **(a)**. **c**, HRTEM image taken on a thin edge of the 1T'-MoS₂ flake in **(a)**. **d**, Corresponding FFT pattern obtained from the HRTEM image in **(c)**.



Supplementary Fig. 38 | TGA-DSC curves of the as-prepared 1T'-MoS₂ crystals.



Supplementary Fig. 39 | (a) XRD pattern and (b) EDS spectrum of *cs*-MoS₂-precursor obtained by our closed-system gas-solid method.



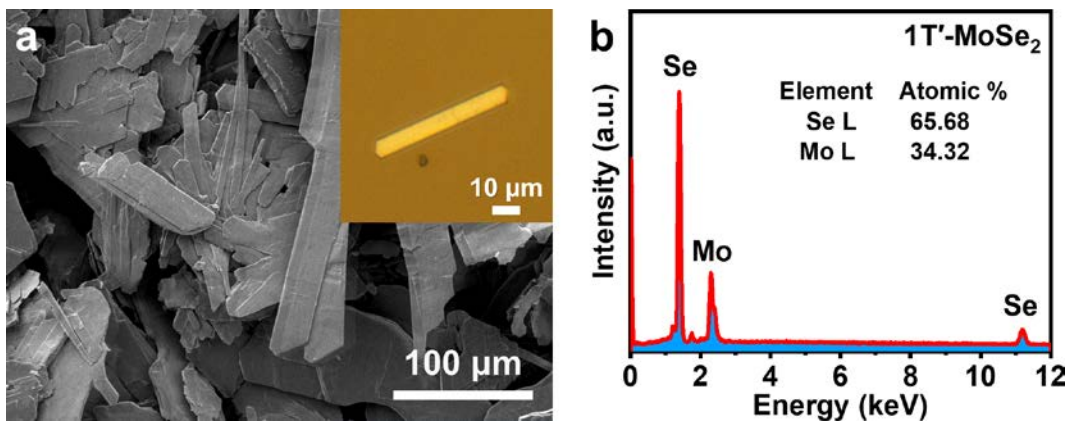
Supplementary Fig. 40 | XRD characterization of MoS₂ obtained by using the mixture of commercial 2H-MoS₂ and K₂SO₄. **a**, XRD patterns of MoS₂ obtained using the mixture of commercial 2H-MoS₂ and K₂SO₄, showing the mixed 1T' and 2H phases. **b**, Magnified XRD patterns of the (200) and (002) peaks of 1T' and 2H phases, respectively, in (a).

Supplementary Note 4

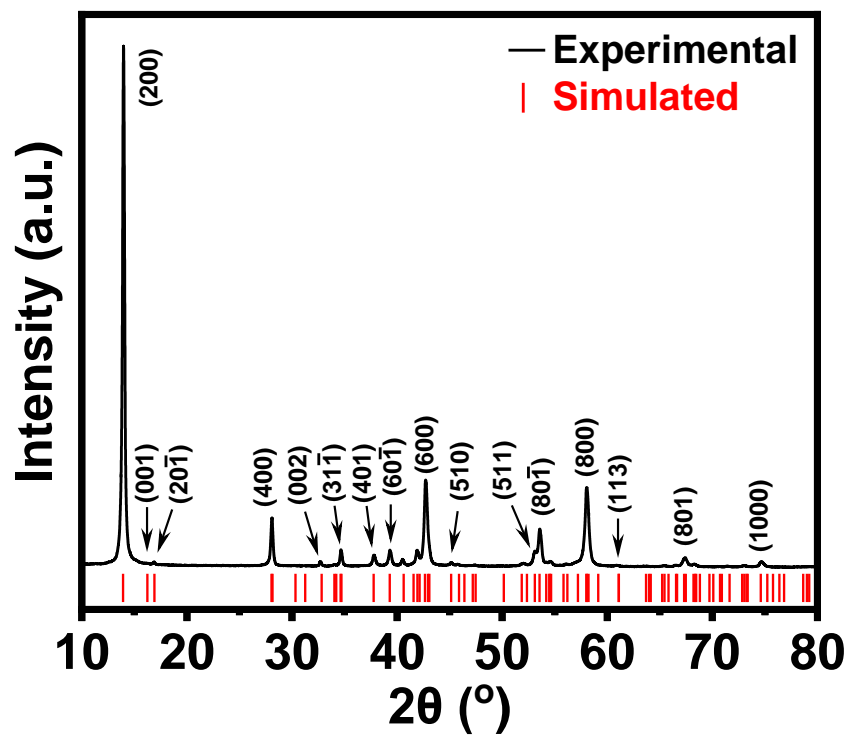
The 1T'-MoSe₂ crystals were also synthesized by using the similar procedures for the preparation of 1T'-WSe₂ but with different precursors (see the detailed information in Experimental Section in **Supplementary Information**). The morphology and chemical composition of as-prepared 1T'-MoSe₂ crystals were revealed by SEM and EDS characterizations (**Supplementary Fig. 41**), showing crystal size of a few hundred micrometers and the atomic ratio of ~1:2 (Mo to Se). The SCXRD analysis (**Supplementary Tables 1-3** and **Supplementary Fig. 2d**) reveals that our as-prepared 1T'-MoSe₂ crystallizes in a monoclinic symmetry (space group: *C2/m*) with the structure parameters of $a = 13.742(4) \text{ \AA}$, $b = 3.2704(9) \text{ \AA}$, $c = 5.895(1) \text{ \AA}$, $\beta = 112.344(8)^\circ$ and $V = 245.05(11) \text{ \AA}^3$. The powder XRD pattern of our as-prepared 1T'-MoSe₂ also well matches the simulated XRD pattern of the 1T'-MoSe₂ crystal (**Supplementary Fig. 42**), confirming the pure phase of our as-prepared 1T'-MoSe₂. As shown in **Supplementary Fig. 43**, a small shift on (200) peak of 1T'-MoSe₂ to higher degree as compared with the (002) peak of 2H-MoSe₂ was also observed, which is consistent with the SCXRD data. The SAED pattern and HRTEM image further confirm the crystal structure of as-prepared 1T'-MoSe₂ (**Supplementary Fig. 44**), clearly showing the distorted octahedral coordinated diffraction feature and zigzag Mo chains originated from the 1T' phase structure.

In addition, as shown in **Supplementary Fig. 45**, the thermal stability of the as-prepared 1T'-MoSe₂ crystals was also studied by DSC and TGA. Obviously, a clear exothermic peak located at 126.8 °C is observed (black line **Supplementary Fig. 45**), while there is no observable weight loss of the 1T'-MoSe₂ crystals during the heating process (blue line **Supplementary Fig. 45**), indicating the phase transition from 1T' to 2H.

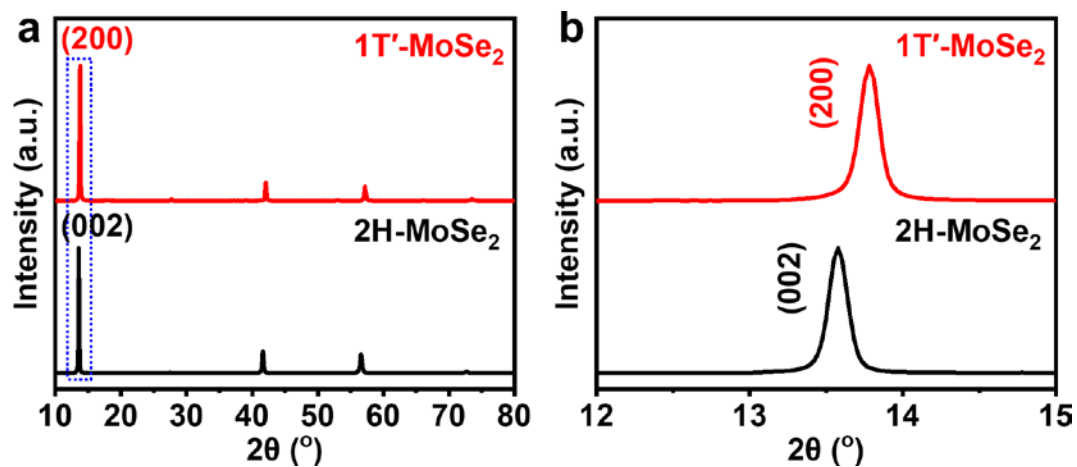
It is worth mentioning that the exothermic heat flow starts at ~ 72.2 °C, revealing the starting phase transition temperature of the as-prepared 1T'-MoSe₂.



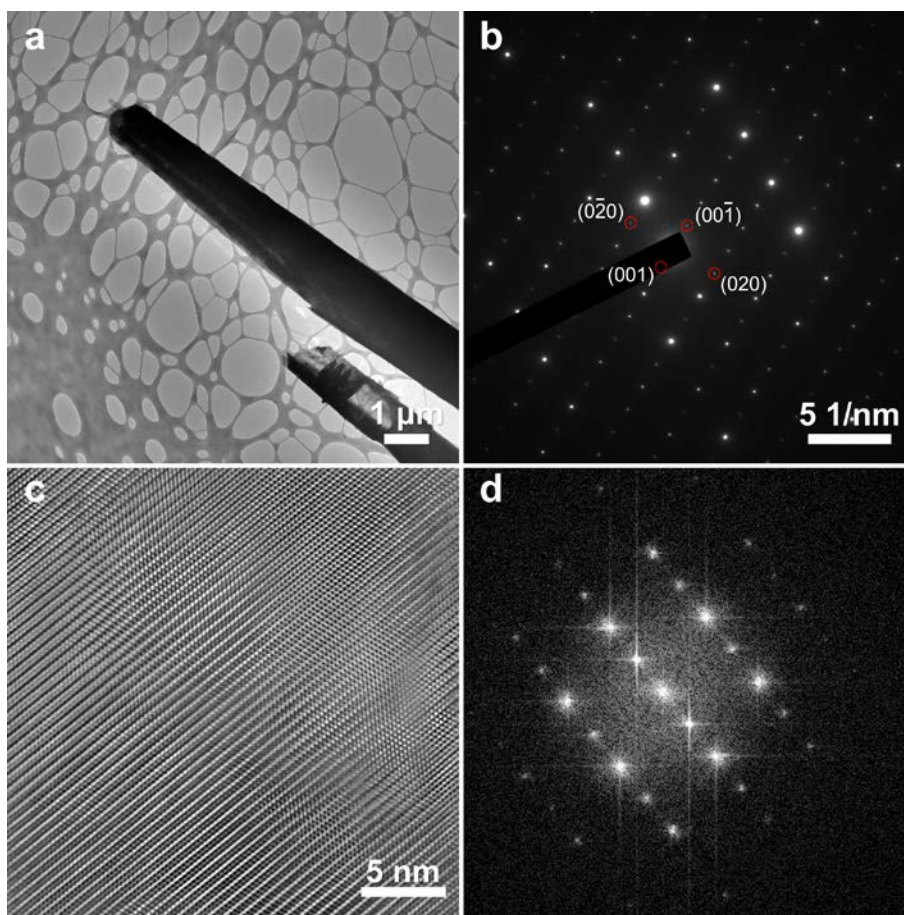
Supplementary Fig. 41 | Morphology and composition analysis of 1T'-MoSe₂ crystals. **a**, SEM image of the as-prepared 1T'-MoSe₂ crystals. Inset: optical image of a 1T'-MoSe₂ crystal. **b**, EDS spectrum of the as-prepared 1T'-MoSe₂ crystals.



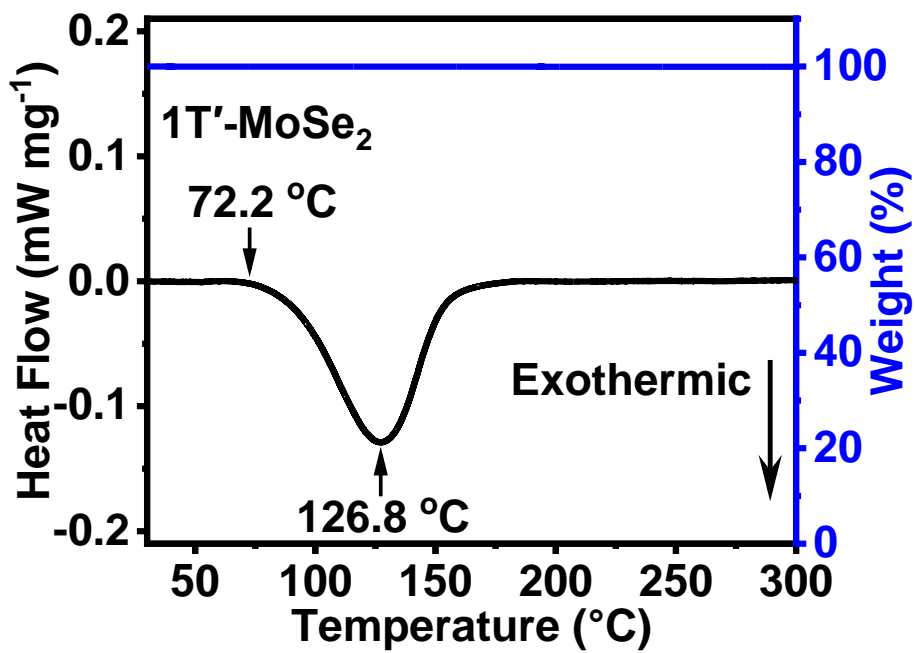
Supplementary Fig. 42 | Comparison of experimental and simulated XRD patterns of the as-prepared 1T'-MoSe₂.



Supplementary Fig. 43 | Structure characterization of 1T'- and 2H-MoSe₂ crystals. (a) XRD patterns of 1T'- and 2H-MoSe₂ crystals. **(b)** Magnified XRD patterns of the (200) peak of 1T'-MoSe₂ and (002) peak of 2H-MoSe₂ crystals, obtained from the blue dotted area in (a).



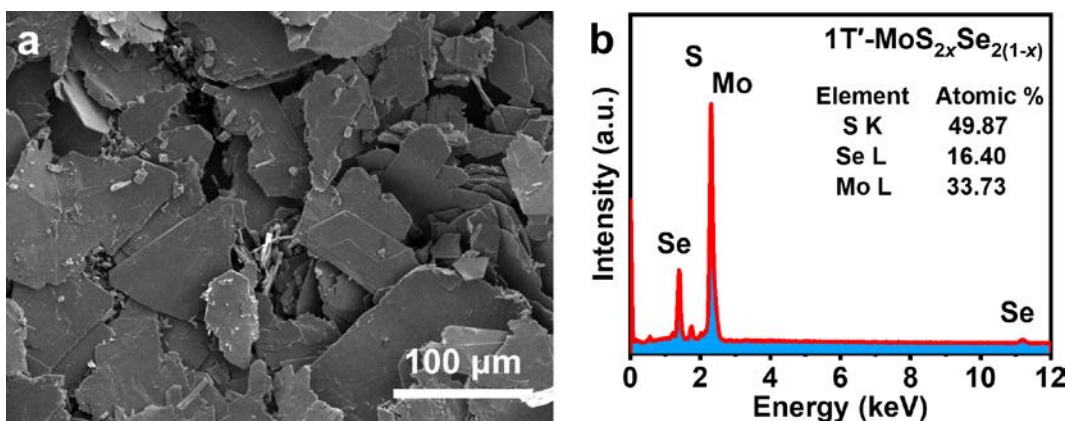
Supplementary Fig. 44 | Structure characterization of 1T'-MoSe₂ crystals. **a**, Low-magnification TEM image of a 1T'-MoSe₂ flake. **b**, SAED pattern taken from the 1T'- MoSe₂ flake in (a). **c**, HRTEM image taken on a thin edge of the 1T'-MoSe₂ flake in (a). **d**, Corresponding FFT pattern obtained from the HRTEM image in (c).



Supplementary Fig. 45 | TGA-DSC curves of the as-prepared 1T'-MoSe₂ crystals.

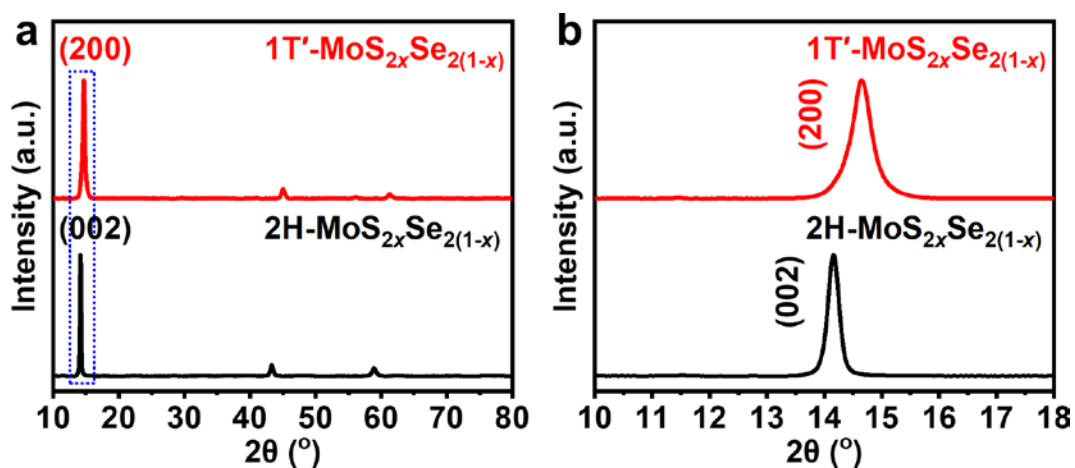
Supplementary Note 5

In addition, ternary $1T'$ - $\text{MoS}_{2x}\text{Se}_{2(1-x)}$ crystals have also been synthesized using the similar method but with different precursors (see the detailed information in Experimental Section in **Supplementary Information**). As shown in **Supplementary Fig. 46a**, the crystal size of the as-prepared $1T'$ - $\text{MoS}_{2x}\text{Se}_{2(1-x)}$ is similar to that of $1T'$ - MoS_2 (**Supplementary Fig. 34a**) and $1T'$ - MoSe_2 (**Supplementary Fig. 41a**). EDS spectrum taken on the as-prepared $1T'$ - $\text{MoS}_{2x}\text{Se}_{2(1-x)}$ crystals confirms the presence of Mo, S and Se (**Supplementary Fig. 46b**). Similar with that of $1T'$ - MoS_2 (**Supplementary Fig. 36**) and $1T'$ - MoSe_2 (**Supplementary Fig. 43**), the (200) peak in the XRD pattern obtained from $1T'$ - $\text{MoS}_{2x}\text{Se}_{2(1-x)}$ also shifts to a higher degree compared to the (002) peak of $2H$ - $\text{MoS}_{2x}\text{Se}_{2(1-x)}$ (**Supplementary Fig. 47**). The crystal structure of $1T'$ - $\text{MoS}_{2x}\text{Se}_{2(1-x)}$ was further revealed by the SAED pattern and HRTEM image (**Supplementary Fig. 48**), showing the distorted octahedral $1T'$ structure characteristics. Moreover, the elemental mapping was carried out on the prepared $1T'$ - $\text{MoS}_{2x}\text{Se}_{2(1-x)}$ crystals, showing a uniform distribution of Mo, S and Se signals throughout the whole crystal flake (**Supplementary Fig. 49**).



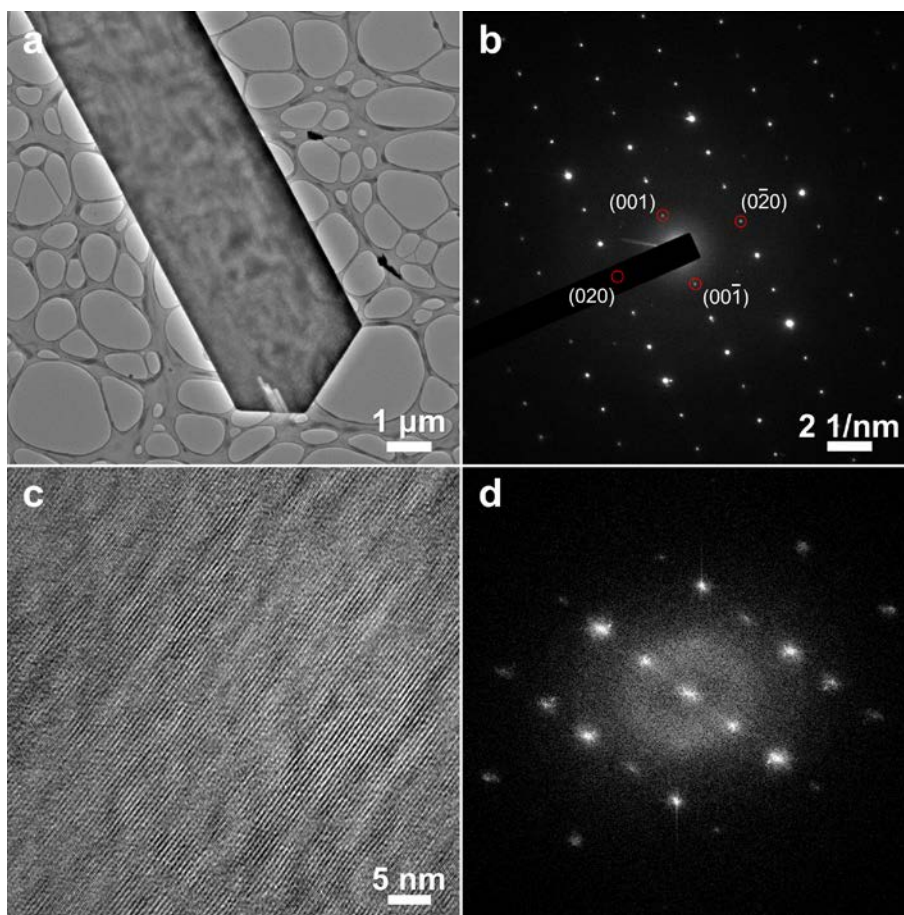
Supplementary Fig. 46 | Morphology and composition analysis of $1T'$ - $\text{MoS}_{2x}\text{Se}_{2(1-x)}$ crystals.

a, SEM image of the as-prepared $1T'$ - $\text{MoS}_{2x}\text{Se}_{2(1-x)}$ crystals. **b**, EDS spectrum of the as-prepared $1T'$ - $\text{MoS}_{2x}\text{Se}_{2(1-x)}$ crystals.

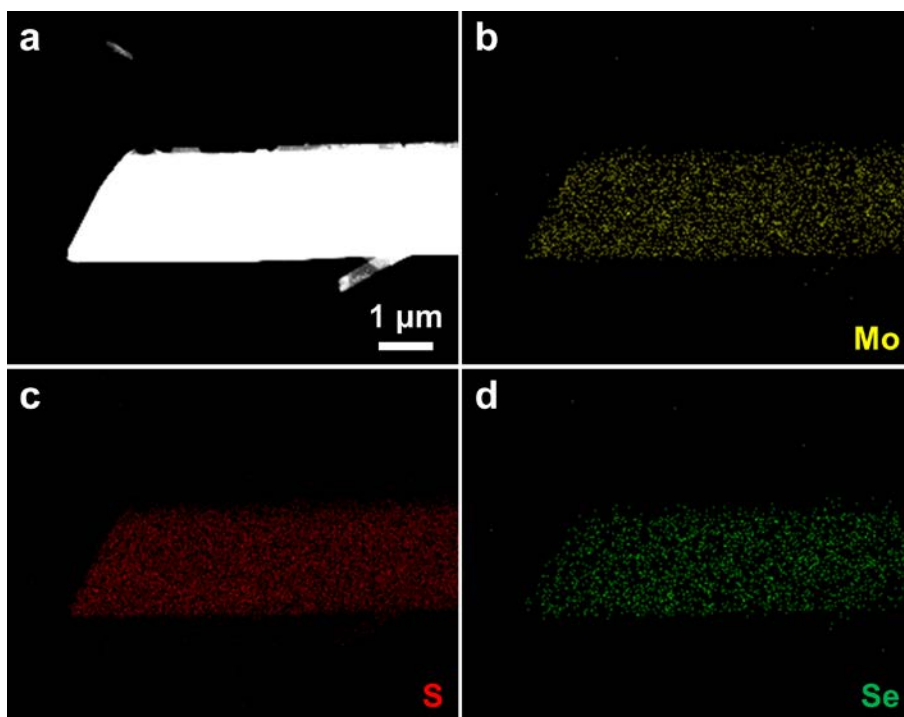


Supplementary Fig. 47 | Structure characterization of $1T'$ - and $2H$ - $\text{MoS}_{2x}\text{Se}_{2(1-x)}$ crystals. a,

XRD patterns of $1T'$ - and $2H$ - $\text{MoS}_{2x}\text{Se}_{2(1-x)}$ crystals. **b**, Magnified XRD patterns of the (200) peak of $1T'$ - $\text{MoS}_{2x}\text{Se}_{2(1-x)}$ and (002) peak of $2H$ - $\text{MoS}_{2x}\text{Se}_{2(1-x)}$ crystals, obtained from the blue dotted area in (a).

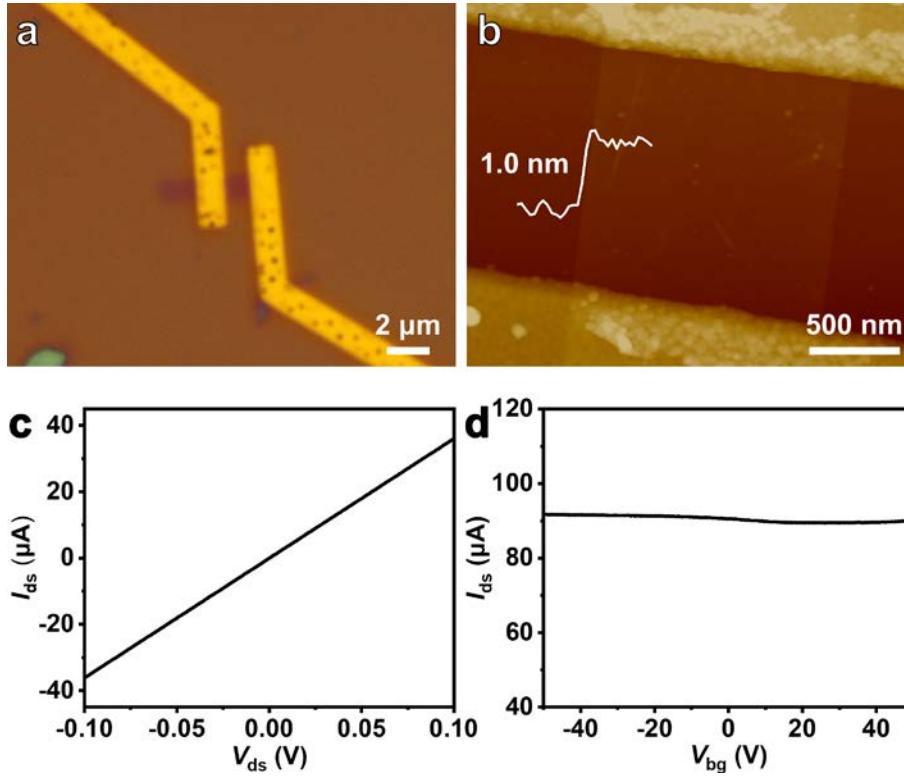


Supplementary Fig. 48 | Structure characterization of 1T'-MoS_{2x}Se_{2(1-x)} crystals. **a**, Low-magnification TEM image of a 1T'-MoS_{2x}Se_{2(1-x)} flake. **b**, SAED pattern taken from the 1T'-MoS_{2x}Se_{2(1-x)} flake in **(a)**. **(c)** HRTEM image taken on a thin edge of the 1T'-MoS_{2x}Se_{2(1-x)} flake in **(a)**. **d**, Corresponding FFT pattern obtained from the HRTEM image in **(c)**.

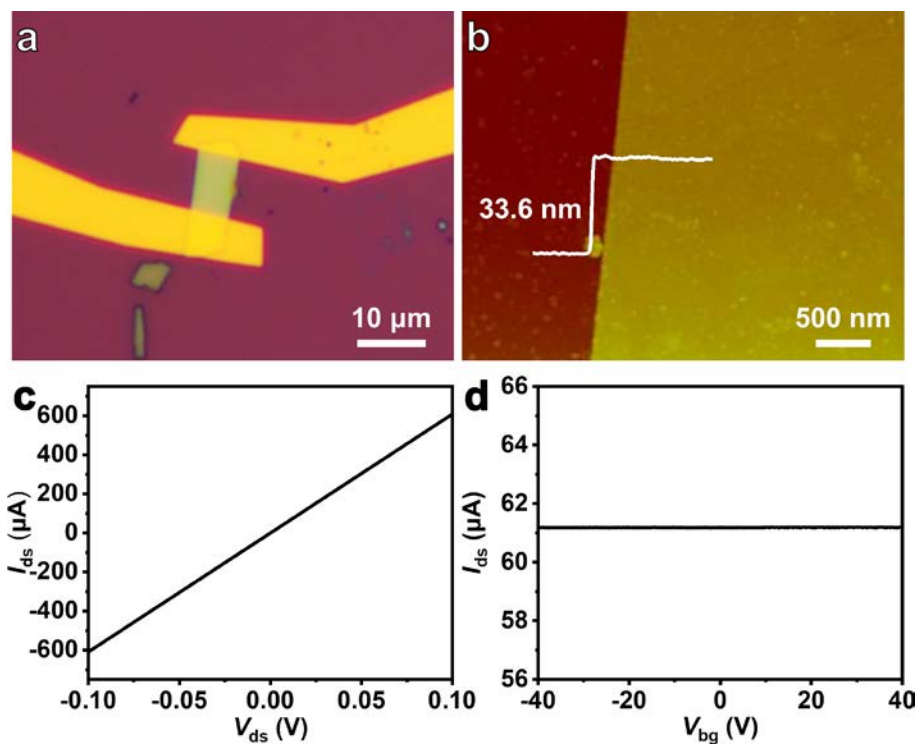


Supplementary Fig. 49 | Elemental mapping of a 1T'-MoS_{2x}Se_{2(1-x)} flake. a, Dark-field STEM image of a 1T'-MoS_{2x}Se_{2(1-x)} flake. **b-d**, Elemental mapping images of the 1T'-MoS_{2x}Se_{2(1-x)} flake in **(a)**: **(b)** Mo K signals, **(c)** S K signals, and **(d)** Se K signals.

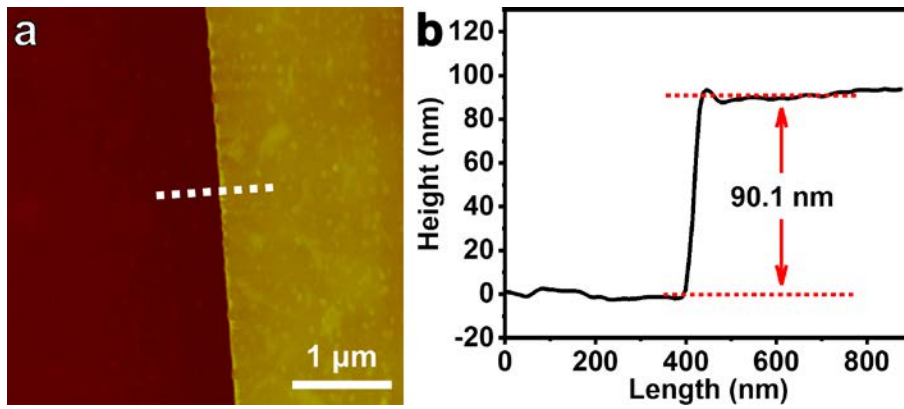
1.3. Electrical transport and superconducting measurements



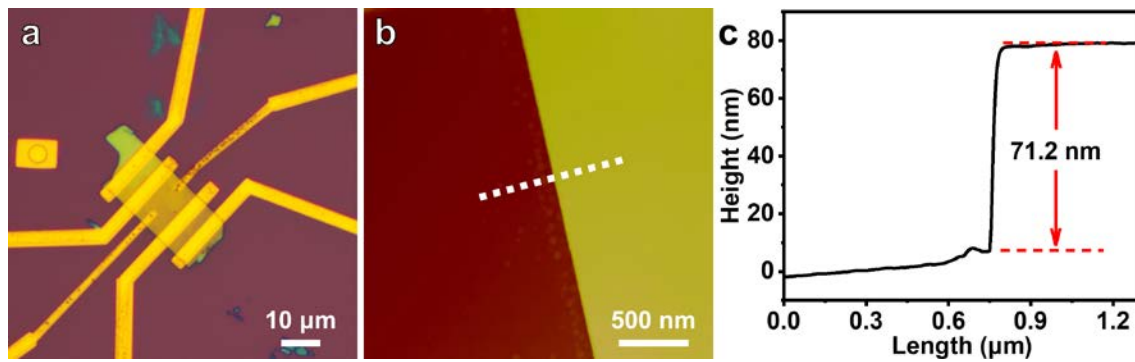
Supplementary Fig. 50 | Charge transport characteristics of a single-layer 1T'-WS₂. **a**, Optical image of a two-terminal device of single-layer 1T'-WS₂. **b**, AFM image obtained from the device in (a). Inset: AFM height profile obtained from the cross-section area in (b). **c**, I_{ds} - V_{ds} curve obtained from the device in (a), $V_{ds} = 0.5$ V. **d**, I_{ds} - V_{bg} curve obtained from the device in (a), showing a metallic charge transport.



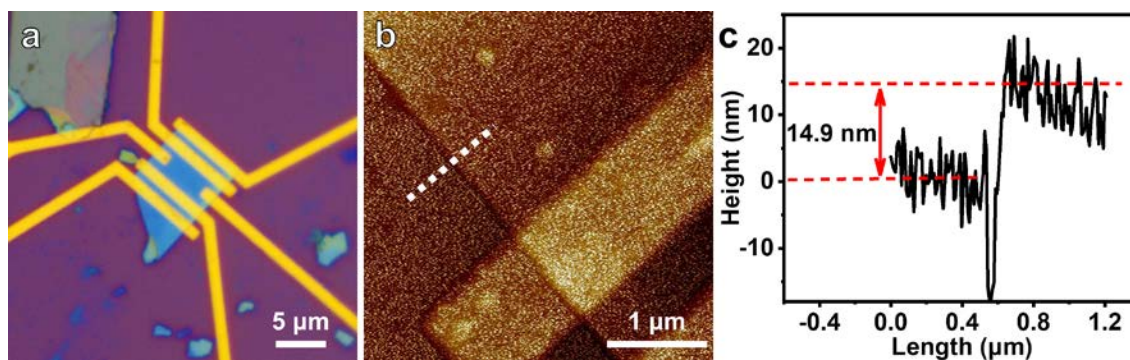
Supplementary Fig. 51 | Charge transport characteristics of 1T'-WSe₂. **a**, Optical image of a two-terminal device of 1T'-WSe₂ nanosheet. **b**, AFM image obtained from the device in **(a)**. Inset: AFM height profile obtained from the cross-section area in **(b)**. **c**, I_{ds} - V_{ds} curve obtained from the device in **(a)**, $V_{ds} = 0.1$ V. **d**, I_{ds} - V_{bg} curve obtained from the device in **(a)**, showing a metallic charge transport.



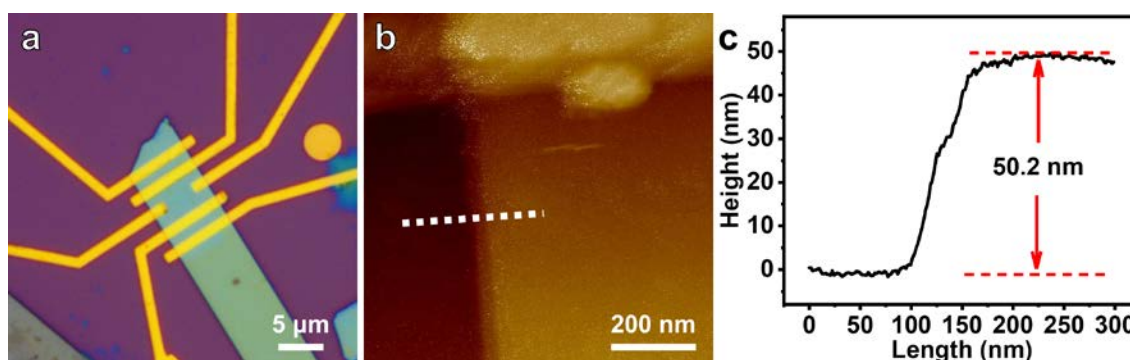
Supplementary Fig. 52 | AFM characterization of the 1T'-WS₂ device shown in the inset in Fig. 4a. a, AFM image obtained from the 1T'-WS₂ device. **b**, Height profile of the cross-section along the white dotted line in (a).



Supplementary Fig. 53 | Characterization of the 1T'-WSe₂ device. a, Optical image of the 1T'-WSe₂ device with four-probe configuration and Hall bars. **b**, AFM image obtained from the device in (a). **c**, Height profile of the cross-section along the white dotted line in (b).

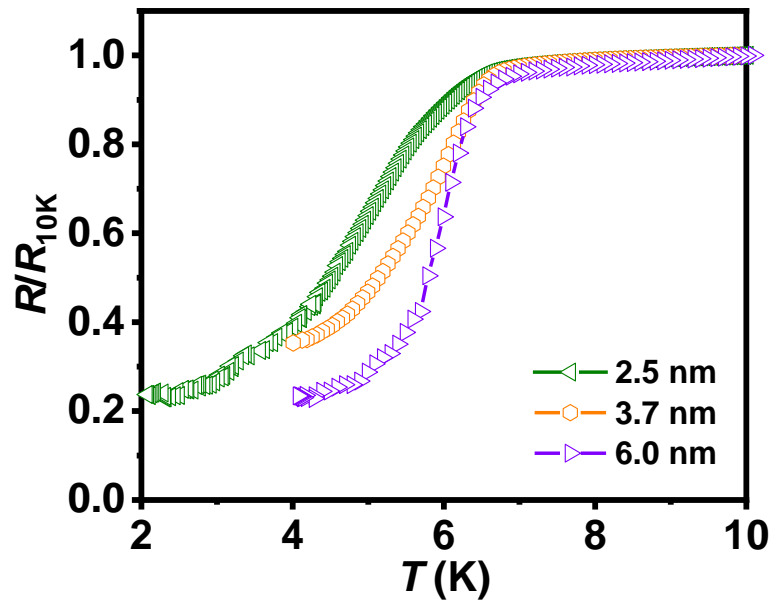


Supplementary Fig. 54 | Characterization of the 1T'-WS_{2x}Se_{2(1-x)} ($x = 0.796$) device. **a**, Optical image of the 1T'-WS_{2x}Se_{2(1-x)} ($x = 0.796$) device with four-probe configuration. **b**, AFM image obtained from the device in **(a)**. **c**, Height profile of the cross-section along the white dotted line in **(b)**.

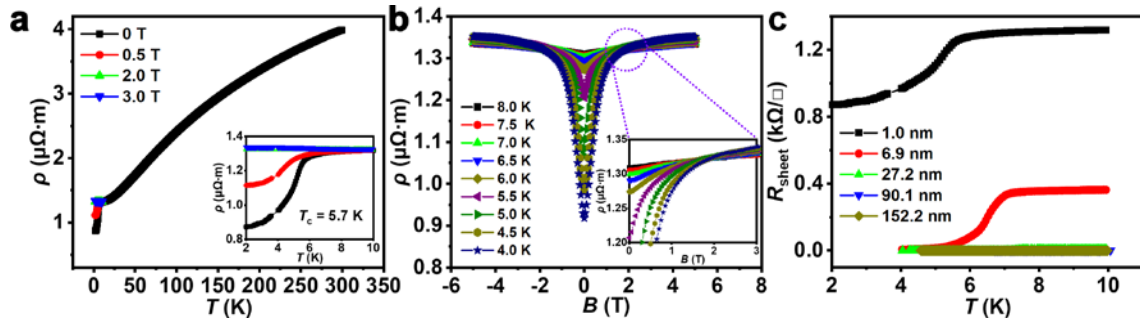


Supplementary Fig. 55 | Characterization of the 1T'-WS_{2x}Se_{2(1-x)} ($x = 0.472$) device. **a**, Optical image of the 1T'-WS_{2x}Se_{2(1-x)} ($x = 0.472$) device with four-probe configuration. **b**, AFM image obtained from the device in **(a)**. **c**, Height profile of the cross-section along the white dotted line in **(b)**.

Supplementary Fig. 56 to 63 show the temperature- and magnetic field-dependent electrical transport properties of the devices made of 1T'-WS₂ with different thicknesses. The out-of-plane upper critical magnetic fields, $B_{c2\perp}$, which were obtained from the ρ - B isotherms below T_c , are used to estimate the in-plane coherence length of each device. Furthermore, to reveal the two-dimensional (2D) feature of superconductivity, we have measured the electrical transport properties of two-probe devices made of 1T'-WS₂ with thicknesses of 2.5 and 6.0 nm, respectively (**Supplementary Fig. 59**), and a four-probe device made of 1T'-WS₂ with thickness of 152.2 nm (**Supplementary Fig. 60-61**) under both out-of-plane and in-plane magnetic fields.

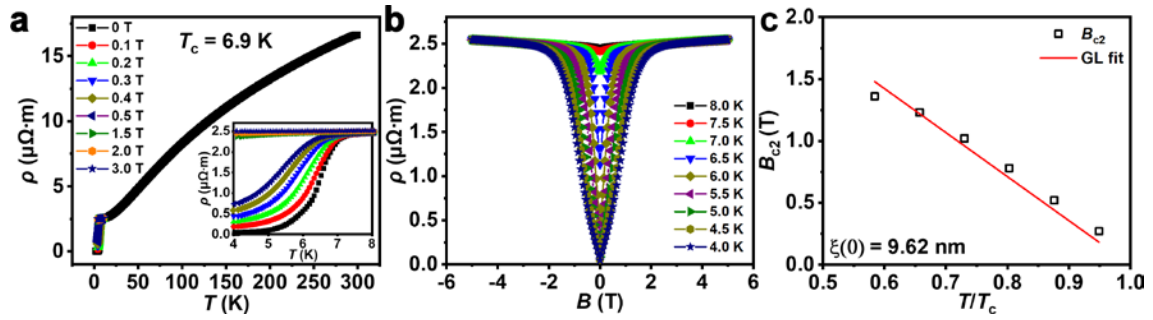


Supplementary Fig. 56 | R/R_{10K} - T plots of the two-probe devices made of 1T'-WS₂ nanosheets with thicknesses of 2.5, 3.7 and 6.0 nm below 10.0 K.



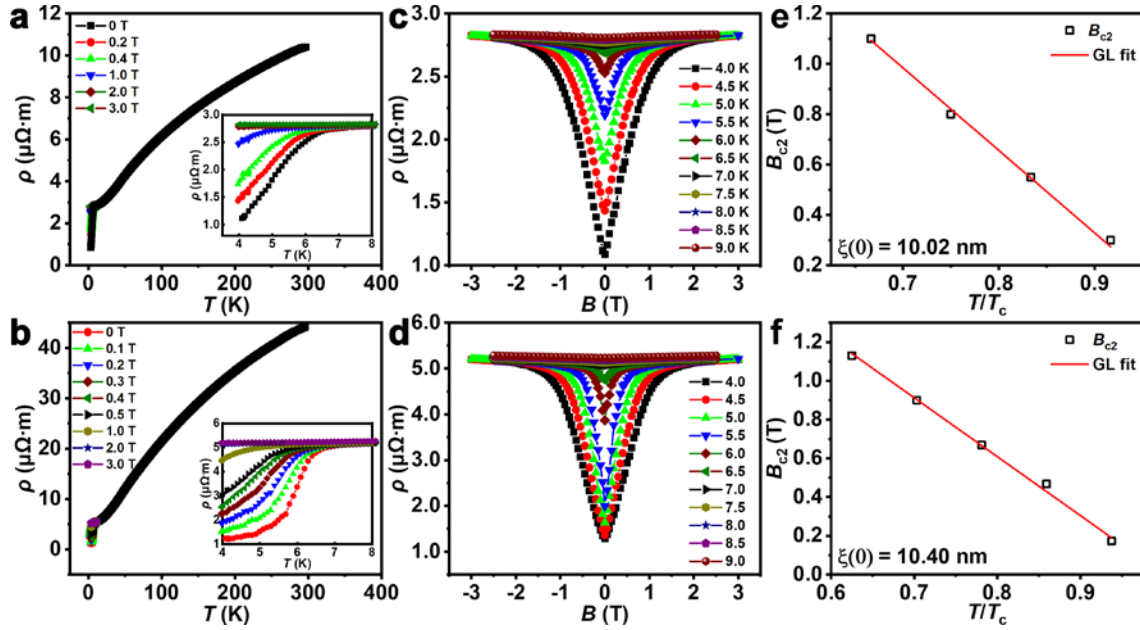
Supplementary Fig. 57 | Superconductivity measurements of the four-probe device made of single-layer (~ 1.0 nm) $1T'$ - WS_2 nanosheet under different out-of-plane magnetic fields. **a, Temperature-dependent resistivity (ρ - T) under different out-of-plane magnetic fields. Inset: high-resolution ρ - T plots below 10.0 K. **b**, ρ - B_{\perp} isotherms under out-of-plane magnetic fields around T_c . Inset: magnified ρ - B_{\perp} isotherms showing the cross-over behavior at the magnetic field of ~ 1.9 T, indicating the field-induced transition from the superconducting metallic state to the insulating phase. **c**, Plots of sheet resistance as a function of temperature for all four-probe devices made of $1T'$ - WS_2 nanosheets with different thicknesses below 10.0 K.**

The inset of **Supplementary Fig. 57a** clearly shows that the superconducting transition of single-layer $1T'$ - WS_2 occurs at 5.7 K without a magnetic field with the non-zero resistance down to 2.0 K. The superconducting state below T_c disappears and the device attains the normal state resistivity under the out-of-plane magnetic field above 2.0 T.

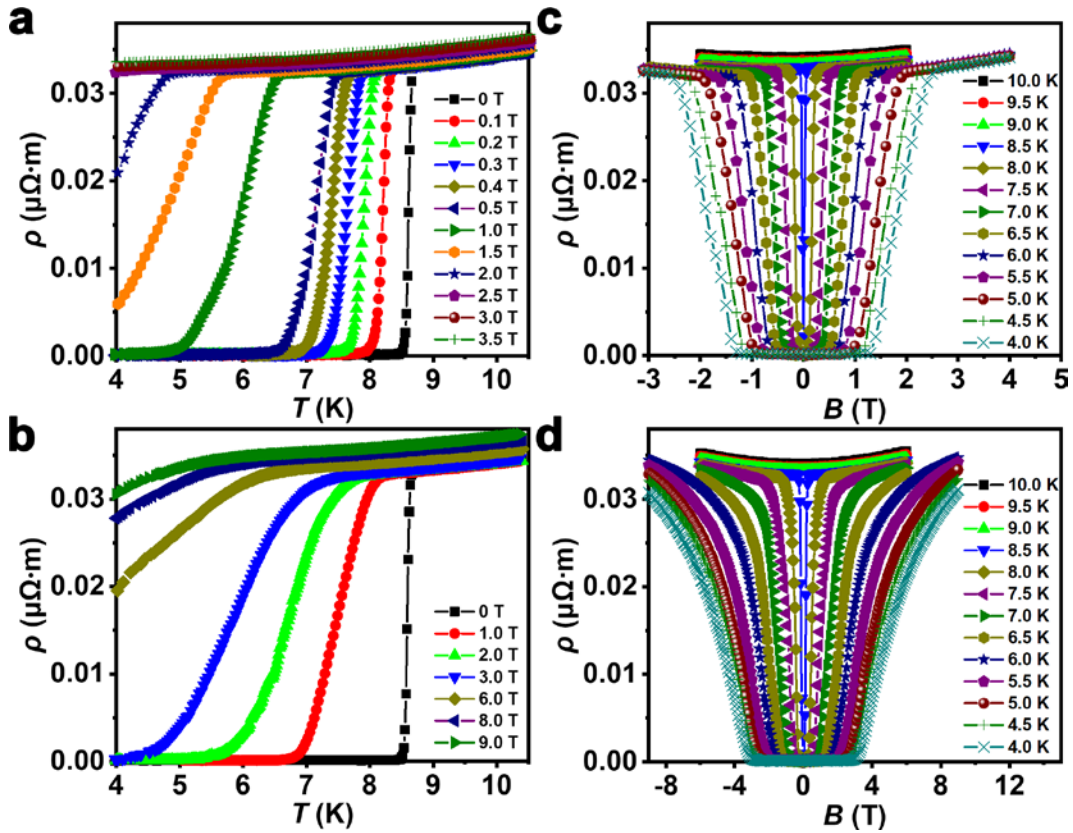


Supplementary Fig. 58 | Superconductivity measurements of the four-probe devices made of 1T'-WS₂ nanosheet with thickness of ~6.9 nm under different out-of-plane magnetic fields. a, Temperature-dependent resistivity (ρ - T) under different out-of-plane magnetic fields. Inset: high-resolution ρ - T plots below 8.0 K. **b,** ρ - B_{\perp} isotherms under out-of-plane magnetic fields at around T_c . **c,** Plot of out-of-plane upper critical magnetic field as a function of T/T_c , fitted with the GL equation to obtain the in-plane coherence length of 9.62 nm, which is larger than the thickness of the sample (6.9 nm).

The inset of **Supplementary Fig. 58a** clearly shows that the superconducting transition occurs at 6.9 K without a magnetic field, and the superconducting state disappears under the out-of-plane magnetic field above 2.0 T at 4.0 K.



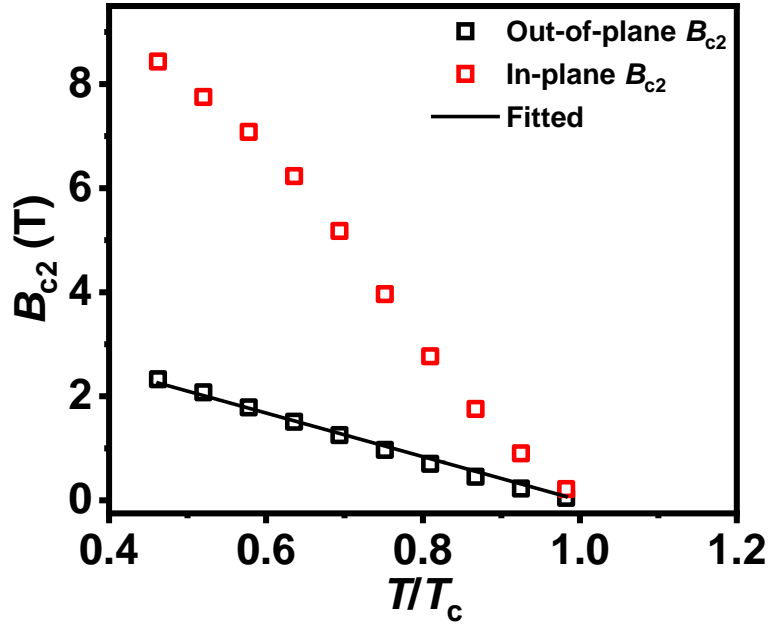
Supplementary Fig. 59 | Superconductivity measurements of the two-probe devices made of 1T'-WS₂ nanosheets with thicknesses of 2.5 and 6.0 nm under different out-of-plane magnetic fields. **a,b**, Temperature-dependent resistivity (ρ - T) of the devices of 1T'-WS₂ nanosheets with thicknesses of **(a)** 2.5 nm and **(b)** 6.0 nm under different out-of-plane magnetic fields. Insets: high-resolution ρ - T plots below 8.0 K. **c,d**, ρ - B_{\perp} isotherms of the devices made of 1T'-WS₂ nanosheets with thicknesses of **(c)** 2.5 nm and **(d)** 6.0 nm under out-of-plane magnetic fields at around T_c . **e,f**, Plots of out-of-plane upper critical magnetic fields as a function of T/T_c , fitted with GL equation to obtain the in-plane coherence length from the devices made of 1T'-WS₂ nanosheets with thicknesses of **(e)** 2.5 nm and **(f)** 6.0 nm. The obtained coherence lengths, 10.02 nm and 10.4 nm, are much larger than their thicknesses of 2.5 and 6.0 nm, respectively.



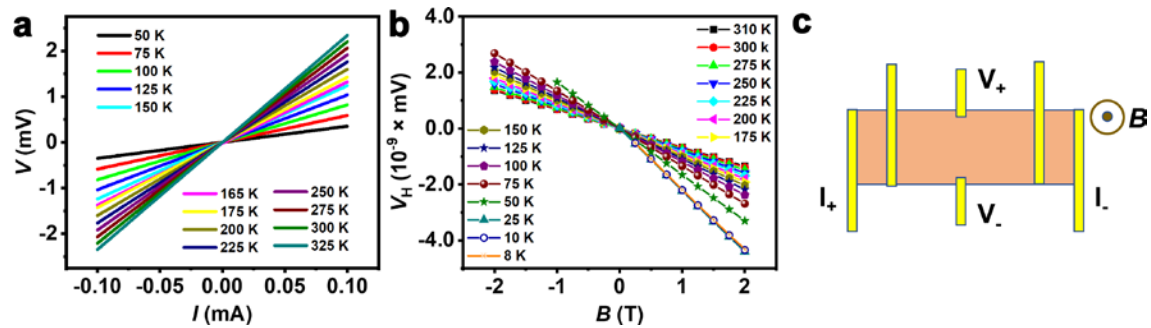
Supplementary Fig. 60 | Superconductivity measurements of the four-probe device made of 1T'-WS₂ nanosheet with thickness of 152.2 nm under different magnetic fields. a,b, Temperature-dependent resistivity (ρ - T) under (a) out-of-plane and (b) in-plane magnetic fields. c,d, ρ - B isotherms under (c) out-of-plane and (d) in-plane magnetic fields.

As shown in **Supplementary Fig. 60 a-b**, the superconducting transition occurs at $T_c = 8.7$ K without a magnetic field. T_c shifts to lower temperature as the magnetic field increases. The superconducting state completely disappears under the out-of-plane magnetic field above 2.5 T at 4.0 K (**Supplementary Fig. 60a**). In contrast, the superconducting state persists under the in-plane magnetic field up to 9.0 T at 4.0 K (**Supplementary Fig. 60b**). As shown in **Supplementary Fig. 60 c-d**, the ρ - B isotherms also show a large difference in the critical fields between out-of-plane and in-plane

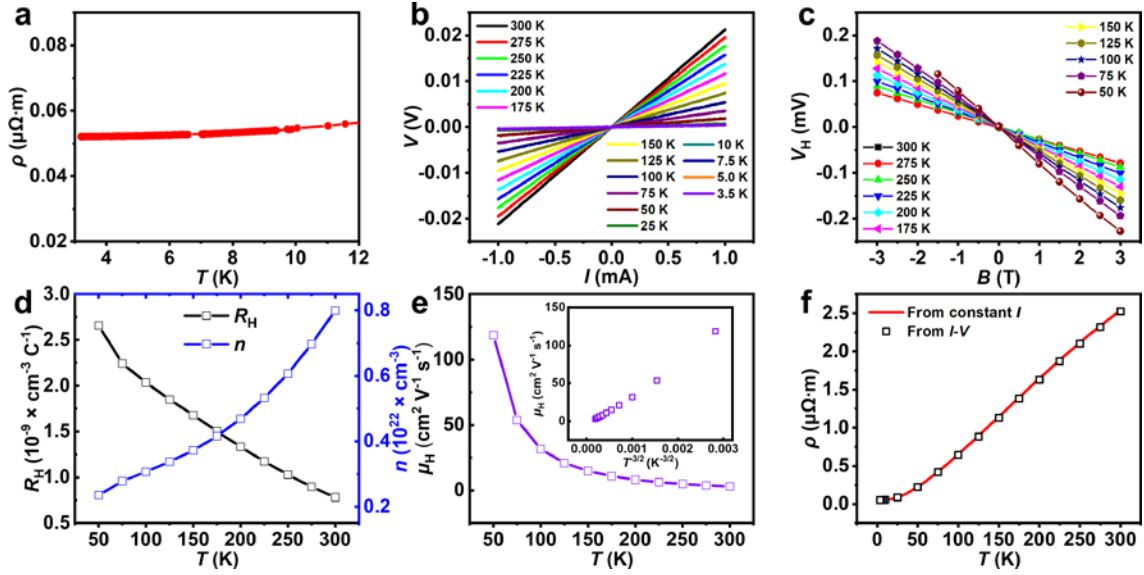
magnetic field-dependent resistivity measurements (ρ - B isotherms). The anisotropic nature in critical fields clearly indicates the signature of a 2D superconductor.



Supplementary Fig. 61 | Plots of upper critical magnetic fields as a function of T/T_c under out-of-plane and in-plane magnetic fields, respectively, obtained from the four-probe device made of 1T'-WS₂ nanosheet with thickness of 152.2 nm. The in-plane coherence length of 8.85 nm was obtained by fitting the out-of-plane critical magnetic fields with GL equation.



Supplementary Fig. 62 | Isotherms of (a) I - V characteristics and (b) Hall voltage as a function of applied magnetic field obtained from the device made of 1T'-WS₂ with thickness of 90.1 nm (**Fig. 4a**, **Supplementary Fig. 52**) at different temperatures. **c**, Schematic configuration of the Hall bar measurements.

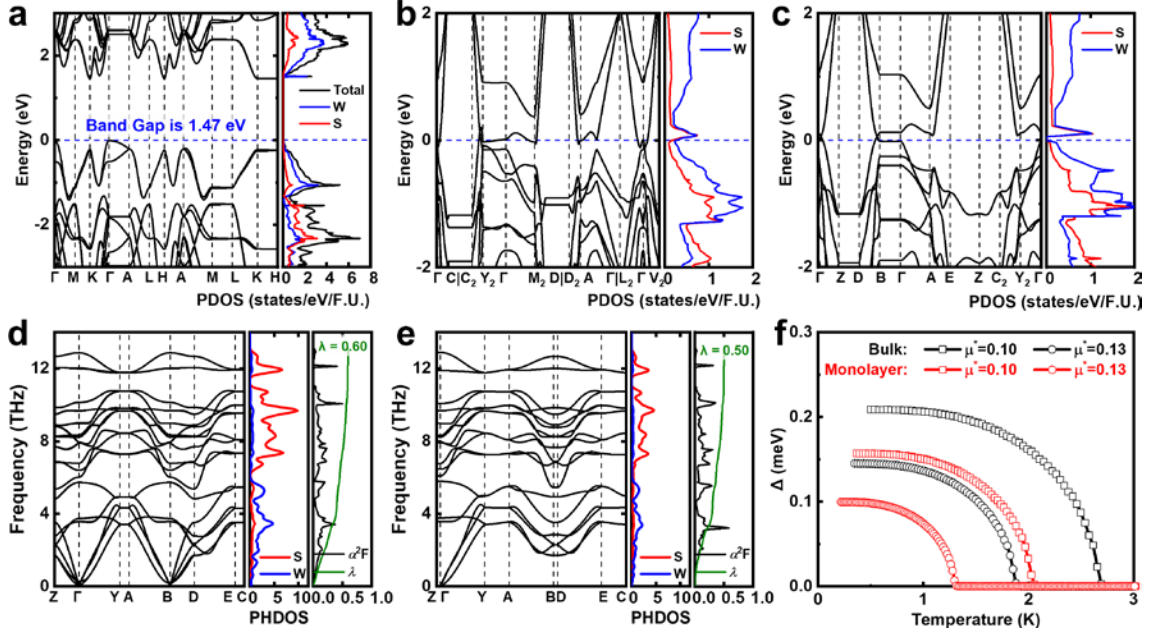


Supplementary Fig. 63 | Charge transport measurements of the device made of 1T'-WSe₂ with thickness of 71.2 nm (Supplementary Fig. 53) at low temperature. a, High-resolution temperature-dependent resistivity (ρ - T) of the 1T'-WSe₂ device below 12.0 K. **b**, Isotherms of current versus voltage characteristics at different temperatures. **c**, Isotherms of the Hall voltage as a function of applied magnetic fields at different temperatures. **d**, Plot of temperature-dependent Hall coefficient (R_H) and carrier concentration (n) at different temperatures. **e**, Plot of temperature-dependent carrier Hall mobility (μ_H). Inset: plot of the mobility as a function of $T^{-3/2}$. **f**, Temperature-dependent resistivity obtained from the continuous measurements of resistivity (line) and from I - V curves (empty square).

1.4. Discussion on the calculation results of 2H-WS₂ and 1T'-WS₂

Electronic band structures and projected density of states (PDOS) of bulk 2H-WS₂, bulk 1T'-WS₂ and single-layer 1T'-WS₂ were calculated by DFT. The results show that 2H-WS₂ is a semiconductor with a band gap of 1.47 eV (**Supplementary Fig. 64a**), while both bulk and single-layer 1T'-WS₂ are semi-metallic (**Supplementary Fig. 64b-c**) which show higher intrinsic carrier concentrations than that of 2H-WS₂ (the electronic density of states of bulk and single-layer 1T'-WS₂ at Fermi level (N_{Ef}) are higher than that of 2H-WS₂). Assuming that bulk and single-layer 1T'-WS₂ are conventional superconductors, we theoretically studied their superconducting properties in the framework of Bardeen-Cooper-Schrieffer (BCS) theory⁹. As a result, the absence of any imaginary frequencies in the phonon spectra indicates that structures of bulk and single-layer 1T'-WS₂ are dynamically stable (**Supplementary Fig. 64d-e**). The resulting EPC parameters, λ , of bulk and single-layer 1T'-WS₂ reach 0.60 and 0.50, respectively. T_c values were then obtained through the direct solution of the isotropic Eliashberg equation^{10,11}. We have thereby calculated their superconducting gaps (Δ), which were evaluated as a function of temperature (**Supplementary Fig. 64f**). The highest temperature, in which the superconducting gap value is nonzero, defines the critical transition temperature T_c . Therefore, both the bulk 1T'-WS₂ and single-layer 1T'-WS₂ are predicted to be superconductors with T_c values of up to 2.70 K and 2.06 K, respectively, with a typical value of $\mu^* = 0.1$. Although the calculated T_c values (2.70 and 2.06 K) are lower than our experimental results (8.6 K and 5.7 K for 90.1 nm and ~1.0 nm (single-layer) 1T'-WS₂, respectively), it shows the similar trend of the T_c values, indicating that 1T'-WS₂ is a

promising superconductor. Moreover, the shift of T_c to lower temperature in single-layer 1T'-WS₂ is also consistent with our experimental result.



Supplementary Fig. 64 | Electronic band structure comparison of bulk 2H-WS₂, bulk 1T'-WS₂ and single-layer 1T'-WS₂ by DFT calculations. a-c, Electronic band structure (left panel) and projected density of states (right panel) of (a) bulk 2H-WS₂, (b) bulk 1T'-WS₂ and (c) single-layer 1T'-WS₂. d,e, Phonon properties and Eliashberg spectral function for (d) bulk 1T'-WS₂ and (e) single-layer 1T'-WS₂. Phonon dispersion relations, projected phonon densities of states (PHDOS), and the Eliashberg spectral function ($\alpha^2F(\omega)/\omega$) as well as the integration ($\lambda(\omega)$) are plotted in the left, middle, and right panels, respectively. f, Calculated anisotropic superconducting gap (Δ) of bulk 1T'-WS₂ and single-layer 1T'-WS₂ on the Fermi surface as a function of temperature. The Coulomb pseudopotential parameters (μ^*) are set to be 0.10 and 0.13 for the bulk 1T'-WS₂ and single-layer 1T'-WS₂, respectively.

2. Supplementary tables

Supplementary Table 1 | Crystallographic and structure refinement data of 1T'-WS₂, 1T'-WSe₂, 1T'-MoS₂ and 1T'-MoSe₂ crystals.

Name	1T'-WS ₂	1T'-WSe ₂	1T'-MoS ₂	1T'-MoSe ₂
Formula	WS ₂	WSe ₂	MoS ₂	MoSe ₂
Formula weight (g·mol ⁻¹)	247.97	341.77	160.06	253.86
Temperature (K)	100	100	100	100
Crystal color	Black	Black	Black	Black
Crystal system	Monoclinic	Monoclinic	Monoclinic	Monoclinic
Space group	<i>C2/m</i>	<i>C2/m</i>	<i>C2/m</i>	<i>C2/m</i>
<i>a</i> (Å)	12.848(5)	13.739(4)	12.835(6)	13.742(4)
<i>b</i> (Å)	3.2178(12)	3.2651(8)	3.1838(14)	3.2704(9)
<i>c</i> (Å)	5.693(2)	5.865(1)	5.662(2)	5.895(1)
β (deg.)	112.847(13)	111.505(7)	113.695(11)	112.344(8)
<i>V</i> (Å ³)	216.88(15)	244.77(11)	211.86(16)	245.05(11)
<i>Z</i>	4	4	4	4
^a <i>D</i> _c (g·cm ⁻³)	7.594	9.275	5.018	6.881
^b GOOF on <i>F</i> ²	1.059	1.047	1.028	1.044
^c <i>R</i> ₁ , <i>wR</i> ₂ (<i>I</i> > 2σ(<i>I</i>))	0.0391, 0.0938	0.0555, 0.1333	0.0444, 0.0942	0.0900, 0.2236
<i>R</i> ₁ , <i>wR</i> ₂ (all data)	0.0434, 0.0955	0.0628, 0.1372	0.0535, 0.0984	0.1006, 0.2275
^d BASF	0.30(12)	0.40(14)	/	0.29(5)/0.12(6)
Largest diff. peak/hole (e Å ⁻³)	2.513 / -1.788	2.630 / -2.215	1.725 / -1.036	3.026 / -3.247

^a*D*_c refers to the crystal density. ^bGOOF refers to “the goodness of fit”. ^c*R*₁= $\sum||F_o|-|F_c||/\sum|F_o|$ for $F_o^2 > 2\sigma(F_o^2)$; $wR_2 = \sum[w(F_o^2 - F_c^2)]/\sum[w(F_o^2)^2]^{1/2}$, where $w = 1/[\sigma^2 F_o^2 + (AP)^2 + BP]$, and $P = (F_o^2 + 2F_c^2)/3$. ^dThe single crystal data of 1T'-WS₂ and 1T'-WSe₂ were refined as a 2-component twin, and the single crystal data of 1T'-MoSe₂ were refined as a 3-component twin.

Supplementary Table 2 | Atomic coordinates and equivalent isotropic displacement parameters of 1T'-WS₂, 1T'-WSe₂, 1T'-MoS₂ and 1T'-MoSe₂ crystals.

	Atom	Wyckoff	^a Occ	<i>x/a</i>	<i>y/b</i>	<i>z/c</i>	<i>U</i> _(eq)
1T'-WS₂	W1	<i>4i</i>	1	0.24424(8)	0.5	0.2963(2)	0.0256(4)
	S1	<i>4i</i>	1	0.1049(5)	0	0.2865(11)	0.0264(13)
	S2	<i>4i</i>	1	0.3599(5)	0	0.1797(11)	0.0269(13)
1T'-WSe₂	W1	<i>4i</i>	1	0.24320(13)	0.5	0.3032(3)	0.0344(6)
	Se1	<i>4i</i>	1	0.1047(3)	0	0.2944(7)	0.0349(9)
	Se2	<i>4i</i>	1	0.3581(3)	0	0.1701(7)	0.0344(9)
1T'-MoS₂	Mo1	<i>4i</i>	1	0.24391(13)	0.5	0.2933(3)	0.0281(5)
	S1	<i>4i</i>	1	0.1059(4)	0	0.2869(7)	0.0286(9)
	S2	<i>4i</i>	1	0.3621(4)	0	0.1832(7)	0.0291(10)
1T'-MoSe₂	Mo1	<i>4i</i>	1	0.2428(4)	0.5	0.3002(7)	0.0359(13)
	Se1	<i>4i</i>	1	0.1042(4)	0	0.2931(9)	0.0367(14)
	Se2	<i>4i</i>	1	0.3610(4)	0	0.1735(9)	0.0388(15)

^aOcc is defined as the atom site occupancy.

Supplementary Table 3 | Selected bond lengths (Å) of 1T'-WS₂, 1T'-WSe₂, 1T'-MoS₂ and 1T'-MoSe₂ crystals.

Bonds	1T'-WS₂	1T'-WSe₂	1T'-MoS₂	1T'-MoSe₂
W(Mo)1-S(Se)1	2.392(5)	2.493(4)	2.371(4)	2.499(6)
W(Mo)1-S(Se)1A	2.413(5)	2.514(4)	2.384(4)	2.517(6)
W(Mo)1-S(Se)1B	2.392(5)	2.493(4)	2.371(4)	2.499(6)
W(Mo)1-S(Se)2	2.450(6)	2.583(4)	2.446(5)	2.606(7)
W(Mo)1-S(Se)2C	2.514(6)	2.610(4)	2.486(4)	2.609(6)
W(Mo)1-S(Se)2B	2.450(6)	2.583(4)	2.446(5)	2.606(7)
W(Mo)1-W(Mo)1B	3.218(1)	3.2651(8)	3.184(1)	3.2704(9)
W(Mo)1-W(Mo)1D	3.218(1)	3.2651(8)	3.184(1)	3.2704(9)
W(Mo)1-W(Mo)1A	2.779(2)	2.777(2)	2.783(2)	2.812(5)
W(Mo)1-W(Mo)1E	2.779(2)	2.777(2)	2.783(2)	2.812(5)
W(Mo)1-W(Mo)1C	3.792(2)	3.979(3)	3.743(3)	3.972(6)

Symmetry code: A = $1/2-x, 1/2-y, 1-z$; B = $x, 1+y, z$; C = $1/2-x, 1/2-y, -z$; D = $x, -1+y, z$; E = $1/2-x, 3/2-y, 1-z$.

Supplementary Table 4 | Comparison of experimental and calculated Raman-active vibrational modes of 1T'-WS₂.

1T'-WS ₂			2H-WS ₂
Experimental Frequency (cm ⁻¹)	Calculated Data		Experimental Frequency (cm ⁻¹)
	Frequency (cm ⁻¹)	Intensity (normalized)	
110.7	114.5 (<i>B_g</i>)	< 0.001	
127.4	126.3 (<i>A_g</i>)	0.030	
178.7	174.7 (<i>B_u</i>)	0.039	
	174.9 (<i>A_g</i>)	0.005	
239.7	237.8 (<i>A_g</i>)	0.037	
267.6	267.7 (<i>A_g</i>)	0.143	
275.4	274.0 (<i>A_g</i>)	0.020	
	277.1 (<i>A_u</i>)	0.092	
295.4	307.7 (<i>B_u</i>)	0.010	
315.4	311.3 (<i>A_g</i>)	0.032	
	327.5 (<i>A_g</i>)	1	
	355.5 (<i>A_g</i>)	0.008	350.7 (<i>E_{2g}¹</i>)
406.2	406.7 (<i>A_g</i>)	0.043	420.5 (<i>A_{1g}</i>)
	433.6 (<i>A_g</i>)	0.001	

Supplementary Table 5 | Comparison of atomic distances (Å) from resolving EXAFS using EvAX and SCXRD for 1T'-WS₂ and 2H-WS₂.

Sample	Path	EvAX	SCXRD
1T'-WS₂	W-S _{average}	2.42	2.435(5)
	W-W1	2.81	2.779(2)
	W-W2	3.23	3.218(1)
	W-W3	3.78	3.792(2)
2H-WS₂	W-S	2.41	2.405(5)
	W-W	3.18	3.153(1)

Supplementary Table 6 | Comparison of experimental and calculated Raman-active vibrational modes of 1T'-WSe₂.

1T'-WSe ₂			2H-WSe ₂
Experimental Frequency (cm ⁻¹)	Calculated Data		Experimental Frequency (cm ⁻¹)
	Frequency (cm ⁻¹)	Intensity (normalized)	
	104.4 (<i>B_u</i>)	0.005	
105.9	105.3 (<i>A_g</i>)	0.005	
	108.1 (<i>B_g</i>)	0.002	
145.6	148.4 (<i>B_g</i>)	< 0.001	
152.7	154.0 (<i>B_u</i>)	0.005	
177.1	174.4 (<i>A_g</i>)	0.011	
	175.0 (<i>A_g</i>)	0.005	
	175.8 (<i>B_u</i>)	0.003	
182.7	188.0 (<i>B_g</i>)	0.002	
	220.2 (<i>A_g</i>)	0.002	
217.9	221.2 (<i>A_g</i>)	1	
236.6	235.6 (<i>B_u</i>)	0.078	248.3 (<i>E_{2g}¹</i>)
259.2	261.0 (<i>B_u</i>)	0.081	257.6 (<i>A_{1g}</i>)
	299.1 (<i>A_g</i>)	0.143	

Supplementary Table 7 | Comparison of superconducting T_c values in previously reported TMDs and our as-prepared 1T'-WS₂.

Compounds	Thickness	T_c (K)	Gate-tuning or High Pressure	Reference
2H-NbSe ₂	Bulk	7.0	No	12
	6 layers	3.8	No	13
	Nanotube	8.3	No	14
	Bilayer	2.5	No	15
	Monolayer	1.9	No	16
	Monolayer	1.0	No	17
	10 layers	4.56	No	17
	Nanoflake	4.83	No	18
	Bilayer	2.77	No	19
2H-NbS ₂	Bulk	6.2	No	20
	Bulk	5.7	No	21
	Bulk	8.9	20 GPa	22
2H-TaSe ₂	Bulk	0.2-0.5	No	23
	Bulk	0.13	No	24
1T-TaSe _{2-x} Te _{2x}	Bulk	2.5	No	25
2H-TaS ₂	Bulk	1.0	No	26
	4.2 nm	2.5	No	27
1T-TaS ₂	Bulk	1.5	2.5 GPa	28
2H-MoS ₂	20 nm	10.8	Gate-tuning in IL*	29
	6 layers	8-12	Gate-tuning in IL*	30
	Bilayer	7	Gate-tuning in IL*	30
	Monolayer	1.5	Gate-tuning in IL*	30
1T-MoS ₂	Bulk	4.6	No	31
1T'-MoS ₂	Restacked film	4	No	32
2H-WS ₂	20 nm	4.0	Gate-tuning in IL*	33
	Monolayer	3.15	Gate-tuning in IL*	34
K-doped WS ₂	Nanoflake	8.6	Gate-tuning in IL*	35
	Nanotube	5.3	Gate-tuning in IL*	36
1T'-MoTe ₂	Bulk	8.2	11.7 GPa	37
	Bulk	0.1	No	37
1T'-WTe ₂	Bulk	7	16.8 GPa	38
	Monolayer	~0.6-1	Gate-tuning	39
	Monolayer	~1	Gate-tuning	40
K-doped MoS ₂	Bulk 2H phase	6.9	No	41
	Bulk 1T phase	2.8	No	41
	Bulk 1T' phase	4.6	No	41

2M-WS ₂	Bulk	8.8	No	42
1T'-WS ₂	152.2 nm	8.7	No	This work
	90.1 nm	8.6		
	27.2 nm	7.5		
	6.9 nm	6.9		
	6.0 nm	6.6		
	3.7 nm	6.3		
	2.5 nm	6.1		
	~1.0 nm (single layer)	5.7		

*IL=Ionic liquid

Supplementary References

- 1 Gunawardane, R. P. & Arumainayagam, C. R. in *Handbook of Applied Solid State Spectroscopy* (ed D. R. Vij) 451-483 (Springer US, 2006).
- 2 Toh, R. J., Sofer, Z., Luxa, J., Sedmidubský, D. & Pumera, M. 3R phase of MoS₂ and WS₂ outperforms the corresponding 2H phase for hydrogen evolution. *Chem. Commun.* **53**, 3054-3057 (2017).
- 3 So, C. W. & Barham, D. The system K₂SO₄-K₂S. *J. Therm. Anal.* **20**, 275-280 (1981).
- 4 Sahoo, P. K., Memaran, S., Xin, Y., Balicas, L. & Gutiérrez, H. R. One-pot growth of two-dimensional lateral heterostructures via sequential edge-epitaxy. *Nature* **553**, 63-67 (2018).
- 5 Liu, L. *et al.* Phase-selective synthesis of 1T' MoS₂ monolayers and heterophase bilayers. *Nat. Mater.* **17**, 1108-1114 (2018).
- 6 Yu, X., Prévot, M. S., Guijarro, N. & Sivula, K. Self-assembled 2D WSe₂ thin films for photoelectrochemical hydrogen production. *Nat. Commun.* **6**, 7596 (2015).
- 7 Sokolikova, M. S., Sherrell, P. C., Palczynski, P., Bemmer, V. L. & Mattevi, C. Direct solution-phase synthesis of 1T' WSe₂ nanosheets. *Nat. Commun.* **10**, 712 (2019).
- 8 Yu, Y. *et al.* High phase-purity 1T'-MoS₂- and 1T'-MoSe₂-layered crystals. *Nat. Chem.* **10**, 638-643 (2018).
- 9 Bardeen, J., Cooper, L. N. & Schrieffer, J. R. Theory of Superconductivity. *Phys. Rev.* **108**, 1175-1204 (1957).
- 10 Allen, P. B. & Mitrović, B. in *Solid State Physics Vol. 37* (eds Henry Ehrenreich, Frederick Seitz, & David Turnbull) 1-92 (Academic Press, 1983).
- 11 Eliashberg, G. M. Interactions between electrons and lattice vibrations in a superconductor. *J. Exp. Theor. Phys.* **11**, 696-702 (1960).
- 12 Revolinsky, E., Spiering, G. A. & Beerntsen, D. J. Superconductivity in the niobium-selenium system. *J. Phys. Chem. Solids* **26**, 1029-1034 (1965).

- 13 Frindt, R. F. Superconductivity in Ultrathin NbSe₂ Layers. *Phys. Rev. Lett.* **28**, 299-301 (1972).
- 14 Nath, M., Kar, S., Raychaudhuri, A. K. & Rao, C. N. R. Superconducting NbSe₂ nanostructures. *Chem. Phys. Lett.* **368**, 690-695 (2003).
- 15 Staley, N. E. *et al.* Electric field effect on superconductivity in atomically thin flakes of NbSe₂. *Phys. Rev. B* **80**, 184505 (2009).
- 16 Ugeda, M. M. *et al.* Characterization of collective ground states in single-layer NbSe₂. *Nat. Phys.* **12**, 92 (2015).
- 17 Wang, H. *et al.* High-quality monolayer superconductor NbSe₂ grown by chemical vapour deposition. *Nat. Commun.* **8**, 394 (2017).
- 18 Zou, Y.-C. *et al.* Superconductivity and magnetotransport of single-crystalline NbSe₂ nanoplates grown by chemical vapour deposition. *Nanoscale* **9**, 16591-16595 (2017).
- 19 Lin, H. *et al.* Growth of environmentally stable transition metal selenide films. *Nat. Mater.*, doi: 10.1038/s41563-41019-40321-41568 (2019).
- 20 Fisher, W. G. & Sienko, M. J. Stoichiometry, structure, and physical properties of niobium disulfide. *Inorg. Chem.* **19**, 39-43 (1980).
- 21 Guillamón, I. *et al.* Superconducting Density of States and Vortex Cores of 2H-NbS₂. *Phys. Rev. Lett.* **101**, 166407 (2008).
- 22 Tissen, V. G. *et al.* Pressure dependence of superconducting critical temperature and upper critical field of 2H-NbS₂. *Phys. Rev. B* **87**, 134502 (2013).
- 23 Kumakura, T., Tan, H., Handa, T., Morishita, M. & Fukuyama, H. Charge density waves and superconductivity in 2H-TaSe₂. *Czech. J. Phys.* **46**, 2611-2612 (1996).
- 24 Yokota, K.-i., Kurata, G., Matsui, T. & Fukuyama, H. Superconductivity in the quasi-two-dimensional conductor 2H-TaSe₂. *Physica B* **284-288**, 551-552 (2000).
- 25 Liu, Y. *et al.* Nature of charge density waves and superconductivity in 1T-TaSe_{2-x}Te_x. *Phys. Rev. B* **94**, 045131 (2016).

- 26 Nagata, S. *et al.* Superconductivity in the layered compound 2H-TaS₂. *J. Phys. Chem. Solids* **53**, 1259-1263 (1992).
- 27 Navarro-Moratalla, E. *et al.* Enhanced superconductivity in atomically thin TaS₂. *Nat. Commun.* **7**, 11043 (2016).
- 28 Sipos, B. *et al.* From Mott state to superconductivity in 1T-TaS₂. *Nat. Mater.* **7**, 960 (2008).
- 29 Ye, J. T. *et al.* Superconducting Dome in a Gate-Tuned Band Insulator. *Science* **338**, 1193-1196 (2012).
- 30 Costanzo, D., Jo, S., Berger, H. & Morpurgo, A. F. Gate-induced superconductivity in atomically thin MoS₂ crystals. *Nat. Nanotechnol.* **11**, 339-344 (2016).
- 31 Fang, Y. *et al.* Structure Re-determination and Superconductivity Observation of Bulk 1T MoS₂. *Angew. Chem. Int. Ed.* **57**, 1232-1235 (2017).
- 32 Guo, C. *et al.* Observation of superconductivity in 1T'-MoS₂ nanosheets. *J. Mater. Chem. C* **5**, 10855-10860 (2017).
- 33 Jo, S., Costanzo, D., Berger, H. & Morpurgo, A. F. Electrostatically Induced Superconductivity at the Surface of WS₂. *Nano Lett.* **15**, 1197-1202 (2015).
- 34 Oleksandr, Z., Jianming, L., Jie, Y. & Jianting, Y. Monolayer Superconductivity in WS₂. *physica status solidi (RRL) – Rapid Research Letters* **11**, 1700245 (2017).
- 35 Shi, W. *et al.* Superconductivity Series in Transition Metal Dichalcogenides by Ionic Gating. *Sci. Rep.* **5**, 12534 (2015).
- 36 Qin, F. *et al.* Diameter-Dependent Superconductivity in Individual WS₂ Nanotubes. *Nano Lett.* **18**, 6789-6794 (2018).
- 37 Qi, Y. *et al.* Superconductivity in Weyl semimetal candidate MoTe₂. *Nat. Commun.* **7**, 11038 (2016).
- 38 Pan, X.-C. *et al.* Pressure-driven dome-shaped superconductivity and electronic structural evolution in tungsten ditelluride. *Nat. Commun.* **6**, 7805 (2015).
- 39 Fatemi, V. *et al.* Electrically tunable low-density superconductivity in a monolayer

- topological insulator. *Science* **362**, 926-929 (2018).
- 40 Sajadi, E. *et al.* Gate-induced superconductivity in a monolayer topological insulator. *Science* **362**, 922-925 (2018).
- 41 Zhang, R. *et al.* Superconductivity in Potassium-Doped Metallic Polymorphs of MoS₂. *Nano Lett.* **16**, 629-636 (2016).
- 42 Fang, Y. *et al.* Discovery of Superconductivity in 2M WS₂ with Possible Topological Surface States. *Adv. Mater.* **31**, 1901942 (2019).